



POLITECNICO DI TORINO  
MSc in Aerospace Engineering

Master's Degree Thesis

# Development of a High Precision Thrust Balance

Author: Ivan Mascolini

Tutor: Lorenzo Casalino

Final Project of the ERASMUS+/PROGRAMME COUNTRIES  
at the Institute of Space Systems of the University of Stuttgart

 **Institute of Space Systems**  
University of Stuttgart

Responsible in Stuttgart: Georg Herdrich  
Supervisor in Stuttgart: Johannes Martin

October 2019

(This page intentionally left blank)

*To my family,  
thank you for giving me  
the opportunities to grow up  
and pursue my passions.*

*To my friends,  
thank you for giving me  
the strength and hope to  
face these years together.*

## Abstract

A new AOCS called “High Precision Attitude and Orbit Control System Based on the Emission of Electromagnetic Radiation” (PACER) is currently under development at the Institute of Space Systems (IRS) of the University of Stuttgart.

This thesis deals a new high precision thrust balance in the sub micro-Newton range, with a new concept of active damping system, based on the emission of electromagnetic waves. The chosen radiation source are LEDs because of the low thermal radiation component, the low energy consumption and the continuous improvement of this technology in recent years.

Goal of this project will be the measurement of the light pressure emitted by LEDs, to evaluate a possible use of these technology for the PACER.

The motivation for the investigation of a such system based on upcoming and planned satellite missions within the commercial and scientific sector, where an ever-increasing demand on precision accuracy can be observed. For example, the “Lisa Pathfinder” mission demands on the AOCS require thrust as low as 1  $\mu\text{N}$  with a thrust noise of 0,1  $\mu\text{N}$  and a lifetime of 5 years.

A steady-state thrust stand based on a fiber-suspended torsion pendulum was developed, with thrust range 50 nN - 400 nN and a sensibility of 25 nN, that can be controlled and monitored by a PC using MATLAB, with a revolutionary damping system and an estimated cost less than 1000€. This stand could represent an excellent compromise for a first evaluation of the effects of electromagnetic radiation propulsors.

# Index

Index	5
Table of Figures	8
Table of Tables	11
Nomenclature	12
Abbreviations	14
Introduction	15
1 Basics	17
1.1 LED Technology	17
1.1.1 p-n junction	17
1.1.2 Output Power	19
1.2 Optics Basics	21
1.2.1 Geometrical optics	21
1.2.2 Lenses and Conical Mirrors	23
1.3 Photonic Propulsion	25
1.3.1 Existing and Future Photonic Thrusters	25
1.3.2 Physical Basics for Photonic Propulsion	26
1.4 Torsional Pendulum Dynamics	27
1.5 Existing Torsion Pendulum Thrust Balances	28
1.5.1 Overview	28
1.5.2 2001) nN Thrust Stand by Jamison, Ketsdever and Muntz [3]	29
1.5.3 2001) Sub- $\mu$ N Thrust Stand by Ziemer [4]	29
1.5.4 2002) nN Thrust Stand by Phipps and Luke [6]	30
1.5.5 2003) $\mu$ N Thrust Stand by Lake, Cavallaro and Spanjers [5]	31
1.5.6 2003) Sub- $\mu$ N Thrust Stand by Gamero-Castaño [8]	32
1.5.7 2006) nN Thrust Stand V2.0 by Phipps, Luke and Helgeson [7]	33
1.5.8 2012) $\mu$ N Thrust Stand by Y. Yang, Tu, S. Yang, Luo [9]	34
1.5.9 2013) Sub- $\mu$ N Thrust Stand by Soni and Roy [10]	34
1.5.10 Summary	36
2 Requirements and Boundary Conditions	37
2.1 Requirements	37
2.2 Boundary Conditions	38
3 Thrust Balance model	39
3.1 Specifics	39
3.2 Possible Damping Cases	43
3.2.1 First case	44
3.2.2 Second case	45
3.3 Conclusions	46

4	First Concept	48
4.1	Specifics	48
4.1.1	Measurement system	48
4.1.2	High Powered light source	50
4.1.3	Light Transport Through Mirror Reflection	53
4.1.4	Software and Hardware	53
4.1.4	Summary	53
4.2	LEDs of the Damping System	55
4.2.1	Common LEDs	55
4.2.2	Specialized LEDs	56
4.3	Cost Analysis	58
4.4	System Changes	58
5	Damping System Design	60
5.1	LED System	60
5.1.1	First solution	61
5.1.2	Second solution	61
5.1.3	Third solution	63
5.1.4	Radiant Power Model of LEDs	64
5.1.5	Efficiency Model of Conical Reflectors	66
5.1.5	Fourth solution	69
5.2	Mirrors System	72
5.3	Optical Aberrations	73
5.4	Cooling System	73
6	Swing Arm	77
6.1	Cooling System	77
6.2	Auxiliary damping system	78
6.3	Fiber Selection	79
6.4	Calibration Method	80
7	Measurement System	82
7.1	Laser Deflection System	82
7.1.1	Simulation n°1	82
7.1.2	Simulation n°2	83
7.2	Electrical-Digital Measurements	85
8	Power and Control systems	87
8.1	Damping system Power Consumption	87
8.2	Measurement system Power Consumption	88
8.3	Total Power Consumption	89
8.4	LEDs Damping System Power Control	89
8.5	Measurement System Digital Control	91

9	Final concept	93
9.1	List of Components	93
9.2	Design Description	95
9.2.1	Damping System Operation	95
9.2.2	Measurement System Operation	97
9.2.3	Swing Arm Operation	98
9.2.4	Nano Newton Thrust Stand by IRS	99
9.3	Cost Analysis	100
10	Conclusions	101
	References	102

## Table of Figures

Figure 1: a) Inner workings of a LED; b) Band-bending effect when a bias voltage is applied.	17
Figure 2: Correlation of semiconductor materials with light colour, wavelength and photon energy.	18
Figure 3: Colour temperature on Kelvin scale.	18
Figure 4: Emission spectra of cool and warm white LEDs, daylight used as reference.	19
Figure 5: Three methods to obtain white LEDs: a) blue LED die coated in yellow phosphor; b) 3-colour combination of distinct LED dies; c) UV LED die coated with distinct red, green, and blue phosphor coatings.	19
Figure 6: The radiant flux, measured as a function of forward current from a typical LED.	20
Figure 7: Rays and Wavefront generated by an emitting point source.	21
Figure 8: Geometry of specular reflection.	22
Figure 9: Geometry of refraction.	22
Figure 10: a) Positive-Converging lens; b) Negative-Diverging lens.	23
Figure 11: Longitudinal, transverse spherical aberration and the circle of least confusion for the lens.	24
Figure 12: The undercorrected longitudinal chromatic aberration of a simple lens.	24
Figure 13: a) Parabolic reflectors; b) Elliptical reflector.	25
Figure 14: Schematic operation principles of PACER with LED array, accumulation and collimation system, and thrust vectoring system.	26
Figure 15: Torsional pendulum a) Characteristics; b) Response amplitude for damping coefficient $\zeta < 1$ .	28
Figure 16: Schematic structure of the <i>Jamison et al.</i> thrust stand and its liquid seal damping system.	29
Figure 17: Schematic design of the <i>Ziemer</i> thrust stand configuration.	30
Figure 18: Schematic design of the First <i>Phipps et al.</i> thrust stand configuration.	31
Figure 19: Schematic design of the <i>Lake et al.</i> thrust stand configuration.	32
Figure 20: Schematic design of the <i>Gamero-Castaño</i> thrust stand configuration.	33
Figure 21: Schematic design of the Second <i>Phipps et al.</i> thrust stand configuration.	33
Figure 22: Schematic design of the <i>Yang et al.</i> thrust stand configuration.	34
Figure 23: Schematic design of the <i>Soni and Roy</i> thrust stand configuration.	35
Figure 24: Pendulum diagram.	40
Figure 25: Example of $Fm$ for $m = [1\ 2\ 3]$ and $F_{test} = 500nN$ .	41
Figure 26: $F_{test} = 500nN$ and $m = [1\ 2\ 3]$ a) angular displacement $\theta m$ ; b) angular velocity $\omega m$ ; c) angular acceleration $\alpha m$ ; d) damping force $Fm$ .	41
Figure 27: Example for $F_{test} = 500nN$ how work the damping system: blue $\theta m$ , red $\theta im$ a) $\theta 0$ and $\theta im1$ ; b) $\theta 1$ and $\theta im2$ ; c) $\theta 2$ and $\theta im3$ .	42
Figure 28: a) Damping force $Fm$ ; b) Potential energy of the system $Um$ during time; c) Potential energy of the system $Um$ for displacement.	43
Figure 29: a) First case: Single pulse, magnitude control; b) Second case: Multiple pulses, frequency control.	43
Figure 30: Maximum elastic response, rectangular and triangular load pulses [36].	45
Figure 31: First Case: $F_{min} = 50nN$ and: a) angular displacement $\theta m$ ; b) angular velocity $\omega m$ ; c) angular acceleration $\alpha m$ ; d) damping force $F(m)$ .	47
Figure 32: Second Case: $F_{min} = 50nN$ a) angular displacement $\theta m$ ; b) angular velocity $\omega m$ ; c) angular acceleration $\alpha m$ ; d) damping force $F(m)$ .	47
Figure 33: ELCOMAT autocollimator model choice depending on measuring accuracy and range [39].	49
Figure 34: Measuring principle of the autocollimator [39].	49
Figure 35: a) Electromagnetic spectrum b) Visible spectrum.	50
Figure 36: Mirrors schematic configuration of thrust stand.	53
Figure 37: Data path and light path of the system.	53
Figure 38: C-LED Royal Blue $\lambda: 440-450nm$ : a) Real image; b) Relation Electric and Radiated power [46].	55

Figure 39: First concept of high emitting light source: 3 configurations.	55
Figure 40: S-LED ASMT-JL31-NRS01, Colour: Royal Blue, Wavelength $\lambda$ (nm): 440-460.	56
Figure 41: S-LED ASMT-JL31-NRS01: a) Typical Characteristics [48]; b) Configuration concept.	56
Figure 42: UV-LED LZ1-00UAP5: Colour: Violet; Wavelength $\lambda$ (nm): 395.	57
Figure 43: UV-LED LZ1-00UAP5: a) Typical forward current characteristics; b) Typical normalized radiant flux over current [49].	57
Figure 44: Evaluation cost of the project	58
Figure 45: Typical 100W W-LED characteristics.	60
Figure 46: a) Reflector collimator; b) Lens; Lens characteristics [52].	61
Figure 47: a) LED, reflector, lens and starting of the tubing; b) Complete system with mirrors in blue.	61
Figure 48: a) Parabolic mirror; b) How it works; Characteristics.	62
Figure 49:a) ACL5040U Aspheric Condenser Lens; b) How it works; Characteristics.	62
Figure 50: Chosen Fresnel lens characteristics.	62
Figure 51: a) Component design to support the aspheric lens; b) Complete system.	63
Figure 52: Optgeo simulation of the second solution, the element in green is the strike point.	63
Figure 53: Chosen Elliptic reflector characteristics.	63
Figure 54: Optgeo simulation of the third solution, the element in green is the hitting point.	64
Figure 55: Luminous Efficiency Function, $V(\lambda)$ .	64
Figure 56: W-LED YJ-BC-160H-G01 characteristics [57].	65
Figure 57: a) Spectral power distribution YJ-BC-160H-G01; b) Luminous efficiency function; c) product between graph a) and b).	65
Figure 58: First reflector: a) 3D; b) 2D; Characteristics.	66
Figure 59: Second reflector: a) 3D; b) 2D; Characteristics.	66
Figure 60: Third reflector: a) 3D; b) 2D; Characteristics	67
Figure 61: The reflection of the radiation flux generates a force perpendicular to the mirror.	67
Figure 62: LED Intensity distribution: a) 3D; b) 2D	68
Figure 63: Intensity distribution after reflector: a) 1 <sup>th</sup> ; b) 2 <sup>th</sup> ; c) 3 <sup>th</sup> : 1) 3D; 2) 2D; 3) with inclination effect.	69
Figure 64: a) Typical car headlights LEDs; b) Light distribution inside reflector.	69
Figure 65: First concept 3 LEDs of 10 mm diameter: a) Frontal view; b) 3D View; c) LEDs inside reflector.	70
Figure 66: Second concept 5 LEDs of 10 mm diameter: a) Frontal view; b) 3D View; LED Characteristics.	70
Figure 67: a) Inclination effect depending on view angle; b) Configuration.	71
Figure 68: Optgeo simulation of the Fourth solution, the element in green is the hitting point at 350 mm from the end of the reflector, or rather 450 mm from the focus.	71
Figure 69: a) Hitting area depending on view angle; b) Distribution of radiated power emitted.	72
Figure 70: Complete system with mirrors; Table with quantity and sizes of mirrors.	72
Figure 71: a) Chosen servomotor; b) Maximum limit angles; Characteristics.	73
Figure 72: Water cooling system scheme and Components.	74
Figure 73: a) Water pump; b) Heat exchanger radiator; c) Fan; d) Tank.	74
Figure 74: a) Typical Water block [63]; b) Designed Water block; c) Radiator fins; d) Front view; e) Lateral view; Characteristics.	75
Figure 75: Configurations: a) 1; b) 2; c) 3.	75
Figure 76: Cross section of the arm; Characteristics.	77
Figure 77: Eddy-current damp system; Legend.	78
Figure 78: Force diagram acting on pendulum; Legend.	80
Figure 79: Complete arm configuration.	80
Figure 80: Basic laser deflection Simulation n°1; Components;	82
Figure 81: Simulation n°1: Scheme after mirror deflection and results; Results.	83
Figure 82: Schematic configuration of Simulation n°2; Components.	83
Figure 83: a) Plano-Convex lens; b) Plano-Concave lens; Characteristics.	84
Figure 84: Simulation n°2: Scheme after mirror deflection a) Conf. 1; b) Conf. 2; Results.	84

Figure 85: Simulation n°2 laser beam diameter: a) Conf. 1; b) Conf. 2; Legend.	85
Figure 86: Photoresistor LDR GL5528 shape; Characteristics [71];	85
Figure 87: Simulation of electronic measurement using photocells.	86
Figure 88: Circuit diagram of LEDs system.	87
Figure 89: Circuit diagram of LEDs Cooling system.	87
Figure 90: Circuit diagram of Servo rotating the pivot mirror.	88
Figure 91: Circuit diagram of Laser, main voltage coming from Servo circuit.	88
Figure 92: Circuit diagram of a Multiplexer with 8 Photocells.	88
Figure 93: Circuit diagram of Arduino board supplying 5 Multiplexers.	89
Figure 94: Circuit diagram of the thrust stand systems requiring electrical power supply.	89
Figure 95: Gears system: Servomotor controls potentiometers rotations: a) Trim POT; b) Rotary POT.	90
Figure 96: Damping system: Mirror-servo and Gear-servo control made by Arduino Nano:	91
Figure 97: Multiplexer connections with photocells and resistances, and main pins.	91
Figure 98: Arduino Mega pins connections with the 5 multiplexers.	92
Figure 99: Reflector with LEDs, Water block and fittings: a) Front view; b) Side view.	95
Figure 100: Damping system: a) Side view; b) Top view.	96
Figure 101: Light beams on the final mirror on the swing arm: a) Front view; b) 3D view.	96
Figure 102: Water cooling system for the LEDs of the damping system.	97
Figure 103: Measurement system based on laser deflection.	97
Figure 104: Final laser beam size, tested for $F_{min}= 50nN$ and $F_{Max}= 500nN$ .	98
Figure 105: Screen to manually measure the angular displacement or electronically using the LDR system.	98
Figure 106: Thrust stand arm.	99
Figure 107: Schematic design of the IRS thrust stand configuration.	99
Figure 108: Details of the: a) Main LEDs electromagnetic damping system; b) Auxiliary Eddy-Current damping system.	100
Figure 109: Cost analysis of the thrust stand.	100

## Table of Tables

Table 1: Overview of the thesis' chapters and summary of their respective content	16
Table 2: Characteristics of common lens types.	23
Table 3: Overview of existing concepts for thrust stands in the sub micro-Newton range based on torsion pendulum sorted by year.	36
Table 4: Thrust stand requirements.	38
Table 5: Thrust stand boundary conditions.	38
Table 6: Pendulum data.	39
Table 7: Angular displacements produced by maximum and minimum thrust	44
Table 8: Results of the two cases simulated.	46
Table 9: General elements of the thrust stand.	54
Table 10: Resume of changes after meeting.	59
Table 11: Data of the MATLAB simulation for different types of reflectors.	68
Table 12: Data of the Fourth solution MATLAB simulation.	71
Table 13: Data of the thrust stand fiber.	79
Table 14: Sensibility Simulation n°2;	85
Table 15: All MUXes pins connections with Arduino Mega board.	92
Table 16: List of the thrust stand components.	94

## Nomenclature

Symbol	Unit	Description
$A_0$	–	Radiant flux constant
$A_1$	–	Radiant flux linear constant
$A_2$	–	Radiant flux square constant
$c$	$kg\ m^2/s$	Pendulum damping constant
$c_0$	$m/s$	Speed of light
$c_p$	$J/(mol\ K)$	Heat capacity at constant pressure
$d$	$\mu m$	Pendulum fiber diameter
$D$	$mm$	Laser beam diameter
$E_{photon}$	$eV$	Energy carried by a photon
$E_{Ref}$	–	Reflector efficiency
$E_{Ref\_fin}$	–	Reflector efficiency depending on inclination and perfect reflection
$E_{Ref\_incl}$	–	Reflector efficiency depending on inclination
$f$	$m$	Lens or mirror focus
$F$	$N$	Force applied to the pendulum arm
$F_i$	$N$	Ideal Force generated by a radiant flux
$F_m$	$nN$	Force generated by the damping system
$F_{test}$	$nN$	Force generated by the thruster tested
$F_\phi$	$N$	Force generated by a flux of photons
$G$	$MPa$	Torsional modulus of the pendulum fiber
$h$	$kg\ m^2/s$	Planck constant
$I$	$kg\ m^2$	Pendulum moment of inertia
$i$	$^\circ$	Inclination of the radiation respect to the normal of the mirror
$I_e$	$W/sr$	Intensity of a light source radiant flux
$I_F$	$A$	LED current
$I_v$	$J$	Intensity of a light source luminous flux
$J$	$kg\ m^2$	Polar moment of inertia of the pendulum fiber
$k_0$	$Nm/^\circ$	Spring constant of the pendulum fiber
$LER$	$lm/W$	Luminous Efficacy of Radiation
$m$	$kg$	Pendulum arm mass
$M$	$g/mol$	Pendulum material molar mass
$m_{limit}$	$kg$	Maximum safe carrying capacity of the pendulum fiber
$M_t$	$N\ m$	Torsional moment applied to the pendulum
$n$	–	Photons number of a flux
$n_1$	–	Lower index of refraction
$n_2$	–	Higher index of refraction
$P_{in}$	$W$	LED electric power
$p_{photon}$	$J\ s/m$	Impulse carried by a photon
$Q$	$J$	Heat transferred from the LEDs to the Pendulum arm

$R$	$m$	Pendulum lever length
$R_1$	$mm$	Curvature radius of the lens surface closer to the light source
$R_2$	$mm$	Curvature radius of the lens surface farther to the light source
$S(\lambda)$	$W/nm$	Spectral power distribution of a light source
$t$	$s$	Time
$T$	$s$	Pendulum period
$t_d$	$s$	Single pulse acting time of the damping system
$T_J$	$K$	LED junction temperature
$U_m$	$J$	Pendulum potential energy
$\nu$	$Hz$	Frequency
$V(\lambda)$	–	Luminous Efficiency Function
$V_F$	$V$	LED voltage
$V_{in}$	$V$	Voltage of the main power
$x_n$	$mm$	Amplitude of the $n^{\text{th}}$ peak of oscillation
$\beta$	$^\circ$	Laser initial inclination
$\Delta T$	$K$	Temperature difference between LEDs and pendulum arm
$\Delta x_1$	$mm$	Initial laser length displacement, before lenses
$\Delta x_2$	$mm$	Final laser length displacement, after lenses
$\zeta$	–	Pendulum damping coefficient
$\theta$	$^\circ$	Pendulum angular displacement
$\Theta$	$rad$	Laser beam divergency
$\dot{\theta}$	$^\circ/s$	Pendulum angular velocity
$\ddot{\theta}$	$^\circ/s^2$	Pendulum angular acceleration
$\theta_i$	$^\circ$	Incident ray angle
$\theta_R$	$^\circ$	Refracted ray angle
$\theta_r$	$^\circ$	Reflected ray angle
$\theta_{sens}$	$^\circ$	Pendulum angular sensibility
$\lambda$	$nm$	Wavelength
$\Lambda$	–	Logarithmic decrement of the calibration method
$\phi_0$	$W$	Radiant flux of a light source at 0 K
$\phi_e$	$W$	Radiant flux of a light source
$\phi_{e\_fin}$	$W$	Radiant flux with effects: Reflector, Inclination, Reflection
$\Phi_{photons}$	$1/s$	Flux of photons
$\phi_\nu$	$lm$	Luminous flux of a light source
$\omega_d$	$rad/s$	Pendulum damped frequency
$\omega_n$	$rad/s$	Pendulum natural frequency

## Abbreviations

Abbreviation	Description
AOCS	Attitude and Orbit Control Systems
C-LEDs	Common LEDs
COB	Chip On Board
C-POT	Current control Potentiometer
DSMC	Direct Simulation Monte Carlo
ESA	European Space Agency
FEPP	Field Effect Electric Propulsion Subsystem
FMEJ	Free Molecular Electro Jets
FWHM	Full Width at Half Maximum
GaAs	Gallium Arsenide
GaAsP	Gallium Arsenide Phosphide
GaN	Gallium Nitride
GaP	Gallium Phosphide
GFPPT	Gas-Fed Pulsed Plasma Thrusters
In-FEEP	Indium Field Emission Electric Propulsion
IR	Infrared Radiation
IRS	Institut für Raumfahrtssysteme
LDR	Light Dependent Resistor
LDS	Laser Distance Sensors
LED	Light Emitting Diode
LER	Luminous Efficacy of Radiation
LPT	Laser Plasma Thruster
LVDT	Linear Variable Differential Transformer
MEMS	Microelectromechanical Systems
MUX	Multiplexer
PACER	Precision Attitude Control system based on Electromagnetic Radiation emission
PID	Proportional Integral Differential
PPT	Pulsed Plasma Thrusters
PWM	Pulse With Modulation
S-LEDs	Specialized LEDs
SPD	Spectral Power Distribution
UV	Ultraviolet Radiation
VAT	Vacuum Arc Thrusters
VLM	Vaporizing Liquid Microthruster
V-POT	Voltage control Potentiometer
W-LEDs	White LEDs
ZnSe	Zinc Selenide

# Introduction

## Relevance of the Topic

The high-Precision Attitude Control system based on the emission of Electromagnetic Radiation (PACER) is a new type of propellant-less photonic propulsion system currently under development at the Institute of Space Systems (IRS – German abbreviation for “Institut für Raumfahrtsysteme”) [1]. With a projected thrust generation of  $1\mu\text{N}$  and an active thrust vectoring system, it is meant to become an alternative to current micro-thruster technology. Micro-thrusters are spaceflight propulsion systems operating in a thrust range of micro-Newtons. They are used for precise attitude and orbit control systems (AOCS) of satellite and probe missions for their highly precise thrust capabilities.

Current AOCSs can generally be divided into: Chemical systems, Electrical systems and Propellant-less systems like reaction wheels and photonic propulsion systems. Chemical and electrical propulsion devices all depend on propellant mass, thus making propellant storage and distribution systems necessary. Photonic propulsion systems like PACER only need electrical power in the range of around  $1\text{kW}$ , which can easily be provided by a spacecraft’s solar power supply. Because of this independency, photonic systems could significantly reduce a spacecraft’s overall system complexity and operate for a theoretically infinite time. The system is based on the physical principle that  $1\text{W}$  of emitted electromagnetic radiation corresponds to  $3.3\text{nN}$  of thrust independent from the radiation’s wavelength. The emitted thrust is scalable over a wide range of thrust levels also in sub-micro Newton.

PACER is designed to fulfil requirements mission as the ones of the Lisa-Pathfinder launched in 2015. Lisa-Pathfinder is a test satellite of the European Space Agency (ESA) to test the performance of measurement devices for the later mission “Evolved Laser Interferometry Space Antenna/ New Gravitational Wave Observatory” (eLISA/NGO). This mission consists of three spacecraft in a triangle constellation with 2.5 million kilometres between each of the craft. Because of the distance between the craft a highly precise attitude control system with  $1\mu\text{N}$  of thrust and  $0.1\mu\text{N}$  thrust noise was needed [2].

To accurately determine the performance of photonic emission thrusters, producing nano-Newtons of thrust, a new, highly accurate thrust stand must be developed. Here, it is reported the design and characterization of a thrust stand based on the principle of a torsion balance. The device is essentially a torsion fiber pendulum, which undergoes angular deflections when a force acts on the arm. This force can be measured as linear displacement of the balance arm at a known distance from the pivot. *Jamison et al.* [3], *Ziemer* [4], *Lake et al.* [5], *Phipps et al.* [6] [7], *Gamero-Castaño* [8], *Yang et al.* [9], *Soni and Roy* [10] have all built thrust stands with the same working principle, albeit with different methods of calibration, damping techniques, and displacement measurement.

In comparison, *Jamison et al.* thrust stand was calibrated using DSMC techniques, and the lowest thrust measured was  $88.8\text{ nN}$ . The steady state thrust measured by *Ziemer* was  $1\mu\text{N}$  using a FEEP thruster. *Lake et al.* measured the lowest thrust  $5\mu\text{N}$  of uPPT using LVDT, while *Phipps et al.* using a fiber suspended pendulum with a  $254\mu\text{m}$  steel fiber diameter has reached  $100\text{ nN}$ . The lowest measured by *Gamero-Castaño* was  $0.11\mu\text{N}$  using an electrospray source and  $7.89\mu\text{N}$  using a colloid thruster. *Yang et al.* used a pendulum stage suspended from  $502\mu\text{m}$  titanium fiber calibrated by measuring the moment of inertia of the setup and oscillation frequency with a resolution of  $90\text{ nN}$ . The most recent projected by *Soni and Roy* can measure a lowest thrust of  $1.3\mu\text{N}$  with an uncertainty of  $\pm 20\%$ . In Chapter 1.5 the existing thrust stands previously mentioned are described individually and summarized for resolution and lower thrust measured.

In order to validate the idea of the future PACER it was decided to design an innovative damping system based on the same technology. The displacement measurement is obtained by laser deflection and an auxiliary eddy-current damping system was chosen to validate the results of the first one.

## Objectives and Structure of the Study

This study present and examine existing thrust stand design concepts and determine the requirements for a new future thrust stand at the IRS. Based on this requirement profile and the recognized boundary conditions the project design is presented, from the first concept and primary cost analysis to the final ones, evaluating the use of different technologies and describing guidelines for future assembly. The following table provides an overview of the thesis chapters.

Number	Chapter Name	Content Summary
1	Basics	Lists of the most important equations and properties of LEDs, Optics, Photonic thrusters, Torsional pendulums. Eight existing nN- $\mu$ N thrust stands based on torsional pendulum are presented separately and at the end there is a summary table with the most important information.
2	Requirements and Boundary Conditions	A list of requirements and boundary conditions is explained based on the existing thrust stands. The requirement profile lists several points which map out the targeted properties of the thrust stand while the boundary conditions describe the present dimensional capabilities.
3	Thrust Balance Model	The building of the pendulum simulator and some tests on how it works are presented. Two possible configurations of the damping system were evaluated and explained. At the end are presented the conclusions and the choice between the two configurations.
4	First Concept	First analysis of the components required to design the thrust balance. Analysis on the specifics of the system, research on the existing LEDs and its performance, primary evaluation of the thrust balance cost and the system changes after a project meeting.
5	Damping system design	All the consideration made on the design of the damping system from first ideas to the final concept. Design of the LED system, analysis on the real radiant power emitted, efficacy of the collimating system, sizing of the mirror system, design of the water-cooling system.
6	Swing arm	Design of the pendulum's arm, dimension, material, cross section. Sizing of two configuration thrusters cooling system, choice of the vibration auxiliary damping system, pendulum fiber and calibration method. Sizing of the counter-balanced weight on the arm.
7	Measurement System	Development of the measurement system based on laser deflection over optical lens and mirrors. After two configurations are presented, the first with laser visible measurement on a chart, the second based on an electrical measurement system upgrading the first one.
8	Power and Control System	Design of power and control system, definition of all the electrical components. Electricity consumption of damping system, measurement system and the total thrust stand. Design and explanation of the control with Arduino with assembly guide.
9	Final Concept	Presentation of the final concept after the work made in the previous chapter. List of the all components of the thrust stand with the respective quantities and costs, an explication of how work the system, in the end a cost analysis and a comparison with the first concept.
10	Conclusions	The results and conclusions are summarized, and an overview of the future thrust stand design concept is given.

Table 1: Overview of the thesis' chapters and summary of their respective content

# 1 Basics

This chapter introduces the technologies that have been used for the development of the thrust stand presented in this thesis. First, there is an analysis on LED technology that has been evaluated for the design of an active damping system based on electromagnetic emission and for a possible future use of this technology as photonic thrusters. For this reason, there are also an overview of the optics basics and an introduction to optical elements such as lenses and conical mirrors, followed by research on existing photonic thrusters and the presentation of future concepts. The last two sub-chapters focused on the dynamics of torsional pendulum and existing thrust stand based on that technology.

The results have been used in Chapter 2 for an evaluation of requirements and boundary conditions of the project, and in Chapter 3 for an analysis on possible concepts.

## 1.1 LED Technology

This section discusses the full array of LED fundamentals, light emission mechanism including band energy, material and wavelength correlation. It is also described how the white LEDs work, how to determinate the radiant light power and which are the common effects that decrease this value during the diode lifetime.

### 1.1.1 p-n junction

As the name implies, a light-emitting diode (LED) is a semiconductor diode that emits photons when a current flows through the device. Application of a voltage across the *p* and *n* terminals of the device can impart enough energy to excite electrons into higher energy states. Then the excited electrons spontaneously drop from the conduction band to recombine with holes in the valence band, releasing a photon in the process [11], Figure 1.

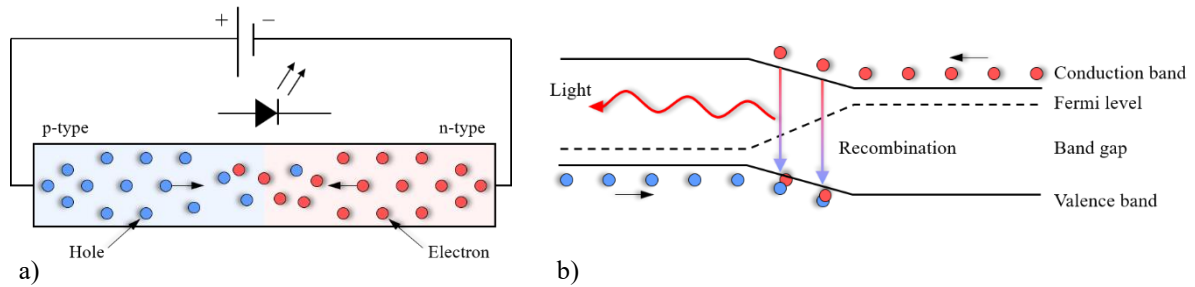


Figure 1: a) Inner workings of a LED; b) Band-bending effect when a bias voltage is applied.

Selection of semiconductor materials with appropriate bandgap energies allows the control of the wavelength of photon emitted. Wider bandgaps will result in the production of higher energy light. The energy  $E$  carried by a photon of a certain wavelength is given in Eq. 1.

$$E_{photon} = \frac{h c_0}{\lambda} = h\nu \quad (Eq. 1)$$

with  $h$  being Planck's quantum of action,  $\nu$  the photon's frequency and  $c_0$  the speed of light in a vacuum. The relationship of photon  $\lambda$  and its  $\nu$  is:

$$\lambda = \frac{c_0}{\nu} \quad (Eq. 2)$$

Traditionally, LEDs can be made from a wide range of semiconductor materials, each possessing a characteristic bandgap energy ( $E_B$ ), which corresponds to different wavelengths of light emission. Peak emission wavelengths of LEDs can range from ultraviolet (360 nm) to infrared (950 nm).

The full spectrum of visible light can be produced using several material bases, including gallium arsenide (GaAs) for infrared emission [12], gallium arsenide phosphide (GaAsP) for red to yellow emission [13], gallium phosphide (GaP) for yellow to green emission [14], zinc selenide (ZnSe) in early blue emission [15], and gallium nitride (GaN) for green to ultra-violet emission [16]. The corresponding wavelength-colour association is depicted in Figure 2.

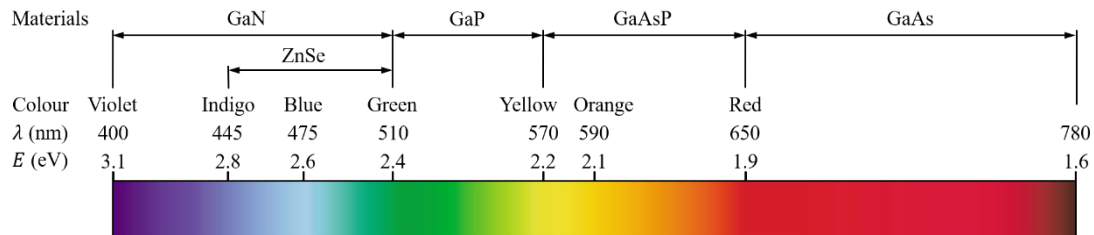


Figure 2: Correlation of semiconductor materials with light colour, wavelength and photon energy.

When considering the suitability of a light source for a particular application, factors such as luminous efficiency, effective brightness (measured in lumens,  $lm$ ), and colour temperature (measured in Kelvins,  $K$ ) are of importance. The colour temperature is referred to the temperature of an ideal black body, if that is heated its energy will increase entering the field of visible light, visible areas from low to high colour temperature is determined by the colour temperature orange  $\rightarrow$  yellow  $\rightarrow$  red  $\rightarrow$  yellow  $\rightarrow$  white  $\rightarrow$  blue [17]. Generally, a greater fraction of longer wavelength light is attributed with warmer light temperatures, as shown in Figure 3.

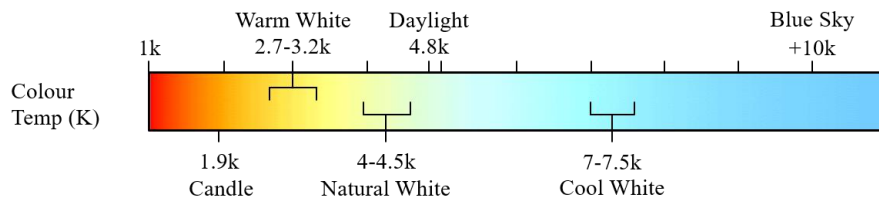


Figure 3: Colour temperature on Kelvin scale.

Figure 4 compares the emission spectra of cool and warm white LEDs with the daylight spectrum [18]. Current LED technology allows for light emission over the entire visible spectrum, as well as extending into the UV and IR regions. There are a few ways to achieve white lighting in solid-state LED technology. The most common and inexpensive of these are made possible with the development of colour altering phosphors which are used to coat the LED die post fabrication. A blue or ultraviolet LED emitting with a peak in the 450-500nm wavelength range is coated with a yellow phosphor. A portion of the light is converted into yellow light, resulting in a non-uniform full spectral range appearing as white light, as shown in Figure 5a. Variations in the properties and quality of both the LED die and the phosphor will result in varying qualities of light. A second way to produce white light is to combine the emissions of three or more LED dies covering the wavelength spectrum as in Figure 5b. This method is the most expensive approach due to the requirement for multiple LED dies and potentially multiple phosphor coatings. Finally, a third approach to producing white light is to coat an ultra-violet LED with multiple phosphor materials Figure 5c. This allows the production of a wide sampling of spectral peaks with relatively few LED die sources, producing a robust white appearance. Currently, the lighting industry regulates key parameters of LED products based on colour uniformity, emission brightness, power management, and colour temperature [19].

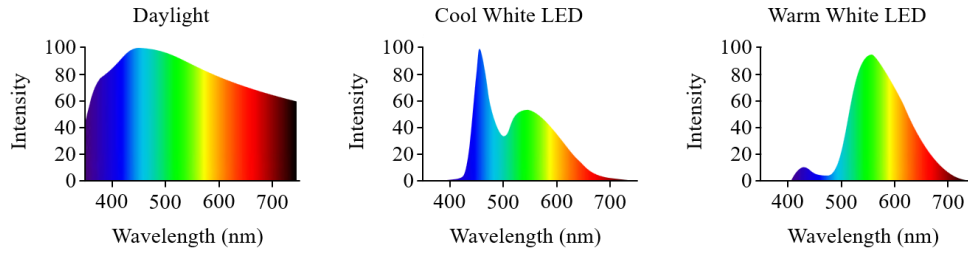


Figure 4: Emission spectra of cool and warm white LEDs, daylight used as reference.

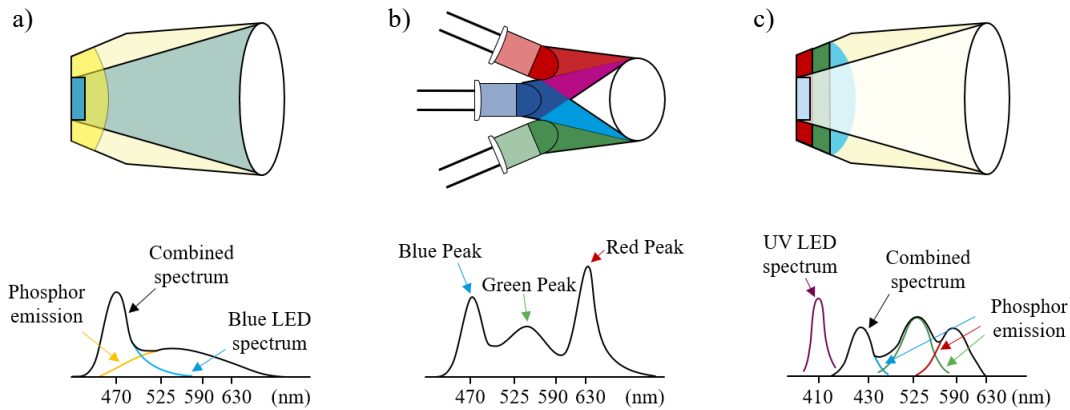


Figure 5: Three methods to obtain white LEDs: a) blue LED die coated in yellow phosphor; b) 3-colour combination of distinct LED dies; c) UV LED die coated with distinct red, green, and blue phosphor coatings.

### 1.1.2 Output Power

One of the problems with controlling the light output from LEDs is that the technology itself has some inherent nonlinearities. These nonlinearities stem from the way semiconductor materials behave when used in this way. Both the amount of current and the temperature of the device will change the properties of the resulting illumination. When an LED is operated with a forward voltage, heat is generated by non-radiative combination and photon absorption in the material. This injected heat increases the temperature of the junction until the heat production is balanced with the heat transfer from the device. When an equilibrium is reached the device will have reached its operation temperature. Raised junction temperatures have a negative effect on device lifetime.

The total radiant flux  $\phi$  from a LED is influenced by current  $I$  and junction temperature  $T_j$  and several material and device characteristics, such as the crystal defect density, dopant concentration, current leaks etc. Since the materials used might be unknown, it must be used empirical models to describe the light output corresponding to a given set of  $I$  and  $T_j$ . The emitted light power as a function of temperature  $\phi_e(T)$  has been empirically determined to be an exponentially decaying function:

$$\phi_e(T) \propto \phi_0 e^{-(T-300 K)/T_0} \quad (\text{Eq. 3})$$

where  $T_0$  is a material specific constant and  $\phi_0$  can be interpreted as the power emitted at 300 K [20]. Assuming 100 % quantum efficiency, the light output would be directly proportional to the current, since every electron-hole pair would be converted to a photon. However, it is seen that efficiency decreases with increasing current, the so-called droop effect. Different effects have been suggested as the cause for this efficiency decrease. Examples of such effects are Auger recombinations, surface recombinations, and defect recombinations [21].

Incorporating all these effects in a purely empirical relation between output power and current, using a polynomial description:

$$\phi_e(I) = A_0 + A_1 I_F + A_2 I_F^2 \quad (\text{Eq. 4})$$

where  $A_0, A_1, A_3$  are fitting constants. The intersection  $A_0$  should of cause be zero as no current will give zero light output. The proportional term  $A_1$  can be interpreted as the linear relation between forward current and light output, that can be observed at low currents. The square term  $A_2$  can then be used to describe the droop, as shown in Figure 6.

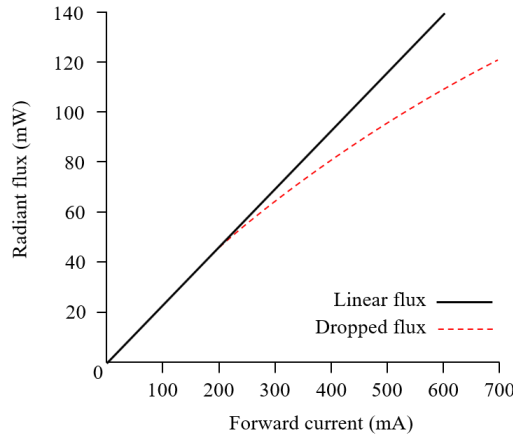


Figure 6: The radiant flux, measured as a function of forward current from a typical LED.

The spatial distribution of light is generally required to have a high homogeneity of intensity and colour in the illuminated field. In relation to time dependent phenomenon in lighting, there is the issue of unwanted low frequency visual flicker, glare, changes over longer times in LEDs caused by heating of the junction and changes in light output caused by material degradation occurring over the lifetime of the device. For clustered light sources, there is the further issue of coloured shadows, occurring when the differently coloured light sources, set up together, cast differently coloured shadows at different angles. Attention to these issues is important when designing a lighting solution [22].

The definition of the is luminous intensity was adopted by *General Conference on Weights and Measures* in 1979, it is applicable to any spectral power distribution by employing a generalization of the spectral sensitivity of the human eye. For a source with radiant intensity  $I_e$  the luminous intensity  $I_v$  at a given wavelength  $\lambda$  is:

$$I_v(\lambda) = \left[ 683.002 \frac{lm}{W} \right] V(\lambda) I_e(\lambda) \quad (\text{Eq. 5})$$

where  $V(\lambda)$  is the luminosity function defining the eyes sensitivity. For a light source, the net amount of perceivable light is defined by the luminous flux, given by the integration or summation over all the spherical coordinates and  $\lambda$ :

$$\phi_v = \int_0^{2\pi} \int_0^{\pi} \int_{380\text{ nm}}^{730\text{ nm}} I_v(\lambda, \theta, \varphi) \sin(\theta) d\lambda d\theta d\varphi \quad (\text{Eq. 6})$$

where  $\theta$  and  $\varphi$  are the spherical coordinates of a sphere around the light source. The integral over  $\lambda$  from  $380\text{ nm}$  to  $730\text{ nm}$  denotes integration across the visible spectrum. When dealing with visual responses the integrals will yield zero outside the visual range and are therefore in the following given as indefinite integrals.

An important characteristic of an LED is its luminous efficacy, the ratio between luminous flux and electrical input power  $\phi_v/P_{in}$ . The term is sometimes confused with luminous efficiency that describes the ratio between luminous flux and radiant flux, which gives an indication of the visual usefulness of the spectral power distribution (SPD)  $S(\lambda)$ .

$$\frac{\phi_v}{\phi_e} = \frac{\int V(\lambda)S(\lambda)d\lambda}{\int S(\lambda) d\lambda} \quad (Eq. 7)$$

Due to the variations in spectral power distribution caused by changes in the junction temperature it is important to keep the junction temperature of the LED constant during measurements. The most common way of characterizing LED devices is with an ambient temperature of 25°C, using a very short current pulse. Due to the small width of the active region and the high current density, it must however be expected that a rapid temperature change will occur even over short time spans. This characterization method can be used to compare performance between different LED devices, but it will not be applicable in situations where an LED is operated continuously at a higher junction temperature. A typical change in dominating wavelength is on the order of 0.05 nm/°C [23], so with an operation temperature of 120°C, the shift becomes 5 nm. Within the same temperature span the LED might loose between 5% and 30% of the luminous flux [24]. To be able to maintain and control a stable temperature for measurement of the LED, it should be mounted on a surface, which is thermally connected to a cooling system.

LEDs have preponderant long lifetime up to 100 000 hours, the most common symptom of failure is the gradual lowering of the light output and the efficiency loss. Sudden failure, unlike incandescent and fluorescent lamps, is rare. With the development of high-power LEDs, the devices are subjected to higher junction temperatures and higher current densities than traditional devices, this causes stress on the material and may causes early light-output degradation [25].

## 1.2 Optics Basics

This section discusses the geometric optics of an optical system based on reflection and refraction elements such as lenses and conical mirrors, to better understand of the thesis project, and the damaging effects of spherical and chromatic aberrations.

### 1.2.1 Geometrical optics

Geometrical optics is the geometry of light rays and their images, through an optical system [26]. It's possible to think of light as rays pointing along the direction of wave propagation. A closer look to light waves allows a better understanding of geometrical optics. A wavefront is defined as a locus of points that connect identical wave displacements, as seen in Figure 7.

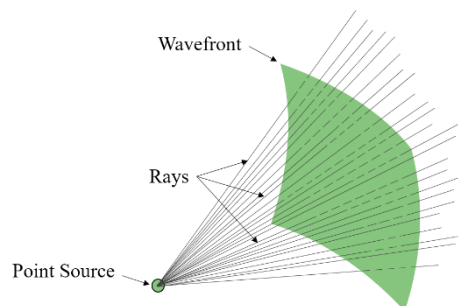


Figure 7: Rays and Wavefront generated by an emitting point source.

A ray is a line perpendicular to a series of successive wavefronts specifying the direction of energy flow in the wave. With the geometrical construct of a light ray it's possible to describe propagation, reflection and refraction of light [27]. Geometrical optics is a robust model and a practical tool to solve optical problems.

Reflection is the change of direction of electromagnetic radiation, such as light, by a surface upon which the radiation is incident. Depending on the sort of surface, reflection of light is either specular, as in mirrors, or diffuse, as in white marble. The law of reflection describes specular reflection. It states that the incident ray, the reflected ray and the normal to the reflecting surface all lie in one plane. And that the angle  $\theta_i$  between the incident ray and the normal is equal to the angle  $\theta_r$  between the reflected ray and the normal, as shown in Figure 8.

$$\theta_i = \theta_r \quad (\text{Eq. 8})$$

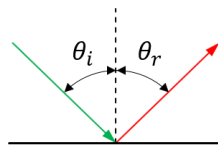


Figure 8: Geometry of specular reflection.

Opposing to specular reflection where an incident ray is reflected at only one angle, in diffuse reflection an incident ray is reflected in many angles.

Refraction is the change of direction of a wave at an interface between two optical media. An optical media can be described in terms of index of refraction, which is defined as the ratio between the speed of light in a vacuum and the speed of light in the medium,  $n = c_0/c_m$ . Air and most gases have an index of refraction nearly equal to one, while other materials have values greater than one. Snell's law shows that rays travelling from a lower index medium to a higher index medium bend toward the perpendicular to the interface. Calling the lower index of refraction  $n_1$ , the higher one  $n_2$  and the angle of refraction  $\theta_R$ . Snell's law states:

$$n_1 \sin(\theta_i) = n_2 \sin(\theta_R) \quad (\text{Eq. 9})$$

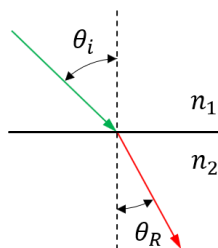


Figure 9: Geometry of refraction.

Figure 9 illustrates the refraction phenomenon, where a wave, propagating in the optical medium 1, approaches the boundary surface obliquely. The velocity of propagation of medium 2 is slower than in medium 1, which forces waves to slow down as they enter medium 2. This makes the direction of travel to bend towards the perpendicular of the surface boundary. By the contrary if the velocity of medium 2 is greater than that of medium 1 the direction of travel would bend outwards.

## 1.2.2 Lenses and Conical Mirrors

Elements useful to focus, diverge or collimate a light beam are lenses and conical mirrors, they allow rays inclination change, the first by exploiting the phenomenon of refraction through curved surfaces, and the second using reflection.

The lenses are classified according to the curvature of the two optical surfaces, in the following table the applications and the shapes of the most common are summarized [28].

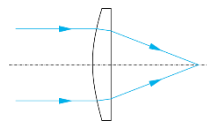
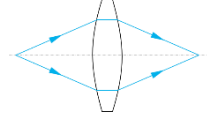
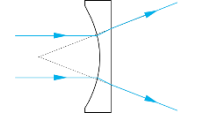
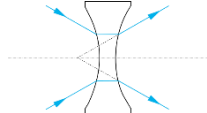
Lens	Focal length	Application	Form
Plano-Convex	Positive	Focusing a Collimated Beam; Collimating a Point Source	
Bi-Convex	Positive	Relay Imaging; Focusing a Divergent Beam	
Plano-Concave	Negative	Diverging a Collimated Beam; Collimating a Convergent Beam	
Bi-Concave	Negative	Relay Imaging; Diverging a Convergent Beam	

Table 2: Characteristics of common lens types.

The focal length ( $f$ ) is one of the main feature of lens and conical mirror, in the table above is defined positive or negative depending on its position on the lens axis of the object and for the converging (+) or diverging effects (-), as shown in the Figure 10. Other properties are:  $d$  the thickness of the lens (the distance along the lens axis between the two surface vertices),  $R_1$  the radius of curvature of the lens surface closer to the light source,  $R_2$  the radius of curvature of the lens surface farther from the light source [29].

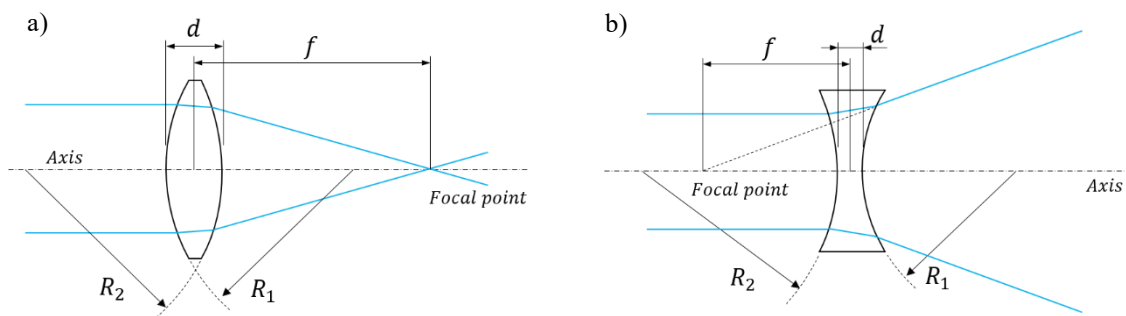


Figure 10: a) Positive-Converging lens; b) Negative-Diverging lens.

The focal length of a lens can be calculated from the Lensmaker's equation, where  $n$  as explained before is the refractive index of the lens material:

$$\frac{1}{f} = (n - 1) \left[ \frac{1}{R_1} - \frac{1}{R_2} + \frac{(n - 1)d}{nR_1R_2} \right] \quad (Eq. 10)$$

These elements are typical subjects to side effects caused by shape and material which are neglected in the simple analytic treatment but present in real behavior, below are reported two types of aberrations important for the thesis work.

**Spherical Aberration:** a type of aberration found in optical systems that use elements with spherical surfaces. Figure 11 illustrates a particular case of third-order spherical aberration in which the rays of light are parallel to the optical axis on the lens-side of the system.

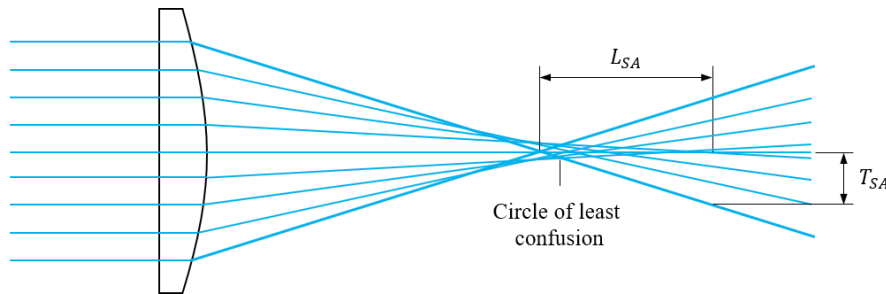


Figure 11: Longitudinal, transverse spherical aberration and the circle of least confusion for the lens.

The longitudinal spherical aberration  $L_{SA}$  is defined as the distance between the intersection of a ray with the optical axis and the paraxial focus. The transverse spherical aberration  $T_{SA}$  is defined as the perpendicular distance above (or below) the paraxial focus that a ray pass. The circle of least confusion is the region between the intersection of all the rays with the optical axis and the paraxial focus where the rays form their narrowest beam.

**Chromatic Aberration:** aberration caused by the dispersion of the lens material, the variation of its refractive index  $n$  with the wavelength of light

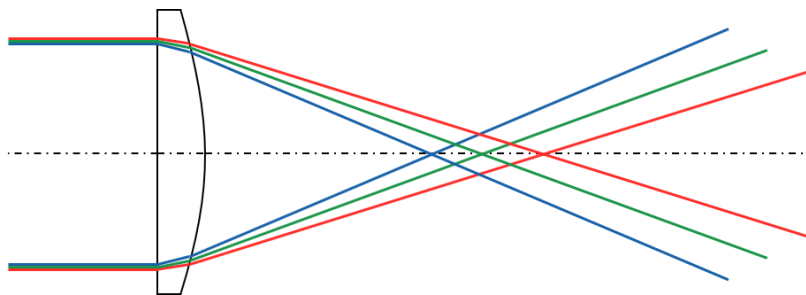


Figure 12: The undercorrected longitudinal chromatic aberration of a simple lens.

From the Eq. 10  $f$  is dependent upon  $n$ , it follows that light of different wavelengths is focused to different positions. Chromatic aberration of a lens is seen as fringes of colour around the image. It can be minimized by using an achromatic doublet in which two materials with differing dispersion are bonded together to form a single lens. This reduces the amount of chromatic aberration over a certain range of wavelengths, though it does not produce perfect correction. Different lens materials may be used to minimise chromatic aberration, such as specialized coatings or lenses made from the crystal fluorite. This naturally occurring substance has the highest known Abbe number, indicating that the material has low dispersion.

During the project two other types of lenses were used: Aspheric condenser lenses and Fresnel lenses. The first ones are ideal for collimating incoherent light from a lamp or LED, or similar light source with a highly uniform illumination pattern, they are designed for high-efficiency illumination applications and they offer reduced spherical aberration with large apertures and low f-numbers [30].

The seconds offer light focusing and collimation without the bulk associated with traditional lenses, their design allows the construction of lenses of large aperture and short focal length without the mass and volume of material that would be required by a lens of conventional design. A Fresnel lens can be made much thinner than a comparable conventional lens, in some cases taking the form of a flat sheet [31].

Other elements introduced before are the conical mirrors, also called spherical reflectors [29], two concave types were used during the project, one with a parabolic shape and the other elliptical, their applications are shown in Figure 13.

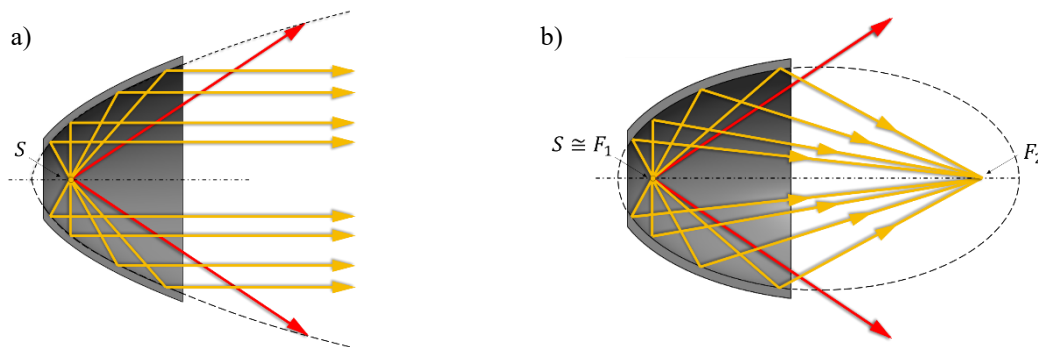


Figure 13: a) Parabolic reflectors; b) Elliptical reflector.

- a) A parabolic reflector is a reflective surface used to collect or project light energy, its shape is part of a circular paraboloid, that is the surface generated by a parabola revolving around its axis. They can be used to focus radiation from an isotropic source into a narrow beam.
- b) An elliptical reflector is a light control device with an ellipsoid shape, that collects light rays generated from a primary focal point and directs it to a secondary focal point.

These two mirrors are subjected as lens to spherical aberration but not to chromatic aberrations, that is produced when light passes through a material, this is also one of many reasons why large telescopes use mirrors rather than lenses for their primary optical elements [32].

### 1.3 Photonic Propulsion

Photonic propulsion systems use the force created by reflecting or emitting electromagnetic radiation for spacecraft propulsion, they are inherently propellant-less. Theoretical advantages of propellant-less propulsion systems are a general reduction of the system's complexity and mass as well as a significantly increased lifetime.

#### 1.3.1 Existing and Future Photonic Thrusters

Most designs currently in development consist of large reflective membrane sails to exploit the reflective radiation pressure either from the sun or laser systems. Two examples of existing spacecraft with photonic propulsion systems are the Japanese IKAROS spacecraft (launched 2010) [33] and the most recent LightSail 2 (launched 2019) [34].

The IKAROS probe was specifically designed to test solar sails as a main propulsion and power generation system for interplanetary missions. IKAROS' quadratic sail, measuring 20m in diameter and 7.5 $\mu$ m in thickness. The reflectivity of said panels was variable, thus allowing attitude control by applying different amounts of reflective radiation pressure on specific areas of the sail.

The LightSail 2 was designed to demonstrate controlled solar sailing in low Earth orbit, raising the orbit apogee and increasing orbital energy following sail deployment. The design challenge was to maximize the surface area of the sail while minimizing the mass of the spacecraft all while adhering to the standard 3-unit CubeSat size limitation. The photonic propulsor is composed by four triangular sails forming a square, measuring 8m in diameter and 4.5 $\mu$ m in thickness.

PACER is a new photonic propulsion system for AOCS [1], it consists of an electromagnetic radiation source, an optical accumulation and collimation system and a beam vectoring system (Figure 14). The currently preferred design uses an array of light-emitting diodes (LEDs) in the visible spectral range, specifically 100 Broadcom 3W LED Emitters. The produced light is then guided through optical fibers into a collimator array, where it is accumulated and aligned. The resulting light beam is then reflected off a pivot mirror into the desired thrust direction. With an approximate thrust generation of 3.3nN per Watt of radiation power, the thrust of PACER in this configuration ideally sums up to around 1 $\mu$ N.

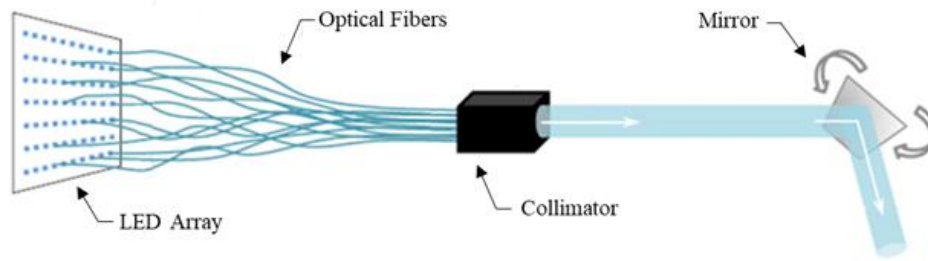


Figure 14: Schematic operation principles of PACER with LED array, accumulation and collimation system, and thrust vectoring system.

### 1.3.2 Physical Basics for Photonic Propulsion

Even though photons are inherently massless, each photon with a wavelength  $\lambda$  carries an impulse  $p_{photon}$  that can be described as

$$p_{photon} = \frac{h}{\lambda} = \frac{h\nu}{c_0} \quad (Eq. 11)$$

The force applied by a flux  $\phi$  of  $n$  photons within a time span  $t$  can be calculated with

$$F_\phi = \phi_{photons} \frac{h\nu}{c_0} = \frac{n}{t} \frac{h\nu}{c_0} = \frac{E_{photon}}{t c_0} \quad (Eq. 12)$$

with the energy  $E_{photon}$  from Eq. 1, the general relation  $P = E/t$  for power, the resulting force in dependency of the applied power  $\phi_e$  of an electromagnetic radiation source can be calculated:

$$F_\phi = \frac{\phi_e}{c_0} \quad (Eq. 13)$$

Eq. 13 shows that 1W of electromagnetic radiation corresponds to about 3.3 nN of force, so it could be defined an ideal force  $F_i$  depending on a constant  $\epsilon = 3.3 \text{ nN/W}$  and the radiant flux  $\phi_e$ .

$$F_i = \epsilon \phi_e = \left[ 3.3 \frac{\text{nN}}{\text{W}} \right] \phi_e \quad (Eq. 14)$$

This physical principle is the base for all photonic propulsion systems like PACER or photonic sails.

## 1.4 Torsional Pendulum Dynamics

A first research on existing thrust stands showed that usually they are based on torsional pendulum, so this section describes the torsional pendulum dynamics.

Torsional pendulum can be described by the general pendulum equation of motion for a second order system [35]:

$$I\ddot{\theta} + c\dot{\theta} + k_0\theta = F(t)R \quad (\text{Eq. 15})$$

where  $I$  is the system's moment of inertia,  $\theta$  the angular pendulum displacement,  $c$  is the system's damping constant,  $k_0$  the systems resulting spring constant and  $F(t)$  the force acting at a distance  $R$  from the pendulum's system of rotation and  $t$  the time variable, Figure 15 a). By adding the definitions of the damping coefficient  $\zeta$  and the systems undamped natural frequency  $\omega_n$ :

$$\zeta = \frac{c}{2} \sqrt{\frac{1}{Ik_0}} \quad (\text{Eq. 16})$$

$$\omega_n = \sqrt{\frac{k_0}{I}} \quad (\text{Eq. 17})$$

The differential Eq. 15 can be brought into the standard form:

$$\ddot{\theta} + 2\zeta\omega_n\dot{\theta} + \omega_n^2\theta = F(t)\frac{R}{I} \quad (\text{Eq. 18})$$

If a constant force  $F(t) = F$  is applied to the pendulum, the solution of the second-order differential Eq. 18, as found by Ziemer [4], is:

$$\theta(t) = \frac{FR}{I\omega_n^2} \left[ 1 - e^{-\zeta\omega_n t} \left( \cos(\omega_d t) + \frac{\zeta}{\sqrt{1-\zeta^2}} \sin(\omega_d t) \right) \right] \quad (\text{Eq. 19})$$

where  $\omega_d$  is the damped frequency that can be calculated with the natural frequency and the damping coefficient:

$$\omega_d = \omega_n \sqrt{1 - \zeta^2} \quad (\text{Eq. 20})$$

For steady-state measurements ( $t \rightarrow \infty$ ) the solution in Eq. 19 can be written as:

$$\theta(t \rightarrow \infty) = \theta_{ss} = \frac{FR}{k_0} \quad (\text{Eq. 21})$$

Ideal torsional pendulums are not affected by gravity and the Eq. 19 can be used to define the response of the system to an applied force for underdamped motion,  $\zeta < 1$ , Figure 15 b).

For torsional pendulums, especially the fiber-suspended type, additional equations can be used to describe the system properties. The angular pendulum displacement  $\theta$  of a torsion pendulum's swing arm can be calculated by the relation:

$$\theta = \frac{M_t}{k_0} = \frac{FR}{k_0} \quad (\text{Eq. 22})$$

with  $M_t$  being the torsional moment on the torsion spring,  $F$  the applied force and  $R$  the distance between the rotational centre of the system and the force's point of attack. For a fiber-suspended torsion pendulum the spring constant  $k_0$  can be further defined as:

$$k_0 = \frac{GJ}{L} \quad (\text{Eq. 23})$$

where  $G$  is the torsional modulus of the suspending fiber,  $J$  is the fiber's polar moment of inertia and  $L$  is the effective fiber length. Knowing the fiber effective diameter ( $d$ )  $J$  is defined as:

$$J = \frac{\pi d^4}{32} \quad (\text{Eq. 24})$$

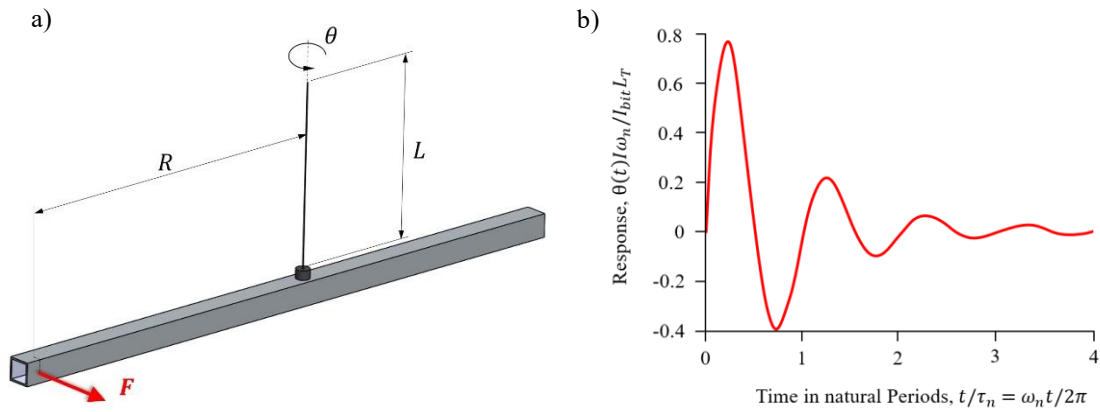


Figure 15: Torsional pendulum a) Characteristics; b) Response amplitude for damping coefficient  $\zeta < 1$ .

## 1.5 Existing Torsion Pendulum Thrust Balances

The following subchapter provides an overview of several existing torsion pendulum thrust balances, based on spring and fiber suspended, and their respective performances. With the growing demand for high precision micro- and nano-thrusters, highly accurate thrust and impulse measurement techniques become inevitable.

### 1.5.1 Overview

The most important requirements of a thrust stand are the high accuracy and reliability of the measure. Load cells are often used for high-level thrusters, where the applied force can be measured directly. For micro- and nano-thrusters and their extremely low thrust-to-weight ratio this method becomes no longer sustainable, as the thrust force is overwhelmed by the thruster's weight and other forces involved in the measurement process [35]. For that reason, indirect force measurements are preferred, where the applied thrust is calculated from the displacement of a pendulum or similar device. These devices can generally be split up into three different categories: hanging pendulums, inverted pendulums and torsional pendulums. These pendulums, all different configurations of a mass-spring-damper system, have implemented themselves as the most common and practical method for measuring low thrust levels. A selection of several existing torsional thrust balances sorted by year of publication, that are suitable for the targeted thrust range, is presented in the following sub-chapter. For each device is reported the type of thrusters that can be tested, size of the system, measuring and damping system characteristics, calibration mode, lowest thrust detectable and sensibility.

### 1.5.2 2001) nN Thrust Stand by Jamison, Ketsdever and Muntz [3]

The Nano-Newton thrust stand by Jamison, Ketsdever and Muntz was developed by the Department of Aerospace and Mechanical Engineering at the University of Southern California and the Air Force Research Laboratory Propulsion Directorate and it consists in a spring-suspended torsion pendulum. The goal of the development was the creation of a simple device to reliably measure the performance of MEMS fabricated systems, for example the Free Molecule MicroResistojet. The length of the swing arm was  $0.25\text{ m}$  completely symmetrical from the centre of rotation and it was suspended on two flexural pivots with a total approximate spring constant of  $0.0016\text{ Nm}/^\circ$ .

The thrust is calculated by measuring the linear displacement of the swing arm with a linear variable differential transformer (LVDT). With a linear displacement of the swing arm of  $0.264\text{ }\mu\text{m}$  at  $100\text{ nN}$  applied force.

A direct mechanical connection between the movable swing arm and the surrounding area (by powerlines and propellant feed lines) was bypassed by using a specially designed liquid oil bath. This bath acts as both liquid seal for propellant transfer and viscous damper for vibration damping, as shown in Figure 16. The liquid used for the bath was Dow Corning oil with a viscosity of  $10\text{ }000\text{ mm}^2/\text{s}$  and a specific gravity of  $0.971\text{ g}/\text{cm}^3$ . The oil was selected because of its high viscosity and low vapor pressure for operating in the vacuum chamber. The stand was calibrated by measuring the arm displacement produced by an under expanded orifice in the free molecule flow regime. The expected thrust of the orifice was prior determined using the Direct Simulation Monte Carlo numerical method (DSMC) with experimentally determined values as inputs for the simulation. The estimated calibration error, mostly a result of the experimental input values, was  $\pm 12.6\%$ . The thrust stand was installed in CHAFF-IV vacuum chamber at an ultimate pressure of  $1.33 \times 10^4\text{ Pa}$ .

The stand was capable of measuring forces as low as  $88.8\text{ nN}$  with an estimated error of  $\pm 16\%$  and  $734\text{ nN}$  with an estimated error of  $\pm 2\%$ .

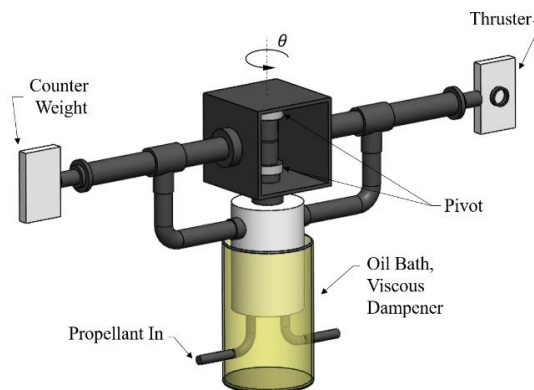


Figure 16: Schematic structure of the *Jamison et al.* thrust stand and its liquid seal damping system.

### 1.5.3 2001) Sub- $\mu\text{N}$ Thrust Stand by Ziemer [4]

The Sub-micro-Newton thrust stand by Ziemer was developed in the Advanced Propulsion Technology Laboratory at NASA Jet Propulsion Laboratory (JPL) and it consists in a spring-suspended torsion pendulum. The goal was the performance validations of devices such as vacuum arc thrusters (VAT), gas-fed pulsed plasma thrusters (GFPP), indium field emission electric propulsion thruster (In-FEEP), vaporizing liquid microthruster (VLM), and a micro-cold gas thruster developed by Moog, Inc. The test mass or thruster is mounted to a horizontal arm which is supported

by two flexural pivots as shown in Figure 17. To reduce the influence of gravity, the thruster is counter-balanced so the centre of mass (CG) of the entire thrust arm is close to the pivot axis.

A LVDT with sub-micron resolution is used to interpret the linear voltage output proportional to position, this system measures the linear displacement instead of the angular displacement that is calculated knowing the distance of measuring point from the rotational axis. In case of small deflections ( $\theta < 4^\circ$ ) the position can be determined within 0.1%.

The external damping system of the pendulum is based on damping coils. The calibration is made supplying a known impulse to the thrust arm by a piezoelectric force transducer mounted at the end of a rod called the “calibration hammer,” as shown in Figure 17. The mounting rod is blocked at an angle by an electromagnet that is switched off to release the hammer. Upon impact, the transducer outputs a voltage proportional to the instantaneous force which can then be integrated to determine the calibration impulse. The impulse magnitude can be changed by changing the cocking angle of the electromagnet.

The resolution of the stand has been characterized experimentally as  $< 1 \mu N$  for steady-state thrust measurements and  $< 1 \mu N$  for impulse measurements.

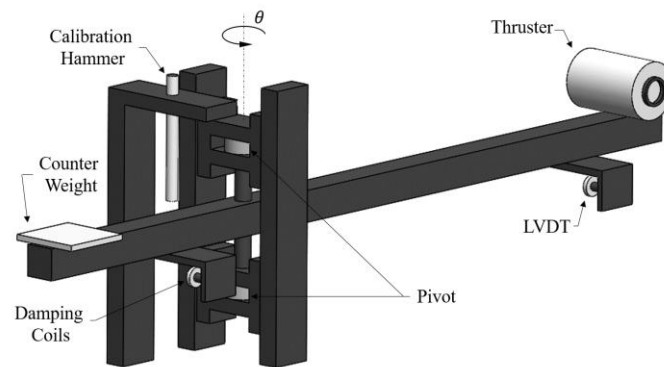


Figure 17: Schematic design of the *Zierner* thrust stand configuration.

### 1.5.4 2002) nN Thrust Stand by Phipps and Luke [6]

The Nano-Newton thrust stand by Phipps and Luke was developed by Photonic Associates LLC in collaboration with the University of New Mexico and it consists in a fiber-suspended torsion pendulum. This thrust stand was developed to accurately measure the performance of their newly developed laser plasma thruster (LPT). The LPT works through laser ablation, a method in which a laser is focused on an ablative plate, emitting a directed plasma jet in the process. The swing arm is hung on a  $78 \mu m$  diameter fused silica fiber.

The angular deflection of the swing arm is measured by reflecting a  $1 W$  probe laser off a micro-mirror located at the swing arm’s centre of rotation onto a ruled chart mounted to the inside of the vacuum chamber. The angular resolution of this method was approximately  $210 \mu rad$ .

The upper end of the fiber is fixed in a fiber vise, while at the lower end a stabilization mass is submerged in an oil bath for vibration damping. The calibration was made observing the pendulum’s resonant frequency and calculating the effective rotating mass applying a known force with a standard pendulum, with an estimated calibration error of 5%. The system was housed in a vacuum chamber at a constant pressure of  $4 \times 10^{-2} Pa$ .

The maximum resolution of the thrust stand was stated to be  $4\text{ nN}$ . The lowest detectable thrust was not officially stated but corresponds to approximately  $6.6\text{ nN}$ .

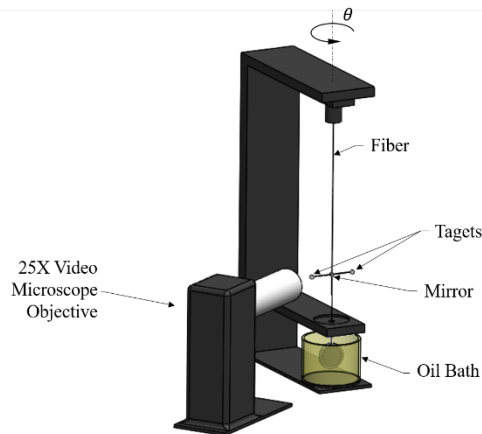


Figure 18: Schematic design of the First *Phipps et al.* thrust stand configuration.

### 1.5.5 2003) $\mu\text{N}$ Thrust Stand by Lake, Cavallaro and Spanjers [5]

The Micro-Newton thrust stand by Lake, Cavallaro and Spanjers was developed in the Air Force Research Laboratory at Edwards Air Force Base and it consists in a spring-suspended torsion pendulum. The goal of the development was the creation of a device to reliably measure the performance of micro pulsed plasma thrusters (uPPT). The torsion springs used are two Lucas Aerospace 5016 – 800 torsional pivots. Roll and pitch locations of the swing arm are adjustable via two stepper motors.

The displacement of the swing arm is measured using a LVDT. Instead of measuring the displacement of the swing arm at a steady-state, this design measures the amplitude of the swing arm in a resonating state. The thruster mounted on the swing arm is fired in resonance with the systems oscillation. This leads to an amplification of the oscillation amplitude of the swing arm, creating a forced harmonic oscillator. With this method the oscillating system is mostly insensitive to outside vibrations and only the difference between the oscillation's minima and maxima is measured.

An automatic routine was developed for thrust stand calibration, where an electromagnet, attached to the thruster position of the swing arm via a  $0.13\text{ mm}$  fishing line over an aluminum pulley, pulls up a calibration weight. The magnet is activated when the swing arm is moving in the same direction as the force applied by the thruster. The amplitude is stored, and the cycle repeated until an asymptotical limit is reached. Then the entire process is repeated for a different calibration mass. The results are used to create a calibration curve. The thrust stand operates in a vacuum chamber at a pressure between  $4 \times 10^{-3} - 8 \times 10^{-3}\text{ Pa}$ .

The thrust stand can achieve a measurement resolution of  $0.04\ \mu\text{N}$  with an estimated accuracy of  $\pm 1.3\%$  for forces of  $5\ \mu\text{N}$ .

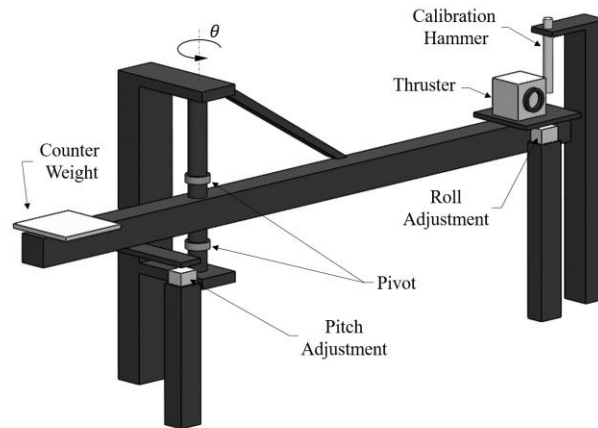


Figure 19: Schematic design of the *Lake et al.* thrust stand configuration.

### 1.5.6 2003) Sub- $\mu$ N Thrust Stand by Gamero-Castaño [8]

The Sub-Micro-Newton thrust stand by Gamero-Castaño, M. was developed at the Massachusetts Institute of Technology supported by a NASA Phase II SBIR and it consists in a spring-suspended torsion pendulum. The goal of the development was the performance validations of devices such as colloid thrusters and FEEPs. A symmetric aluminium arm, with a colloid source in one of its ends, is fixed to the balance frame by means of two flexural pivots. Each pivot has a nominal torsional spring rate of  $1.6 \times 10^{-3} \text{ Nm/}^\circ$ , and can hold an axial load of up to  $20 \text{ N}$ . The motion of the arm is constrained by the pivots to rotation only. As a reference, the length and height of the arm are  $48 \text{ cm}$  and  $22 \text{ cm}$  respectively.

The measuring system was based on a fiber optic displacement sensor (LDS) for measuring the angular displacement of the balance's arm with a resolution of  $5 \text{ nm}$  in the DC-100 Hz range up to  $0.15 \mu\text{m}$  at a frequency of  $200 \text{ kHz}$ .

The external damping circuit can apply a torque proportional to the angular velocity of the balance arm. It consists in an electrode facing the right side of the balance's arm, the voltage of this electrode is determined by an electronic circuit that takes the displacement of the arm as an input, computes its derivative, and generates a positive high voltage signal proportional to it. The calibration of the system is made using the electrostatic force between two charged electrodes. A base of a cylindrical electrode with a diameter and a height of  $12 \text{ mm}$  and  $13 \text{ mm}$ , is fixed to one side of the balance's arm, at  $21 \text{ cm}$  from its axes. A second larger electrode, physically isolated from the balance, faces it. The thrust stand has been tested in a cylindrical vacuum chamber with a diameter of  $0.66 \text{ m}$ , length of  $0.77 \text{ m}$  and pressure of  $1.3 \times 10^{-3} \text{ Pa}$ .

It can be measured comfortably thrust values as low as  $0.11 \mu\text{N}$  with a resolution of  $0.01 \mu\text{N}$ , which were generated with a single emitter colloid source.

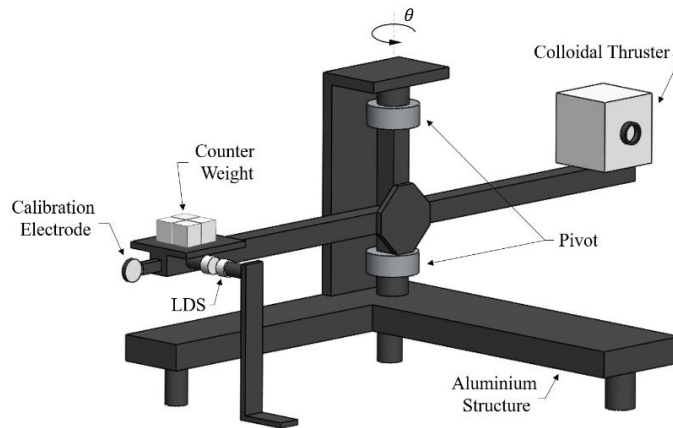


Figure 20: Schematic design of the *Gamero-Castaño* thrust stand configuration.

### 1.5.7 2006) nN Thrust Stand V2.0 by Phipps, Luke and Helgeson [7]

This thrust balance is essentially an upgraded version of the system presented in Subchapter 1.5.5. The thruster and the power supply are both mounted on the swing arm, eliminating the need for a physical connection between the movable arm and the surrounding other than the supporting fiber. The total mass of the swing arm accumulated to 15 kg. The swing arm is suspended from a steel fiber, measuring 254 μm in diameter and 40 cm in length. The fiber upper end is attached to a frame, supporting the entire setup.

The angular deflection is measured via a newly designed device roughly based on a Mach-Zehnder interferometer. At the centre of the arm's rotation, a corner-cube reflector is attached. The other three optical components necessary for such an interferometer are installed outside the vacuum chamber. This optical measurement method can register angular deflections as low as 2 μrad, about one order of magnitude lower than necessary for the targeted thrust stand resolution.

The whole system is critically damped, by submerging a flag, roughly mounted directly under the thruster's centre of thrust, into an oil bath. The thrust stand was calibrated using the magnetic torque between two Helmholtz coils. The large coil was in a fixed position, while the second, small coil was mounted directly to the swing arm of the balance. Calibration errors were estimated to be ±10%.

The balance was able to resolve force changes of 25 nN with a lower force limit of around 100 nN.

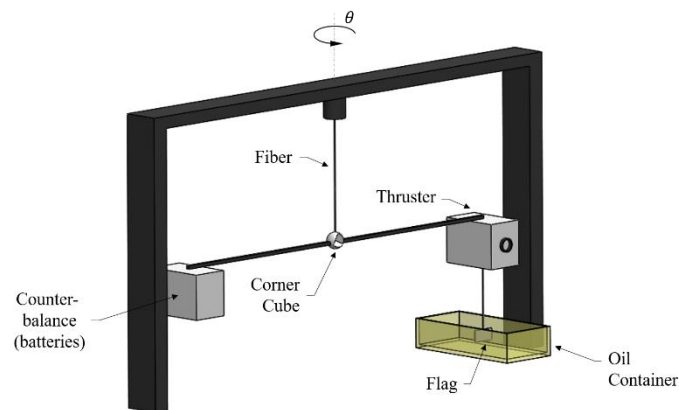


Figure 21: Schematic design of the Second *Phipps et al.* thrust stand configuration.

### 1.5.8 2012) $\mu\text{N}$ Thrust Stand by Y. Yang, Tu, S. Yang, Luo [9]

The Micro-Newton thrust stand by Y. Yang, L. Tu, S. Yang and J. Luo was developed in the School of Physics at Huazhong University of Science and Technology and it consists in a fiber-suspended torsion pendulum. The goal of the development was the ground testing of micro-Newton pulsed plasma thrusters (PPT) developed for Chinese TEPO mission. The pendulum body is made of an aluminium rectangular block with dimension of  $27 \times 3 \times 6 \text{ cm}^3$  approximately that is suspended by a tungsten fiber with a length of  $1160 \text{ mm}$  and a diameter of  $(502.0 \pm 6.1) \mu\text{m}$  with torsion spring constant  $k = 8.47 \times 10^{-4} \text{ Nm/rad}$ .

A PPT is mounted on one end of the pendulum, and the nozzle axis is aligned to be a tangent to the twist motion of the pendulum. When the thruster is firing, the pendulum responds by rotating about the fiber axis, the angular displacement of the pendulum is monitored by an electronic autocollimator ELCOMAT vario 140/40 with a measurement range of  $\pm 2880 \text{ arcsec}$  and an accuracy of  $2 \text{ arcsec}$ .

An  $850 \text{ g}$  copper counterweight is mounted on the opposite side of the PPT in order to balance the weight of the thruster and adjust the attitude of the pendulum by adjusting the four copper nuts, which makes the thrust vector both vertical to the gravity vector and tangent to the twist of the pendulum. The upper end of the fiber is connected to a rotational vacuum feedthrough fastened on the top of the vacuum chamber, which is used to adjust the initial amplitude and position of the pendulum. No information was reported on the damping system used in this thrust stand. The calibration method is based on a pair of electrostatic actuators, parallel to the pendulum surface with a gap of  $4 \text{ mm}$  to form the differentially capacitive transducer, that is used to adjust the amplitude of the pendulum for the impulse and the thrust measurements in open loop mode conveniently. In closed-loop mode, the electrostatic actuators are used to balance the pendulum in the null position by using a proportional integral differential (PID) compensator. The system was housed in a vacuum chamber at a constant pressure of  $1 \times 10^{-3} \text{ Pa}$

The thrust stand can measure impulses up to  $1350 \mu\text{N}$  with a resolution of  $0.47 \mu\text{N}$ , and the thrust up to  $264 \mu\text{N}$  with a resolution of  $0.09 \mu\text{N}$ , which is limited by the accuracy of angular measurement.

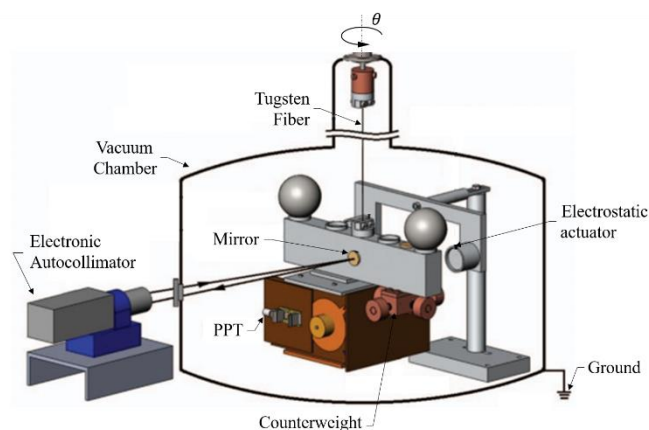


Figure 22: Schematic design of the *Yang et al.* thrust stand configuration.

### 1.5.9 2013) Sub- $\mu\text{N}$ Thrust Stand by Soni and Roy [10]

This thrust stand, called APRG- $\mu\text{N}$ TS (Applied Physics Research Group micro-Newton thrust stand) by Soni and Roy was developed by the University of Florida and it consists in a spring-suspended torsion pendulum. The goal of the development was the testing of plasma micro-thrusters called the

Free Molecular Electro Jets (FMEJ) capable of delivering sub-micronewton level thrust for nanosatellites. The length of the swing arm was  $0.285\text{ m}$  and the torsional springs, which provide the restoring force for the system with spring constants of  $0.0036\text{ Nm}/^\circ$  and an error of  $\pm 10\%$ .

The angular displacement of the arm was measured using the Philtec Model D-100 linear optical displacement sensor.

An electromagnetic eddy-current damping system was used for vibration damping. The damper consisted of a strong neodymium permanent magnet ( $B_{surface} = 0.6619\text{ T}$ ) and a cylindrical copper block (diameter  $63.5\text{ mm}$ , height  $31.75\text{ mm}$ ). The relative motion of the block and the magnet, produced by oscillations in the swing arm, induce eddy-currents in the copper block. These currents generate their own magnetic field, countering the applied field and providing damping. The thrust stand was calibrated using the logarithmic decrement method. This method estimates the spring constant of the system, by backing out the system's damping ratio based on successive peaks of oscillation in conjunction with the measured damped frequency. The result of the logarithmic decrement method was then compared to an electrostatic calibration method. The system was housed in a vacuum chamber sized  $25 \times 25 \times 56\text{ cm}^3$ .

The thrust stand was capable of measurements with a resolution of  $0.01\text{ }\mu\text{N}$  and lowest thrust of  $1.3\text{ }\mu\text{N}$ .

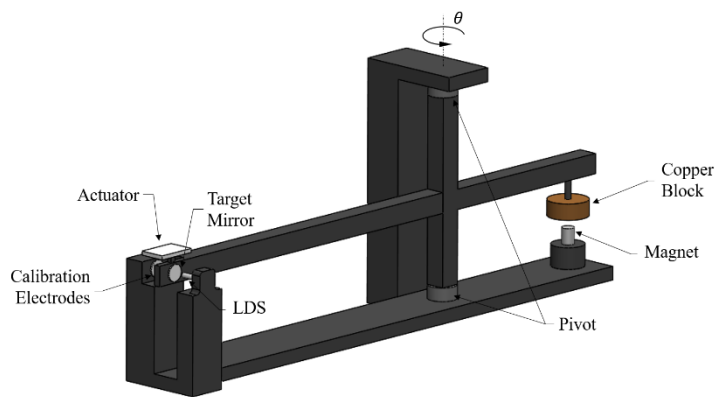


Figure 23: Schematic design of the *Soni and Roy* thrust stand configuration.

### 1.5.10 Summary

The following table provides an overview of the most important properties of the thrust balances previously presented.

As before the devices are sorted by year of publication, in order to better understand the table below a legend has been created:

- a) Spring-suspended=Spr-Susp;
- b) Fiber-suspended=Fib-Susp;
- c) Not mentioned=Nm.

Year	Author/ Team	Operation Principle	Resolution (nN)	Lower thrust limit (nN)	Measurement technique	Damping system	Calibration Source
2001	<i>Jamison et al.</i> [3]	Spr-Susp. Steady-state	Nm	88.8	LVDT	Viscous (oil bath)	Orifice Thruster
2001	<i>Ziemer</i> [4]	Spr-Susp. Steady-state	Nm	1000	LVDT	Damping coil	Impact Pendulum
2002	<i>Phipps and Luke</i> [6]	Fib-Susp. Steady-state	4	6.6 (Ideally)	Laser deflection	Viscous (oil bath)	Known Force
2003	<i>Lake et al.</i> [5]	Spr-Susp. Resonant	40	5000	LVDT	-	Calibration Weight
2003	<i>Gamero-Castaño</i> [8]	Spr-Susp. Steady-state	10	110	Optical LDS	Electrostatic	Electrostatic
2006	<i>Phipps et al.</i> [7]	Fib-Susp. Steady-state	25	100	Mach-Zehnder interferometer	Viscous (oil bath)	Magnetic Torque
2012	<i>Yang et al.</i> [9]	Fib-Susp. Steady-state	90	Nm	Autocollimator	Air Damping	Free Oscillations
2013	<i>Soni and Roy</i> [10]	Spr-Susp. Steady-state	10	1300	Optical LDS	Electromagnetic (eddy-current)	Log Decrement

Table 3: Overview of existing concepts for thrust stands in the sub micro-Newton range based on torsion pendulum sorted by year.

## 2 Requirements and Boundary Conditions

For the design of a completely new thrust stand it was necessary to define the requirements and the boundary conditions of the system, this was made using information from an old thesis work made on this project and the one collected after the research on real thrust stands, Chapter 1.5. Also, the preliminary ideas, formulated when it was conceived the intention to build a thrust stand for future electromagnetic radiation thrusters, were used to define the thrust stand conditions. In this chapter are presented the initial requirements from which the thrust stand project started, during the development of the project other were defined.

### 2.1 Requirements

Starting from the idea of a real thrust stand where the purpose is to have a system able to carefully measure the thrust of the tested elements, it was observed that the first requirement that could also be called “the principal one” was the sensibility of the system. In Chapter 1.5 micro- and nano-Newton real thrust stand with sensibility from 4 nN up to 100 nN were analysed, these values were obtained using different technologies. Considering that the thrusters that will be tested could potentially be used for mission where are demanded better accuracy than the one requested by Lisa Pathfinder AOCS [2], an ideally resolution of 10 nN was established.

To reach this resolution it was analysed the chosen measurement system, that depended on the chosen type of thrust stand. The one designed in this thesis is a fiber suspended pendulum, so it should be designed a measurement system able to measure the angular displacement made by the pendulum’s arm with a sensibility of 10 nN.

Another factor that was decisive for the operation of the project was the minimal force that could be detected by the system, as could be seen from the Table 3 in Chapter 1.5.10 the lower thrust limit depends by the type of torsional pendulum chosen. From the research it was established that the best values are reached by fiber instead of spring-suspended torsional pendulum. Considering that this stand was designed to test photonic thrusters that generate sub micro-Newton forces, the lower thrust limit was set at 50 nN.

In order to obtain that limit a fiber with a low value of elastic constant should be used, so an analysis on this constant should be required and the purpose of that should be to find fibers that permit to measure small forces for big angular displacement. Also, this value influences the response time of the pendulum, the system should provide a short time from resting to measurement position, that could be obtained by designing a good damping system, and a short relaxation time. It is recommended to balance calibrate the system before a new measurement and to make it in a short time. Working on these time spans could increase the efficiency of the thrust stand allowing more tests in small time.

A maximal force limit should be set in order to design the maximal radiation power generated by the experimental damping system radiation source.

Another necessary requirement was the tensile strength of the fiber that should be able to support the weight of the pendulum’s arm, from a first evaluation on existing thrusters it could be seen that this weight value is usually elevated. The one chosen was based on the *Phipps and Luke* system that had requirements and size like the one projected here.

The last requirements that were followed during all the project design were the simplicity of the system operations and assembly, and the preference for high efficiency but low-cost solutions.

In Table 4 are reported the requirements of the system:

Requirements	
Sensibility of the system	10 nN
Lower thrust limit	50 nN
Fiber elastic constant	low to measure 10 nN displacement
Time spans	< 15 minutes
Upper thrust limit	maximum value damped
Fiber Tensile strength	withstand < 20 kg
Simplicity and high efficiency	easy assembly
Cost	< 2 000 €

Table 4: Thrust stand requirements.

## 2.2 Boundary Conditions

The thrust stand will work in a vacuum chamber to not have the damaging effects of air resistance, so the first boundary condition described are the ones inside the vacuum chamber and then outside, or rather the conditions of the Lab where the chamber is placed.

In the vacuum chamber the pressure is close to 0 Pa and its size were supposed to be  $2 \times 1 \times 0,5 \text{ m}^3$ , due to the absence of air the heat exchange can be made only by contact and radiation, all the components of the stand should be prepared to work in these conditions.

Outside the vacuum chamber it was hypothesized the Standard Ambient Temperature and Pressure, temperature of  $25^\circ\text{C}$  and ambient pressure of 1 bar.

Boundary conditions		
Vacuum Chamber	Pressure	Close to 0 Pa
	Size	$2 \times 1 \times 0.5 \text{ m}^3$
	Heat exchange	Contact or radiation
Outside Chamber	Pressure	1 bar
	Temperature	$25^\circ\text{C}$

Table 5: Thrust stand boundary conditions.

### 3 Thrust Balance model

In this chapter are presented the building of the pendulum simulator and some tests on how could work the system. In the first subchapter are reported all the data of the pendulum, the equations used to build the simulator and an analysis on the energy of the system, then in the second there were evaluated 2 possible configurations of the damping system. The first possibility was a constant damping force acting on the arm for a time equal to half a period of the pendulum and changing value at the end of that time, the second one was a fixed force activated in the same time of the one before but with value modulated in frequency. At the end are presented the conclusion of that simulations and a first evaluations on the real damping system.

#### 3.1 Specifics

In this subchapter as explained above are presented all the parameters used to model the thrust balance and how was build the MATLAB model.

The thrust balance is based on a fiber-suspended torsion pendulum, the model is like the Philips and Luke system, the thrusters and the power supply are both mounted on the swing arm, but with an active damping system based on the emission of LEDs electromagnetic waves.

The data of the pendulum were obtained from a previous thesis work on this system, the length of the pendulum's arm is 1.5 m with lever length of 1 m. The swing arm is a hollow aluminium profile, with square cross section, outer width of 4 cm and inner width of 3 cm. The total mass of the pendulum was estimated of 7.5 kg, and this value was fundamental for the calculation of the spring constant of the fiber and the inertia of arm.

The following table shows the data used to simulate the pendulum with a MATLAB model:

Lever length (m)	1.00
Mass (kg)	7.50
Inertia (kg m <sup>2</sup> )	1.41
Spring constant (Nm/°)	1.714 x 10 <sup>-5</sup>

Table 6: Pendulum data.

The first hypothesis is that the fiber damping ratio is neglected, considering that the real pendulum in the vacuum chamber doesn't have air resistance so that the damping ratio of the fiber is close to 0.

The second and third hypothesis come from the small force values of the thrusters that will be tested, so it is possible to use the theory of small oscillation, the pendulum from now on is considered as a linear system and the Superposition principle is applicable [36].

First it was developed a model with a damping ratio of  $\zeta = 0.3 - 0.5$  to have an idea of how should work the system in case of undamped oscillations, from Eq. 18  $F = F_{test}$  is the force made by the thruster that the system is going to measure. It was decided to model an undamped oscillation cause to the uncertainty of the future damping system behaviour, it was supposed that a damping ratio  $\zeta > 0.5$  would have required a high light radiation source difficult to find or design, as confirmed in the conclusion of this chapter.

$$\ddot{\theta}_{id} + 2\zeta\omega_n\dot{\theta}_{id} + \omega_n^2\theta_{id} = \frac{F_{test}R}{I} \quad (Eq. 25)$$

then there were calculated the external forces  $F_m$  needed each half oscillation period to emulate the previously ideal damping. Forces that should be generated by the high-powered source's radiations of the external damping system which strike on a mirror placed on one extreme of the arm, at the same length of the thruster,  $R$ . In Figure 24 the positions of the thruster and the mirror are shown.

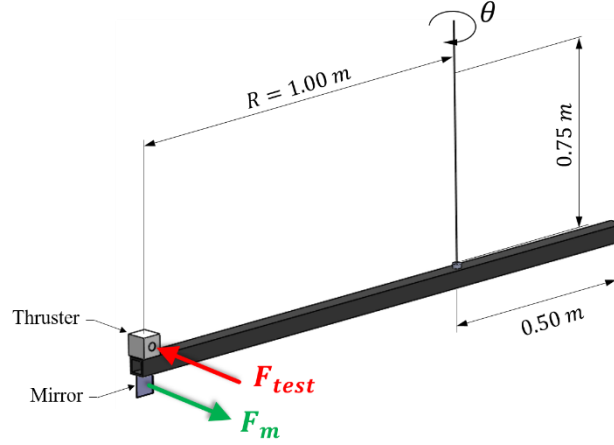


Figure 24: Pendulum diagram.

Starting from the no damped system equation and its solution  $\theta_0$ :

$$\ddot{\theta}_0 + \omega_n^2\theta_0 = \frac{F_{test}R}{I} \quad (Eq. 26)$$

$$\theta_0 = (1 - \cos(\omega_n t)) \frac{F_{test}R}{I\omega_n^2} \quad (Eq. 27)$$

defined  $m \geq 1$ , the number corresponding to the damping force active in a given half period, or rather in the second half period from  $T/2$  to  $T$  the damping force  $F_{m=1}$  is active, then in the third from  $T$  to  $3/2 T$  the force  $F_{m=2}$  is active and so on.

Defining  $\theta_{im(m)}$  the displacement made by each  $F_m$ , the displacement after  $n$  external damp forces  $\theta_{(m)}$  could be calculated:

$$F_{(m)} = (\theta_{id} - \theta_{(m-1)})_{t=T/2(m+1)} \frac{k}{2R} \quad (Eq. 28)$$

$$\theta_{im(m)} = (1 - \cos(\omega_n(t - T/2 m))) \frac{F_{(m)}R}{I\omega_n^2} \quad (Eq. 29)$$

$$\theta_{(m)} = \begin{cases} \theta_{(m-1)}, & t < T/2 m \\ \theta_{(m-1)} + \theta_{im(m)}, & t \geq T/2 m \end{cases} \quad (Eq. 30)$$

In this way is possible to know each half period which damping force is acting and how it is changing the final displacement  $\theta_{(m)}$ .

In Figure 25 is shown a graph with the damping forces depending on time for  $m=3$ , in the first  $T/2$  no damping force is acting so  $F_{m=0} = 0$ , from  $T/2$  to  $T$  the  $F_{m=1}$  is pointing in the same direction of  $F_{test}$  because the idea is to slow the movement of the arm moving in the opposite direction, then  $F_{m=2}$

is opposite to  $F_{test}$  and so on. For that reason, it was decided to use a convention:  $F_{(m)} > 0$  when pointing in the same direction of  $F_{test}$ , and negative if on the contrary. That explained also why the force  $F_{m=2}$  is greater than  $F_{m=1}$ .

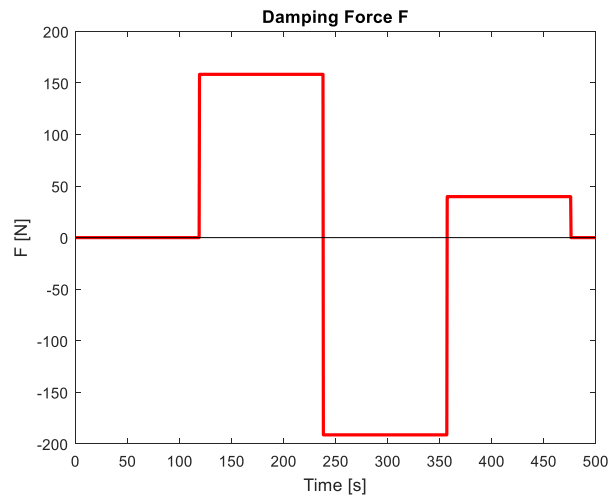


Figure 25: Example of  $F_m$  for  $m = [1\ 2\ 3]$  and  $F_{test} = 500\text{nN}$ .

After the model was rebuilt to simulate the real test condition, the first half period the pendulum is not damped, then when the maximum displacement is reached the program analyses the data about time, displacement, velocity and acceleration to obtain the experimental values of spring constant and a first data about the thrust that is measured. With these values the program calculates the forces  $F_m$  needed to damp the system for a previously chosen damp ratio, and an estimation of the relaxation time.

The program shows in a graph the evolution of angular displacement  $\theta_m$ , angular velocity  $\omega_m$ , angular acceleration  $\alpha_m$  and the damping force  $F_m$ , in Figure 26 is simulated  $F_{test} = 500\text{nN}$  for  $m=3$  while in Figure 27 in red are shown the  $\theta_{im(m)}$  for  $m=[1\ 2\ 3]$  and in blue the  $\theta_{(m)}$  for  $m=[0\ 1\ 2]$ .

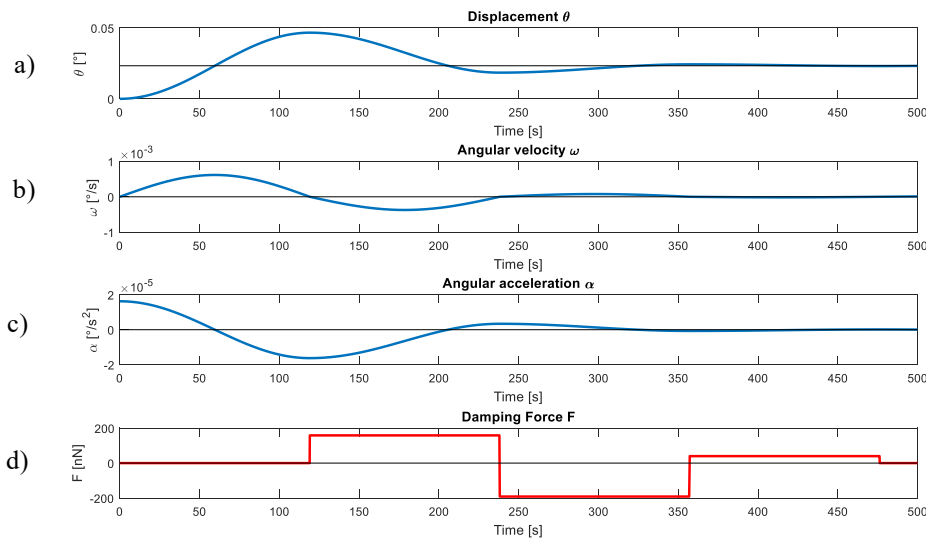


Figure 26:  $F_{test} = 500\text{nN}$  and  $m=[1\ 2\ 3]$  a) angular displacement  $\theta_m$ ; b) angular velocity  $\omega_m$ ; c) angular acceleration  $\alpha_m$ ; d) damping force  $F_m$ .

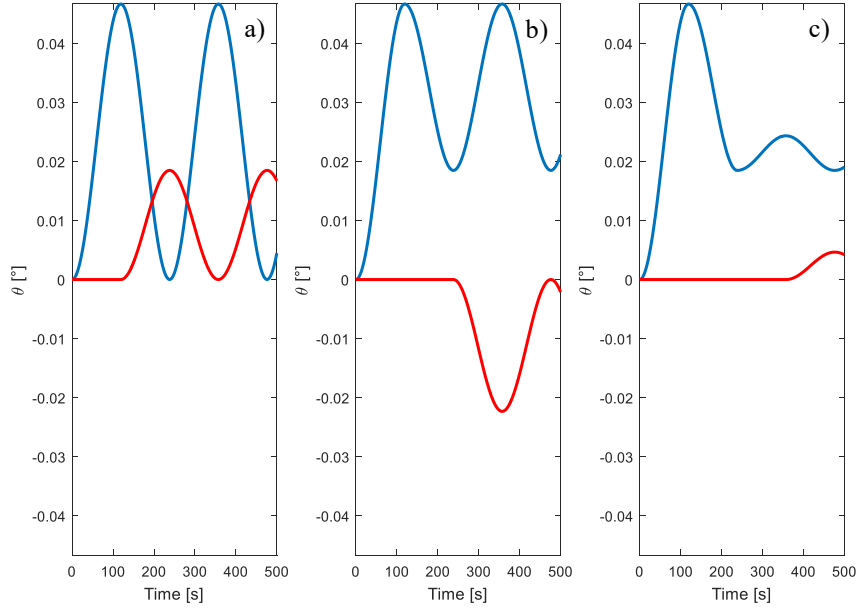


Figure 27: Example for  $F_{test} = 500\text{nN}$  how work the damping system: blue  $\theta_m$ , red  $\theta_{im(m)}$  a)  $\theta_0$  and  $\theta_{im(1)}$ ; b)  $\theta_1$  and  $\theta_{im(2)}$ ; c)  $\theta_2$  and  $\theta_{im(3)}$ .

As explained before it is possible to see that the forces  $F_m$  are activated every time that the angular velocity is 0, their values are constant during all the half period of activation, in this way the forces slow down the swing arm up to allow the measurement of the thrust  $F_{test}$  at relaxation time.

To have information about energy of the system  $E$  it is not possible to use the Superposition principle so the interactions between the response were considered, it's possible to calculate the potential energy  $U$  for  $m \geq 0$ :

$$U_m = \frac{1}{2} k \theta_m^2 \quad (Eq. 31)$$

The first half period it is not damped so for the conservation of energy  $E_0$  is the total energy of the system, then when the external forces started to hit the swing arm there is no more conservation of energy, and it's not possible to calculate the total Energy  $E_{tot}$ .

$$E_0 = \frac{1}{2} k (\theta_0)_{t=T/2}^2 \quad (Eq. 32)$$

After the experimental relaxation time the value of the energy will be close to ideal:

$$E_f \sim \frac{1}{2} k \left( \frac{F_{test} R}{I \omega_n^2} \right)^2 \quad (Eq. 33)$$

In Figure 28 are reported the damping force  $F_m$  and the potential energy of the system  $U_m$  during time, the third graph is the potential energy of the system  $U_m$  depending on displacement.

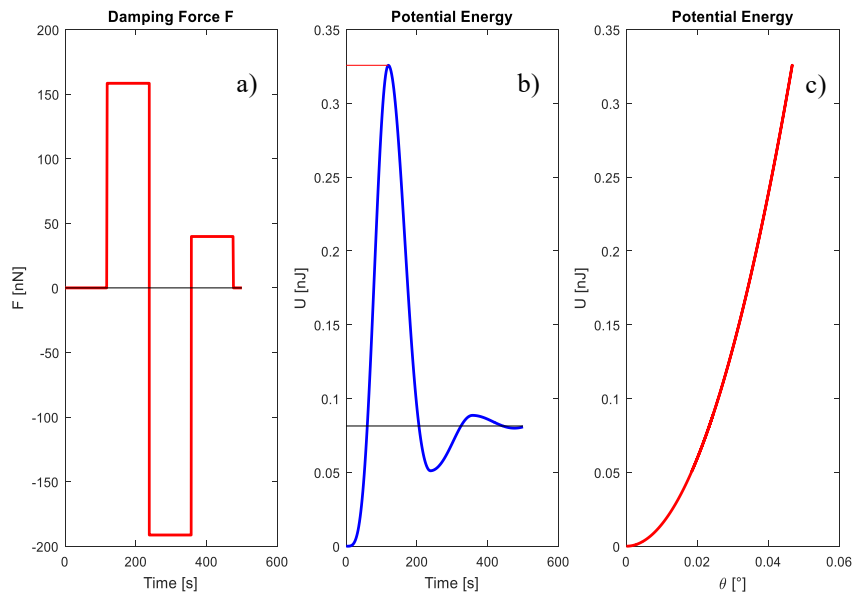


Figure 28: a) Damping force  $F_m$ ; b) Potential energy of the system  $U_m$  during time; c) Potential energy of the system  $U_m$  for displacement.

### 3.2 Possible Damping Cases

Defined a working model it was analysed the possibility to damp the system using a specific force each half period or a pulsed force that changing the frequency and the effective number of pulses reach the same result.

This analysis is crucial to define the light source, because using a specific force for each half period involves that the power of the high light source should be controlled on magnitude to generate a specific electromagnetic radiation, on the other side the source should be controlled on frequency.

To be clearer, in the first case each half period the light source generates an individual square pulse for a time that is exactly half of a period, in the second case the light source generates a constant periodic square pulse.

In the next figure are shown the first case on the left, one force constant for all the half period, and the other one on the right, constant force control in frequency.

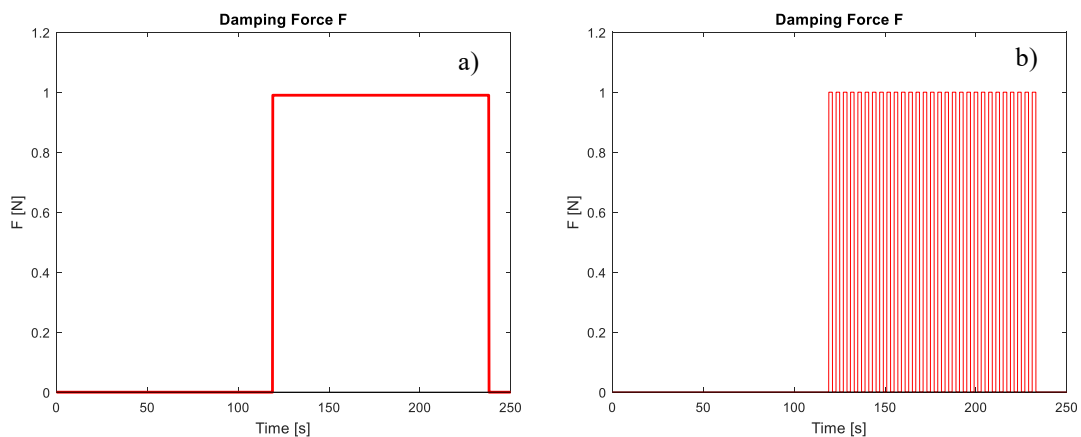


Figure 29: a) First case: Single pulse, magnitude control; b) Second case: Multiple pulses, frequency control.

To set the analysis it was necessary to define a minimum and maximum force that the system would have been able to measure, from the requirements a minimum force of 50nN and a maximum of 500nN were chosen. From the theory using the *Eq. 14* knowing the maximum force, it is possible to define the electromagnetic radiation power emitted by a light source, ideally a power of 150W is needed to generate 500nN of thrust.

The choice of the maximum and the minimum is also important to prove that the initial hypothesis made in the previous subchapter can be used, the displacements made by these thrusts are reported below:

	Force [nN]	Displacement [°]
Minimum	50	0.0029°
Maximum	500	0.0290°

Table 7: Angular displacements produced by maximum and minimum thrust

the values of the angles are very low, so it is possible to use the previous hypotheses of small oscillation and Superposition principle.

For the next simulation was chosen a damping ratio  $\zeta = 0.5$ .

### 3.2.1 First case

An individual square pulse is acting during a time  $t_d$  that is exactly half oscillation period  $t_d/T = 0.5$ , the displacement made by the impulse for  $t < t_d$  is  $\theta_{im}$ :

$$\ddot{\theta}_{im} + \omega_n^2 \theta_{im} = \frac{F_{im}R}{I} \quad (Eq. 34)$$

$$\theta_{im} = (1 - \cos(\omega_n t)) \frac{F_{im}R}{I\omega_n^2} \quad (Eq. 35)$$

when the impulse load is no longer acting  $t \geq t_d$ , the system is responding in free vibration and the response of the system become [36]s:

$$\theta_{im} = (\dot{\theta}_{im})_{t=t_d} \sin(\omega_n \bar{t}) + (\theta_{im})_{t=t_d} \cos(\omega_n \bar{t}) \quad (Eq. 36)$$

with  $\bar{t} = t - t_d$ .

For  $t_d/T = 0.5$ , the angular velocity  $(\dot{\theta}_{im})_{t=t_d} = 0$ , and the angular displacement  $(\theta_{im})_{t=t_d} = 2 \frac{F_{im}R}{I\omega_n^2}$ , so the dynamic amplification is  $D = 2$  and the response for  $t \geq t_d$  is:

$$\theta_{im} = \cos(\omega_n \bar{t}) 2 \frac{F_{im}R}{I\omega_n^2} \quad (Eq. 37)$$

This is confirmed also from the figure below where for rectangular pulses at  $t_d/T = 0.5$  the amplification is double.

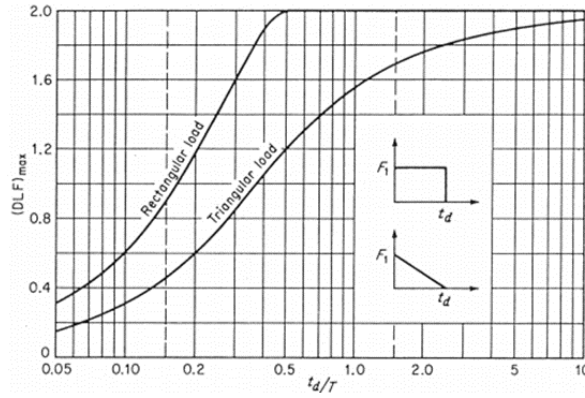


Figure 30: Maximum elastic response, rectangular and triangular load pulses [36].

then using the Superposition principle this response is sum to the undamped response, the result is identical to the one calculated in the previous subchapter,  $F_{im} = F_{(m)}$  for  $m \geq 1$  :

$$\theta_{(m)} = \begin{cases} \theta_{(m-1)}, & t < T/2 m \\ \theta_{(m-1)} + \theta_{im(m)}, & t \geq T/2 m \end{cases} \quad (Eq. 38)$$

Then it was made a simulation for the minimum 50nN and the maximum 500nN thrusts tested, considering the linearity of the system the results are proportional and in Chapter 3.3 is reported the simulation for the minimum.

### 3.2.2 Second case

A periodic square pulse has a period of  $2t_d$ , where  $t_d$  is the time of each singular pulse, for  $t < t_d$  and  $t \geq t_d$  like before the system is working with the Eq.s 34, 35, 36 but the value of the angular velocity is different from zero and the dynamic amplification is less than before [36]:

$$(\dot{\theta}_{im})_{t=t_d} \neq 0 \quad (Eq. 39)$$

$$D = 2\sin\left(\pi \frac{t_d}{T}\right) < 2 \quad (Eq. 40)$$

Considering that the response of the system after each pulse is always the same:

$$\theta_{im(m)} = \begin{cases} 0, & t < 2t_d(n-1) \\ (\theta_{im})_{(t-2t_d(m-1))}, & t \geq 2t_d(n-1) \end{cases} \quad (Eq. 41)$$

it is possible to sum the responses of all the pulses every period  $2t_d$  obtaining the displacement called  $\theta_{p(m)}$  until the maximum of that is equal to the  $\theta$  needed to damp the system:

$$\max\left(\theta_{p(m)} = \sum_{a=1}^b \theta_{im(a)}\right) = (\theta_{id} - \theta_{(m-1)})_{t=T/2(m+1)} \quad (Eq. 42)$$

Also, in this case  $|F_{im(t>T/2)}| = \text{const.}$ , for  $m \geq 1$ :

$$F_{im(m)} = \begin{cases} + |F_{im(t>T/2)}|, & T/2(2m-1) < t \leq T/2(2m) \\ - |F_{im(t>T/2)}|, & T/2(2m) < t \leq T/2(m+1) \end{cases} \quad (Eq. 43)$$

then using the Superposition principle, the response  $\theta_{p(m)}$  is sum to the undamped response,  $m \geq 1$  :

$$\theta_{(m)} = \begin{cases} \theta_{(m-1)}, & t < T/2 m \\ \theta_{(m-1)} + \theta_{p(m)}, & t \geq T/2 m \end{cases} \quad (Eq. 44)$$

As in the previous case it was made a simulation for the minimum and the maximum thrusts tested, also here for the linearity of the system the results are proportional and for that in the following chapter is reported only the simulation for the minimum 50nN.

### 3.3 Conclusions

In Figure 31 and Figure 32, in the next page, are reported the simulation for the first and second case with  $F_{min} = 50nN$ , while in the table below are reported the maximum values of  $F_{(n)}$  calculated in the two simulations for  $F_{test}$  minimum and maximum:

	Case	$F_{min} = 50nN$	$F_{max} = 500nN$
$F_{(m)} max$	First	20 nN	200 nN
	Second	60 nN	600 nN

Table 8: Results of the two cases simulated.

The data forces  $F_{(m)}$  needed to obtain the same damping ratio for each case, so same displacement  $\theta_{(n)}$ , were analysed and from Figure 31 d) and Figure 32 d) and the data in the Table 8 above it was confirmed that the second case needs forces that are almost three times bigger than the first, and that its values should be bigger than the force made by the thruster tested.

In the following consideration it was assumed that the hypothetical high light power source could have been a LED. Due to the difficulty to find info about its electromagnetic radiated power everything was referred to the electrical power using a first approximation, it was chosen an average efficiency of 40% (other 60% lost in heat) [37].

In the first case for  $F_{max}$  is needed a damping force  $F_1 \sim 200nN$ , that corresponds to 40% of the max thrust, from Eq. 14 60.61 W of light power should be needed, so the needed electrical power should be of 151.51 W. Thanks to the scalable nature of the system for the minimum  $F_{min} = 50nN$ , as show in Figure 31 d)  $F_1 \sim 20nN$  so 15.15 W of electrical power are needed.

In the other case to damp is needed a force  $F_1 \sim 600nN$  that corresponds to 120% of the max thrust, emitted radiated power of 181.82 W, then for LED efficiency 40% the needed electrical power is 454.55 W. It is not possible to use  $F_1 \sim 600nN$  to damp the system for  $F_{min}$  and for that as shown in the Figure 32 d) it was chosen  $F_1 \sim 60nN$ , which for the same reasoning as before has an electrical power of 45.46 W.

From this last part and the basics of Chapter 1.1 it was established that:

- is difficult to control in frequency a high intensity light source to damp the  $F_{min}$ ;
- more than one light source for the second case should be needed to reach the same result of the first one;
- is hard to find a LED with that elevated electrical power and having a small size;
- the use of high frequencies may not allow the achievement of the right junction temperature for the correct operation of the LED, resulting in incorrect and non-constant radiation.

After these considerations it was chosen to use the first case to develop the damping system.

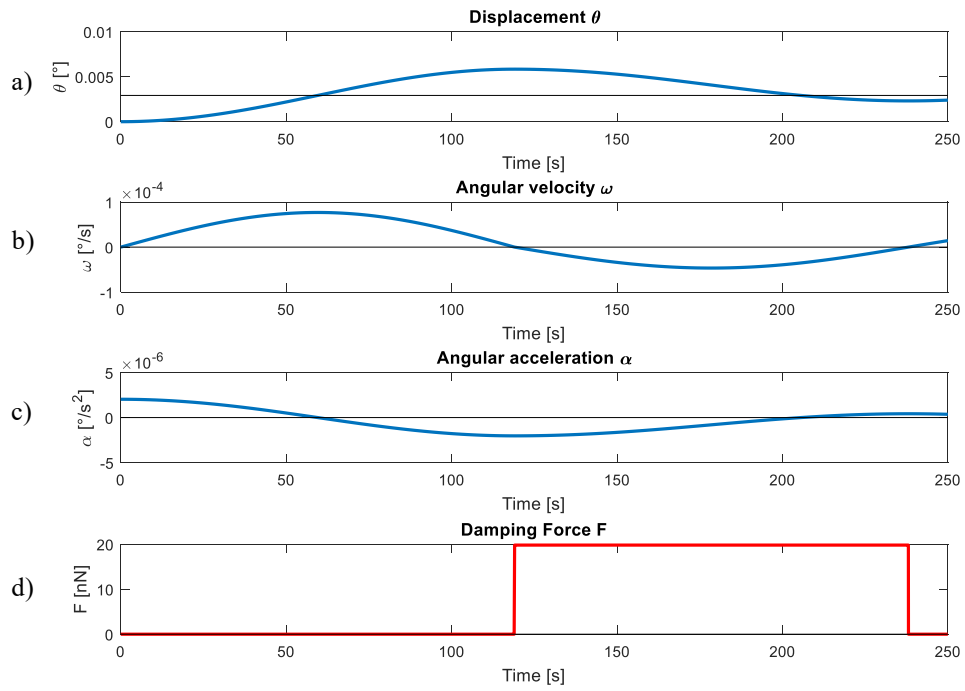


Figure 31: First Case:  $F_{min} = 50\text{nN}$  and: a) angular displacement  $\theta_m$ ; b) angular velocity  $\omega_m$ ; c) angular acceleration  $\alpha_m$ ; d) damping force  $F_{(m)}$ .

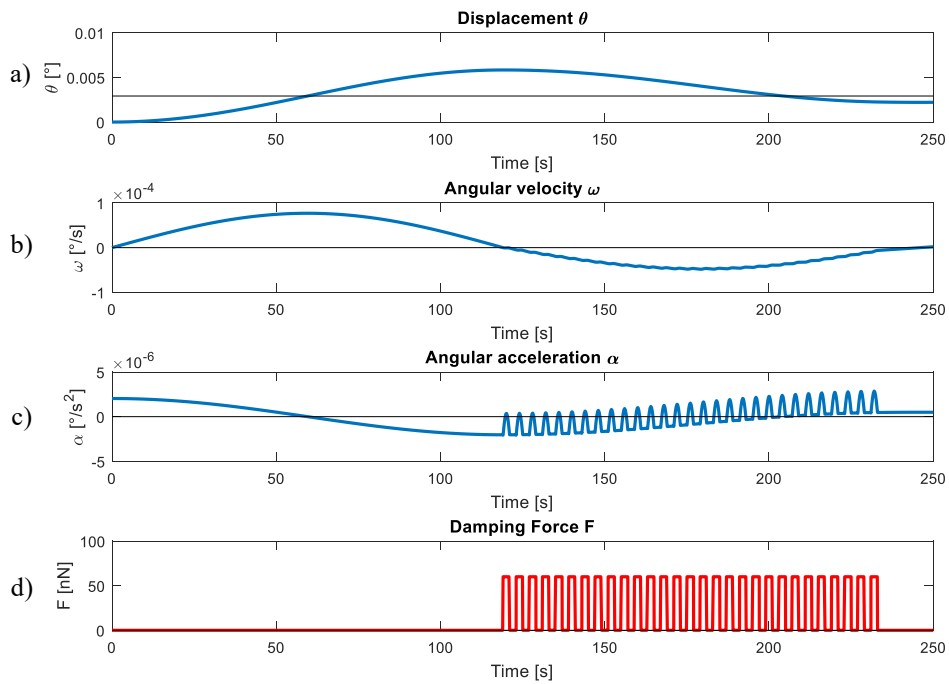


Figure 32: Second Case:  $F_{min} = 50\text{nN}$  a) angular displacement  $\theta_m$ ; b) angular velocity  $\omega_m$ ; c) angular acceleration  $\alpha_m$ ; d) damping force  $F_{(m)}$ .

## 4 First Concept

This chapter is a first analysis of the components required to design the thrust balance and it is structured in this way: at first an analysis on the specifics of the system, where are reported all the general information data on the components and on the project; after a research on the existing LEDs and its performance in order to project an efficient damping system; then a primary evaluation of the thrust balance cost; finally are reported the system changes after a meeting where the results of this chapter analysis were exposed. Particularly attention was posed on the design of the measurement system and damping system. During the project design the requirement and boundary conditions exposed in Chapter 2 were followed.

### 4.1 Specifics

The research started from the existing thrust balances shown in Chapter 1, each system was made by a combination of common sub-systems that can be summarized in: pendulum's arm, measurement system and damping system. The thrust balance presented in this chapter is composed by:

- 1) a fiber suspended pendulum's arm with thruster and the power supply both mounted on the swing arm;
- 2) a measurement system able to measure the small angular displacement of the pendulum's arm generated by thrusters up to 500 nN with a sensibility of 10 nN;
- 3) an external damping system working on the emission of electromagnetic light radiation made by a high light source power (potentially by LEDs).

The analysis on the swing arm is not reported because was already described in Chapter 3.

#### 4.1.1 Measurement system

In Chapter 1 were analysed the measurement systems of real thrust balances, the technologies used were inductive electromagnetic sensor (LVDT), laser deflection, optical linear displacement sensor (LDS), Mach-Zahner interferometer and autocollimator. The last one can measure the angular displacement by laser or LED deflection at the rotation centre of the swing arm.

Starting from the requirements in Chapter 2 a sensibility of 10nN is needed, the model developed in Chapter 3 permit to define the angular displacement for this sensibility:

$$\theta_{sen} = 0.000583^\circ \quad (Eq. 45)$$

The sensibility of 10nN was reached by the *Phipps and Luke* [6], the *Gamero-Castagno* [8] and *Soni and Roy* [10] thrust balances. The first one using a laser deflector and the last two using optical LDSs. A simple temporal analysis, as shown in Table 3, has result that the most recently used technologies are autocollimator and optical LDS. These two types were analyzed, also considering the elevated angular sensibility and accuracy of the recent autocollimators.

The thrust stand of this thesis is based on a fiber suspended, so it is more similar to the one of *Yang et al.* [9] compared to that of *Soni and Roy*, based on a spring suspended. Anyway, a research on LDSs having the angular sensibility  $\theta_{sen}$  was made but with negative results. Despite having with *Soni and Roy* the same sensibility requirement, a different angular sensibility requirement is generated by the different pendulum size and suspended type. So, they weren't chosen as measuring system.

Also, laser deflection was not chosen, because the electronic autocollimator represents an evolution of this technology, greater precision and a digital data collector. So, an autocollimator was chosen as the best measuring system solution for the thrust stand.

### Existing high-resolution autocollimators

An autocollimator as the thrust stand designed by *Yang et al.* was chosen as first solution to reach the high sensibility, for this kind of technology is good to use the unit arcsecond,  $\theta_{sen} = 2.0988''$ .

In their project *Yang et al.* used the autocollimator “ELCOMAT vario 140/40” with high measurement resolution selectable from 0.005 '' up to 10'', a recommended resolution of 0.5'' and a measuring uncertainty of  $\pm 2''$  [38]. They finally reach a resolution of 90nN, but considering the differents data on fiber suspended, inertia and size of the arm of this project it will probably lead to a different result. One advantage of the autocollimator line “vario” of ELCOMAT is that it can be used at different distances from the interested point, 0.3m up to 3 m, and mains voltage between 90 up to 250V at 50 or 60 Hz. On the other side exist a line “direct” of ELCOMAT with a fix max distance and main voltage of 5V via USB, for example the “ELCOMAT direct 140/40” has a maximum measurement distance of 0.75m [39].

In Figure 33 is shown the selection criteria of ELCOMAT autocollimators depending on measuring accuracy and measuring range that was found online on the company website.

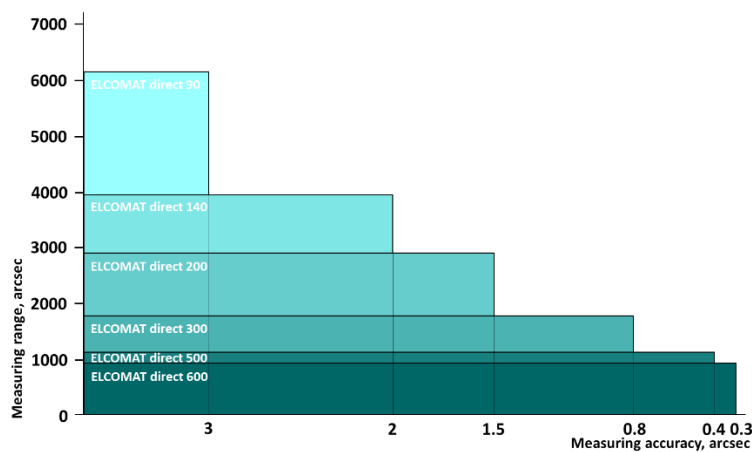


Figure 33: ELCOMAT autocollimator model choice depending on measuring accuracy and range [39].

Considering that this measurement system needs a resolution at list of 2'' and that the maximum angular displacement made by  $F_{max} = 500nN$  is  $\theta_{max} = 0.058^\circ = 208.8''$ , the measuring range is between  $-208.8''$  and  $208.8''$ , so 417.6'' a ELCOMAT direct 140 or 200 could be fine.

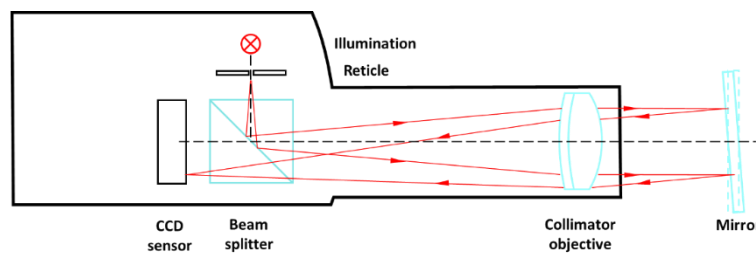


Figure 34: Measuring principle of the autocollimator [39].

In Figure 34 is shown how these autocollimators work, they measure the deflection of a LED beam on a mirror that could be fixed on the rotation centre of the swing arm.

One problem is that these types of autocollimators are not prepared to work in a vacuum chamber, so they should work outside like in the *Yang et al.* project. That make the location of the autocollimator at a variable large distance from mirror and that could explain the choice of *Yang et al.* to use a vario instead of a direct.

After a research on autocollimators with sensibility  $\theta_{sen}$  and able to work in a vacuum chamber was made. An excellent result could be the “TriAngle TA 100-38” with high measurement resolution 0.10 '' and accuracy of 2.5'', that is prepared for an ambient pressure between 0 to 0.1 bar so could be used inside the vacuum chamber. TriAngle has a program online to custom the autocollimator on the accuracy parameters [40].

From this analysis it resulted that using an autocollimator could be a good way to reach the sensibility of 2'', also it could be used to measure the displacement of the arm in a 2D (two dimensions) plane providing in the future more complex thrust tests. Another advantage is that the high measuring range up to 4000'' could allow the measure of a bigger  $F_{max}$  up to  $9.52\mu N$ .

Big problem of this technology is the expensiveness, the price of the ELCOMAT direct 140/40 is starting from 8 880 €, with higher price for higher resolutions, while the TriAngle TA 100-38 is more expensive starting from 11 100 €, as well higher price for higher resolutions.

To elaborate the data coming from the autocollimator a computer is needed, these data should enter in the MATLAB program described in Chapter 3, that could control the power output of the high-power source of the damping system as analysed next.

#### 4.1.2 High Powered light source

The high-powered light source is the innovative part of the project because it will be in charge of radiation power generation that will be used as force opposing the pendulum’s arm movement, damping the system. The goal of this research part was to find a source with elevated radiation power, in order to obtain an elevated damping force.

First, the research started from the Planck relation, that expresses the value of the photon energy  $E$  depending on the  $h$  plank costant and its frequency  $\nu$ , *Eq. 1*. From that relation it is possible to say that lowest is the value of  $\lambda$  and bigger will be the value of  $E$ , considering that  $h$  and  $c_0$  are costant in a vacuum. As explained in Chapter 1.1 the wavelengths that can be generate by LEDs are limited and it was made an analysis on the possible ones.

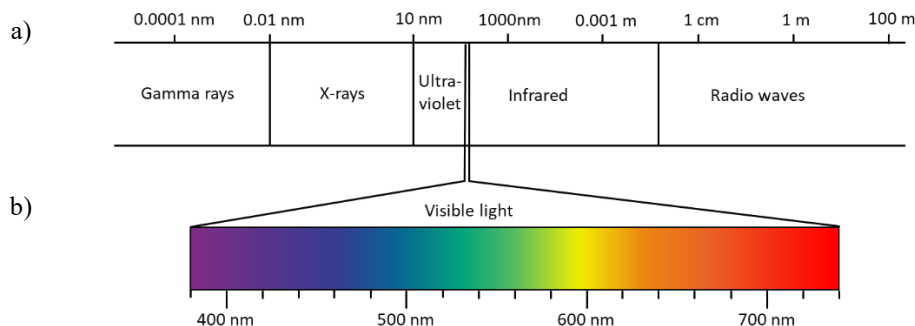


Figure 35: a) Electromagnetic spectrum b) Visible spectrum.

As shown in Figure 35 the wavelengths’ interval between 390 nm and 700 nm (colours from violet red) is the visible spectrum where are present the colours that can be seen by the human eye, usually LEDs produce radiations in this spectrum because of their common utilization in ambient lighting.

## Existing high-powered light sources

A research was carried out on existing high-power light sources with low wavelength radiation, this for the high energy emitted in this range, here are reported 2 of the best examples found online:

- 1) Prizmatix UHP-T2-LED-White with an ultra-high-power white LED (50 W of electrical power) produces a collimated optical power output  $> 2.5$  W, so an efficiency 5% [41];
- 2) Prizmatix UHP-Mic-LED-405 with an ultra-high-power violet LED (32W) that produce a collimated optical power output  $> 2.0$  W, so efficiency 6.25% [42].

For the low efficiency of these ones and their non-predisposition to work in a vacuum chamber a new light source was needed to be design, the idea was to use the same technology of the thrusters that will be tested on this thrust stand, or rather a new kind of Nano Newton thrusters propelled by electromagnetic radiation from a light source.

The research continued looking for LEDs with a wavelength between 400 nm and 500 nm, close to the violet and blue colour, also looking for white LEDs with an elevated value of colour temperature. That could be obtained by a blue LED die coated with yellow phosphor or a specific combination of Blue, Green and Red colours, the LEDs manufacturing methods where explained in Chapter 1.1.

For a White LED higher is the colour temperature value and more will be the power of the Blue light emitted, while on the contrary for lower values more will be the power of Red light emitted, as shown in Figure 3. For what explained before Blue radiation is more powerful than Red, so there were preferred White LEDs with high colour temperature also called “cold” white.

The value of the wavelength is a good start point to define the power emitted by ideal LEDs while for real light source the information given by the seller is required. Usually in the datasheet of a common LED there is information about the total amount of light emitted. For diodes with a wavelength close to the Ultra-Violet light is reported the information about the electromagnetic power emitted in Watt (W). While for the LEDs emitting visible light often is expressed the value of the total quantity of visible light emitted in Lumen (lm), this is due to the common use of these sources.

For this project is important to know the value of radiant power emitted by LEDs, but this can't be obtained only knowing the value in Lumen. Because an integration of the specific electromagnetic spectrum emitted by the LED is needed, for monochromatic light it is easier bur for white LEDs became more complicated. During the project when it was impossible to obtain or calculate this value for missing of data, it was supposed and efficiency of 40% [37], as made in Chapter 3.3.

## Light Transport and Collimation

Ones defined the kind of light that should be used, it became necessary to define how this light would have been transported by the source to the strike point in one extreme of the pendulum's arm. High power LEDs with high efficiency are usually the COB (Chip On Board), disadvantages of this configurations are the elevated beam angle that could be up to  $120^\circ$  [43]. For the project is preferred a light beam angle as possible close to  $0^\circ$  and a small strike area, so if the COB LEDs are used, a light collector will be needed.

First idea was to use a model like the one presented for PACER [1], there it was evaluated the possibility to transport the light via optical fibers to an optical collimator, in order to have a final collimated beam of light that could have been directed by reflection on a mirror Figure 14. For the thrust stand project, the final reflected beam could be used to hit a point of the arm damping the system.

## **Radiation Power Control**

After it was analysed how control the power emitted by the high source, to change the damping force of the system, the most simple way is to control the electrical power sent to the LED but considering that a specific output is needed and that the input data are coming from a computer after the elaboration of autocollimator data, a digital control is required. This digital control could be made by an Arduino, it is possible to PWM (Pulse Width Modulation) to change the brightness of the LED and accordingly change the light power emitted [44].

For LED until 100W is possible to PWM using an Arduino but for bigger power specific and more expensive components are needed [45]. There is not a linear proportion between the electromagnetic power emitted by the LED and the electrical power consumption of the source, as explained in Chapter 1.1. That for the technology of the diode that emit for values above a certain voltage, so ones defined a real system the power radiated should be tested.

## **Junction Temperature Control**

In order to guarantee the correct working of the LED, avoiding the change of the junction temperature which would lead to a variation of the radiated power, a cooling system is needed (Chapter 1.1). At the end of the Chapter 3 it was obtained the maximum value of the electrical power needed to damp, 151.51 W. As explain before as first approximation the 60% of this power will be converting to heat, so at least 91 W should be dissipated. In this case it was important to consider the boundary conditions inside the vacuum chamber, the heat could have been transfer only for conduction or radiation, so the following possibilities were evaluated:

- a) Water cooling system;
- b) Cooling block;
- c) Force heat transfer with a Peltier cell.

For each possibility heat pipes or conductive blocks could be used to transfer the heat from the LED back surface to the cooling system.

The water cooling system would be composed by a pump, a water reservoir and a radiator to ensure the water to air heat exchange, collocated outside the vacuum chamber, then 2 tubes water In and water Out would be connected to a cooling block attached to the backside of the LED inside the chamber.

As second solution it was evaluated a Cooling block that could be used to control the LED temperature, for example an aluminium block at a specific low temperature could be located inside the vacuum chamber attached to the backside of the diode, the heat produced would be transferred to the block and during the test period the Cooling block would increase its temperature matching an equilibrium.

The third was a Peltier cell that could be used to force the transferring heat from the LED. To force the transfer of 91 W of heat more electrical power should be used, a cooling system should be designed to cool the cell inside the vacuum chamber for a cooling power bigger than just the once produced by the diode. Due to this disadvantageous effect this solution could be used only to force the heat transfer.

### 4.1.3 Light Transport Through Mirror Reflection

Once the collimated light beam is produced it is necessary to define how this would hit the extreme of the swing arm, as mentioned before mirrors could be used to easily direct the light.

The pendulum is moving in one direction, so the beam will hit a surface perpendicular to the pendulum movement decreasing the velocity of the arm, 5 mirrors would be used to direct the beam instead of 2 LEDs located in opposite direction, parallel to movement directions of the arm. This idea provides less power consumption and it does not require another or bigger cooling system for a second LED, it guarantees more free space in the vacuum chamber and it is simpler to control. One disadvantage is that a pivot mirror is necessary to direct the beam.

The system includes 4 fixed mirrors and 1 pivot mirror as shown in Figure 36, which can be moved by a servomotor controlled by an Arduino, to have a digital control of the angular rotation

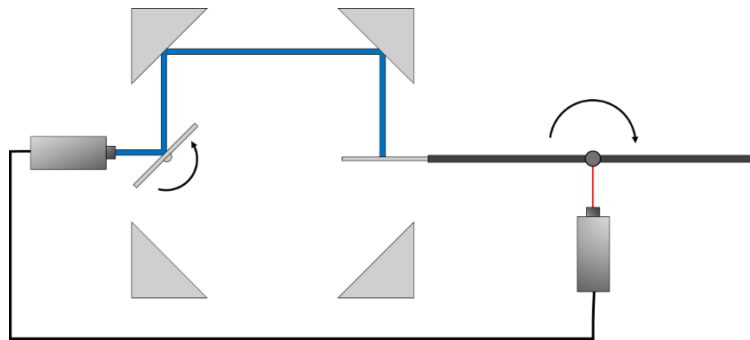


Figure 36: Mirrors schematic configuration of thrust stand.

### 4.1.4 Software and Hardware

As explained before the angular displacement data detected by the autocollimator are sent to a computer, then the MATLAB script made in Chapter 3 could be used to calculate the force needed to damp the system, and after an Arduino could sent an electrical signal to drive the LEDs and to move the pivot mirror in the correct position.

### 4.1.4 Summary

In Figure 37 are reported the data path and the light path of the system, the first highlights the exchange of data between the elements of the thrust balance, the second shows the elements that deal with directing the light beam. The last cell on the right is the mirror located on one extreme of the arm, as explained in Chapter 3.1 is the element that transmits the force of light to the swing arm.

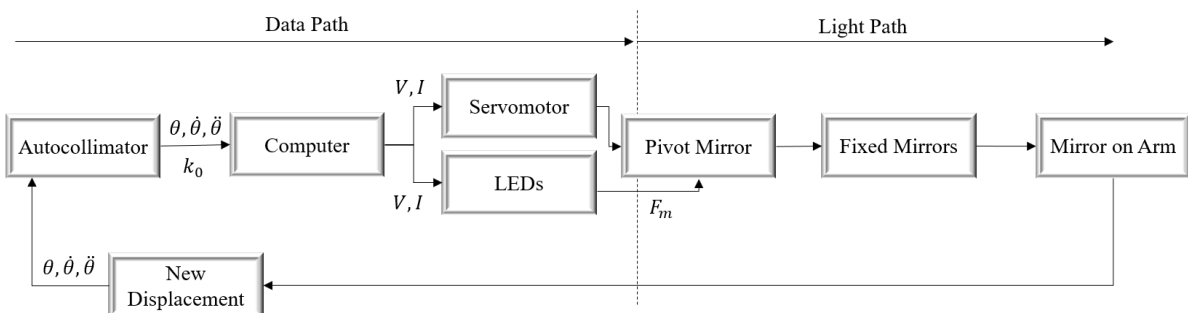


Figure 37: Data path and light path of the system.

Everything starts from a New displacement made by the thrusted tested that is measured by the autocollimator, which sends the angular data to a computer with MATLAB in operation. This is in charge of the calculation of the damping force value, so the intensity of the LED's electromagnetic radiation, and the control of the servo right position moving the pivot mirror. The light coming from the high-power source is directed by the pivot mirror to the fixed mirrors and then to the mirror on the arm. At the end a new displacement is generated by the combination of thruster and damping force on the arm closing the loop.

In the next table are reported the general elements of the thrust stand, particularly the measurement system and damping system, in the same order as reported before.

Elements	Sub-Elements	Description
Autocollimator	-	Information about the angular displacement of the pendulum's arm.
High Powered Light Source	LEDs	Generation of radiant electromagnetic power, controlled by Arduino.
	Optical fibers	Transfers the light from the individual chip LED to the collimator.
	Collimator	Collimate the light coming from the LEDs in a single beam.
Mirrors	Cooling system	Needed to cool the LED and to make it work at a specific junction temperature.
	Pivot Mirror	Direct the light beam in the opposite direction of the moving pendulum.
Computer	Servomotor	Needed to move the pivot mirror to the correct angular configuration.
	Standard Computer	Enough power to run MATLAB and acquired data from autocollimator.
	Arduino (or similar board)	Control the power of the LED and the rotation of the servomotor.

Table 9: General elements of the thrust stand.

## 4.2 LEDs of the Damping System

In this sub-chapter different types of LEDs and some high-power light source designs have been analyzed. As explained in the subchapter before the first research was on LEDs with low wavelengths and high efficiency, as initial idea a system without the optical fibers and the collimator was considered. That because ones of the goals of the project are the cheapness and the simplicity.

### 4.2.1 Common LEDs

The LEDs research starts with an analysis of common and cheap diode, that can be find on ordinary web shops, as eBay or Amazon, in the thesis work from this point on this type is call C-LEDs (Common LEDs). This type is usually made in stock of 0.25 W up to 100 W and just basics data are reported by the seller as Voltage, Current and Luminous flux.

From Chapter 3.3 the maximal radiant power to damp the system was calculated, it was 60.61 W. No information about the efficiency of these diodes was found so it was made an initial approximation estimating an efficiency at 40%, so 151.51 W of needed radiated power.

The initial ideas were to use 1 LEDs of 150W, or 1 of 50 W and 1 of 100 W but considering the difficulty to drive a 100W diode it was chosen to build a modular configuration. This involves the use of LEDs maximum of 50 W, as example there were reported the data of a C-LED found on eBay, this is a Blue LEDs with specific colour: Royal Blue, Wavelength  $\lambda$ (nm): 440-450, [46].

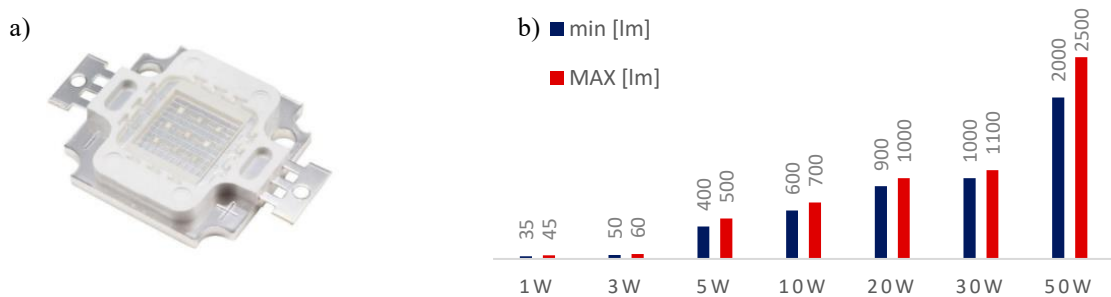


Figure 38: C-LED Royal Blue  $\lambda$ : 440-450nm: a) Real image; b) Relation Electric and Radiated power [46].

The absence of information on the radiated power and the spectrum of the light emitted is common for C-LEDs, this makes it difficult to use them for a project because the real power could only be measured by testing real components. As mentioned before there is no presence of a collimating system based on optical fibers, so it was thought to use a lens to collimate the light emitted by the LEDs and there were evaluated some configuration to minimize the space between each diode and to size the hypothetical lens diameter, as show in the following picture.

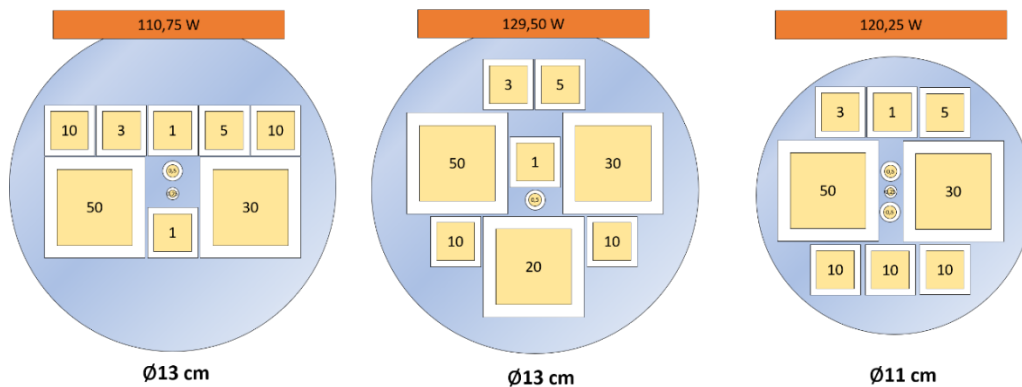


Figure 39: First concept of high emitting light source: 3 configurations.

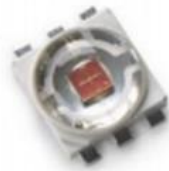
Advantage of this modular configuration was the possibility to not modulate the power of each LEDs but only switch ON the diodes needed to reach the radiation power, each LED needed an individual driver to be powered.

Disadvantages were the big size of the LEDs and most important the difficulty to collimate the light coming from source with different viewing angle and sizes, distributed in a no proportional way.

### 4.2.2 Specialized LEDs

The next idea was to use small LEDs with the same power consumption to ensure an easily control and a right light collimation. The research focused on LEDs with better characteristics and more expensive than before, found on more specialized sites as Mouser Electronics and Digi-Key electronics, in the thesis work from this point on this type is call S-LEDs (Specialized LEDs).

The first one presented here is the: S-LED ASMT-JL31-NRS01, Colour: Royal Blue, Wavelength  $\lambda$ (nm): 440-460, the choice of this component was due to the low wavelength that guarantees an elevated radiation power and an efficiency declared by the manufacturer close to 40%: This is a small 3 W LED with a maximum radiation of 1020 mW at the room temperature of 25°C [47].



Fix $I_F = 700$ mA ( $T=25^\circ\text{C}$ )	
Radiant Flux ( $\phi_e$ )	1020 mW
Voltage ( $V_F$ )	3.6 V

Figure 40: S-LED ASMT-JL31-NRS01, Colour: Royal Blue, Wavelength  $\lambda$ (nm): 440-460.

In Figure 41 are reported the characteristics of the diode, in Figure 41 a) a graph of the relative luminous flux depending on the current and in Figure 41 b) an ideal LEDs matrix configuration 8 x 8. The small dimensions of the matrix permitted to size a smaller lens than before, but the elevated viewing angle of 165° made impossible the collimation by lens. This was an error happened due to a primary research of high-power LEDs with high efficiency, the difficulty to find information about the radiated power had overwhelmed the need for diode with small view angle, however these LEDs are good candidates not to be underestimated for a future system with optical collimated system.

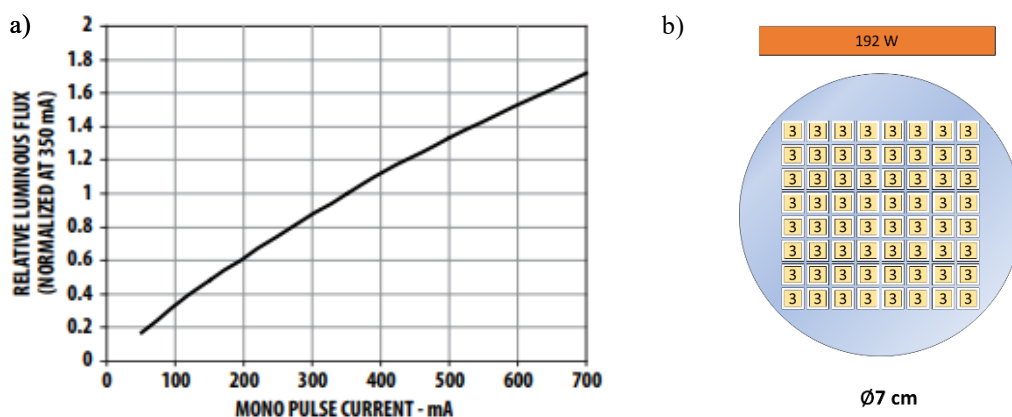


Figure 41: S-LED ASMT-JL31-NRS01: a) Typical Characteristics [48]; b) Configuration concept.

Advantages of these diodes are the compact size: 5 mm x 4 mm, the high-performance energy efficiency. Also, the price of a singular chip on Mouser is 3.28 € [47], for the matrix system 64 diodes would be needed so 210 €.

The most important disadvantage is that can only be used with an optical fibers collimations. The value 192W reported in Figure 41 b) referred to the total electric power required to use all the diodes in the matrix, for an efficiency of 40%, the total value of radiated power is 76.8 W, bigger than the one required due to the possible presence of unpleasant effects.

After it was evaluated the possibility to use LEDs with wavelengths close to the UV (values close to 395nm), because it was easier to have information about the radiant power emitted, reported in the datasheet, and for the high efficiency of this diodes.

The second diode presented here is the UV-LED LuxiGen™ LZ1-00UAP5, Colour: Violet, Wavelength  $\lambda$ (nm): 395, the choice of this component was due to the elevated radiation power and an efficiency declared by the manufacturer close to 50%: This is a small 3.4 W LED that at maximum power 4.1 W generates a radiation power of 2.0 W at the room temperature of 25°C [49].



	Fix $I_F = 1000$ mA ( $T=25^\circ\text{C}$ )	
	Minimum	Maximum
Radiant Flux ( $\phi_e$ )	1.6 W	2.0 W
Voltage ( $V_F$ )	3.1 V	4.1 V

Figure 42: UV-LED LZ1-00UAP5: Colour: Violet; Wavelength  $\lambda$ (nm): 395.

In Figure 43 are reported the characteristics of the diode, in Figure 43 a) a graph of the typical current characteristics and in Figure 43 b) the relative luminous flux depending on the current. The typical working point is at 3.4 W of electrical power circa 1.7 W of radiation power are emitted, but as explained before could reach 2.0 W.

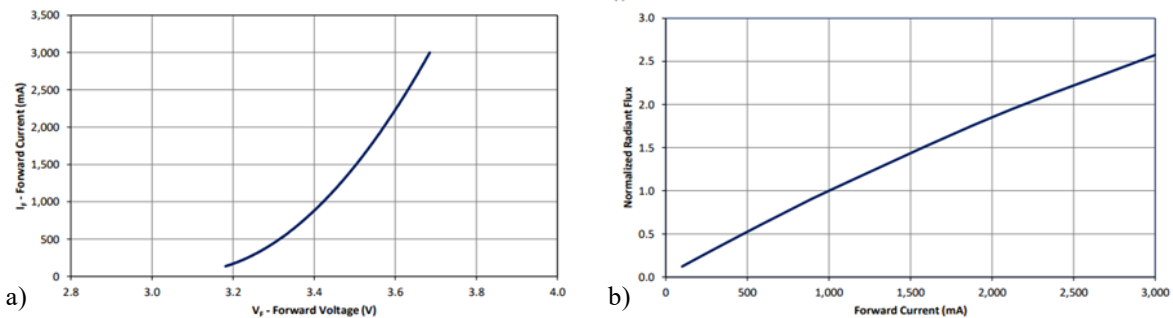


Figure 43: UV-LED LZ1-00UAP5: a) Typical forward current characteristics; b) Typical normalized radiant flux over current [49].

Advantages of these diodes are the compact size: 4.4mm x 4.4mm, close to the one before, and the possibility to emit 4.1W flux output from 1 mm<sup>2</sup> chip at 3000 mA. Also, equally relevant is the view angle of 85°, much smaller value than the one before, which increases the ease collimating.

On the other side one disadvantage is the expensive price, on Mouser is 12.86 € for one [50], for a matrix system like the one presented before 36 would be needed, so 462.92 €. To calculate the number of diodes in the matrix it was used the same consideration explained for the previous LED.

The low view angle of this diode permits its use for lens or optical fiber collimating system, in any case the second one is better because guarantees less power losses, and it is more expensive than the first one. After this research the diode UV-LED LuxiGen™ LZ1-00UAP5 was considered as the best option that could be used in the system, for the elevated radiant power and efficiency.

### 4.3 Cost Analysis

To have a complete view of the project it was necessary a primary evaluation of the thrust balance cost, the price of a possible computer to run MATLAB was not considered because a standard Laboratory one could be use. For the Arduino in charge of LEDs power control was estimated a cost of 20 €, the cooling system price was estimated 100 €, looking at efficient CPU cooling systems having the same power dissipation of the damping system, and the price of mirrors and servomotor was estimated 20 €.

In Figure 44 are reported the initial total cost evaluations, the chosen diodes of the damping system are the UV-LEDs LuxiGen™ LZ1-00UAP5, also are reported the maximum price of 11 702 € calculated considering the more expensive autocollimator TriAngle TA 100-38 and the minimum of 9402 €, choosing the autocollimator ELCOMAT direct 140/40.

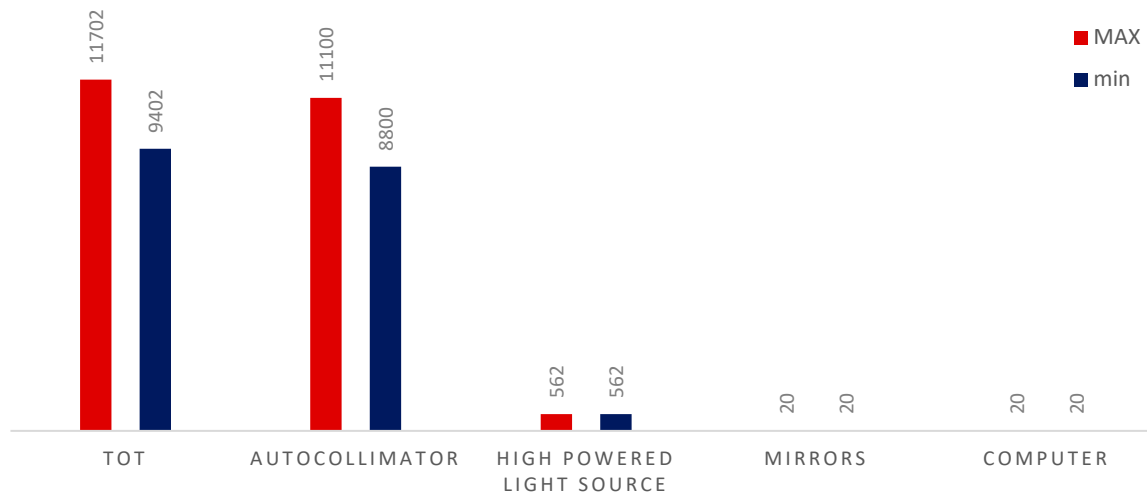


Figure 44: Evaluation cost of the project

From the figure above it's obvious that the autocollimator represent the component with the most elevated cost, this is justified by the high sensibility required by the measurement system, between the two presented the best solution could be TriAngle TA 100-38 for its predisposition to work in a vacuum chamber, quality absent in the other one.

### 4.4 System Changes

After the primary evaluation cost analysis, a meeting was made with the responsible professor and the following decisions were taken:

It was discussed the elevated autocollimator price and it was established that a new measuring system needed to be design. The expense would have been expensive considering the first stage of the project and the not predictable working result of the electromagnetic thrust radiation made by LEDs. This new system should work on the deflection of a laser to reduce the cost, if the experiment work successfully, the possibility to buy an autocollimator will be evaluated.

Then it was analysed the dangerousness of the UV-LEDs, it would be necessary to work with this technology in a prepared environment wearing protective eyewear, so they were not suggested for the project. It was decided that the research should be focus on LED emitting White-cool light, with high colour temperature, so high presence of blue radiations, and elevated value of luminous flux, from this point on this type is call W-LED (White LED).

It was approved the possibility to use a water-cooling system inside the vacuum chamber to cool the damping system source, also it was decided to evaluate the possibility of using a Peltier Cell, while for the cooling system of the thrusters on the swing arm the water one was not recommend. Due to the difficulty design and the unwanted vibrations generated by the water flow, it was decided to design a sized cooling block.

The Table 10 show a summary of the system changes decided after the meeting and that are analysed in Chapters 5:

Sub-Systems	New Options
Measuring System	Laser Deflection
LEDs	W-LEDs
Cooling System	Water Cooling / Peltier Cell

Table 10: Resume of changes after meeting.

## 5 Damping System Design

This chapter is focus on the design of the damping system, here are reported all the consideration made on the project from the first ideas to the final concept. As mentioned at the end of Chapter 4.4, after a meeting with the responsible professor it was decided to use W-LED instead of UV-LEDs due to their danger. The first subchapter is on the design of the LED system, some concepts have been testes with an analysis on the real radiant power emitted and the efficacy of the light collimating system. The second on the sizing of the mirror in charge of direct the light; the last one on the design of the water-cooling system.

### 5.1 LED System

The research started from the assumptions made in Chapter 4.2, that is a research focused on the use of W-LEDs with high colour temperature and high radiation power. The supervisor suggested to design a system without optical fibers, simple as possible to minimize the cost, to be easily tested and proving the efficacy of this damping system based on light radiation technology.

First it was suggested to search for the most common W-LEDs and to not use a combination of diodes, as the one presented in Chapter 4.2.1 due to the absence of an optical fibers collimating system. So, it would be preferred to use a single chip able to generate at least 60W of radiating power, considering the low efficacy of this diode that before it was overestimated of 40%, an electrical power between 100W and 150W is needed.

Usually this type of diodes has dimensions 4 x 4 cm and a chip size of 2 x 2 cm, they can reach a luminous power of 9 000-10 000 lm, sometimes 11 000 lm [51]. They need to be cooled because the elevated junction temperature quickly increases lowering down the value of the radiating power, typical behaviour of the emitting diodes. The information about the radiant power presented in the datasheets are usually referred to an ambient temperature of 25°C and as made before when there is no information about the value of radiated power it will be consider an efficiency of 40%. The viewing angle should be low as possible, online they can be found chips with angle between 0° and 180°, and the idea was to collimate this using lensed.

In Figure 45 are reported the common characteristics of a 100 W W-LED, it is possible to observe that that view angle is elevated, because these diodes are usually used to illuminate rooms, and that they have also an elevated luminous flux.



Characteristics (T=25°C)	
Luminous Flux ( $\phi_v$ )	10000 lm
Power ( $P_{in}$ )	100 W
Efficiency	40% [37]
Viewing angle	140°

Figure 45: Typical 100W W-LED characteristics.

The idea was to use this type of diodes in the damping system but due the elevated viewing angle something was needed to decrease this value, in order to hit the mirror on one extreme of the pendulum's arm in a smaller area.

### 5.1.1 First solution

The first test was evaluating some common cheap solutions to focus the light using lens and it was found online a simple system that could reduce the viewing angle. This was composed by two elements: one small conical mirror, used as a reflector collimator, which task was to collimated the light emitted for viewing angles close to  $140^\circ$ , in order to not lose this power; a glass lens with light transmittance of 98%, and a view angle of  $60^\circ$  [52].

In Figure 46 are reported the data of the components of this system that were used as inspiration for later designs.



Figure 46: a) Reflector collimator; b) Lens; Lens characteristics [52].

Then it was considered that to prevent light reflection in the vacuum chamber, produced by the light coming from the LED and the one reflected by the mirrors, a tunnel way for the light pass was needed. To prevent the born of new heating source PVC white tubes were chosen to cover the light way starting from the lens and ending close to the extreme of the pendulum's arm. In following figure is shown how this system should have worked, in Figure 47 a) there are the LED with the view angle decreasing system, and in Figure 47 b) the complete system with mirrors inside a tubing tunnel.

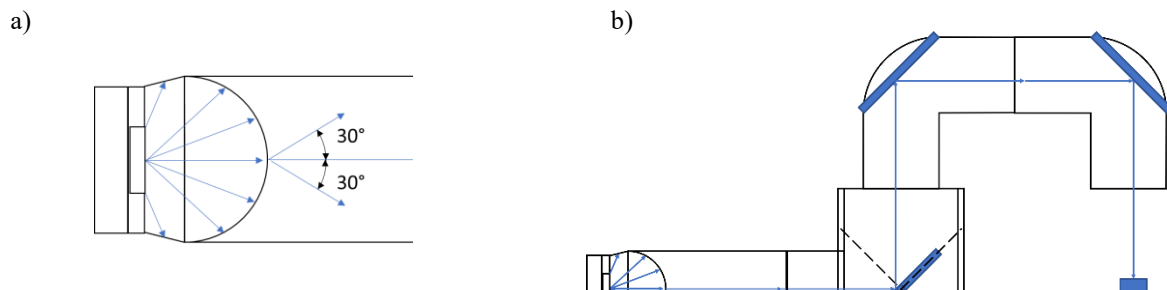


Figure 47: a) LED, reflector, lens and starting of the tubing; b) Complete system with mirrors in blue.

This system would never work as mentioned because the viewing angle after the lens was too high to define a long way until it hits the pendulum's arm, the final size of the beam would have been too big, and a lot of radiant power would be lost. Anyway, this first try was used to estimate the mirrors size, the light way length from the LED to the arm and the complete size of the system. From this system it was observed that a component was needed to collimate the light for the upper viewing angle, as the conical mirror, and that a sized lens was needed to collimate the lower ones.

### 5.1.2 Second solution

The second idea was to use a parabolic mirror for the first purpose and a convergent lens for the second one (exposed before), then a big divergent lens to focus the light coming from the components before. In this case the PVC tubing system wasn't chosen to be used, if necessary, at the end of the project it would have been design.

The parabolic mirror would have changed the direction of the light collimating it, as shown in Figure 48, and increased the quantity of light that in the preview configuration would have been wasted. The first parabolic reflector tested was found online, it was a cheap solution and it was decided to use its characteristics for a first design [53].

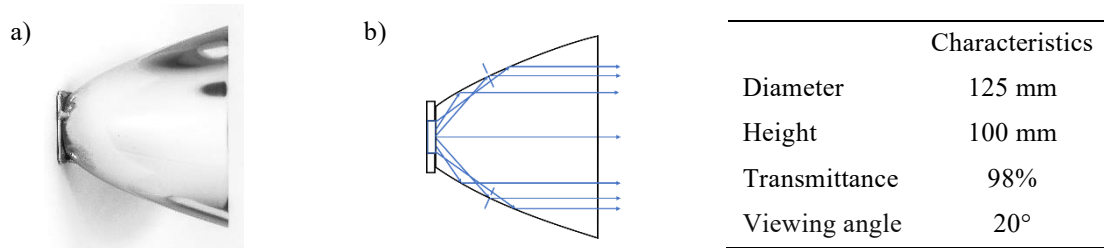


Figure 48: a) Parabolic mirror; b) How it works; Characteristics.

Not all the light emitted by the LED would have been collimated by the reflector, so an aspheric condenser lens was chosen to collimate the light coming from the incoherent source. The one chosen for the project was the: ACL5040U Aspheric Condenser Lens [54], diameter: Ø50 mm, focus length: 40 mm, Uncoated, found on Thorlabs online store.

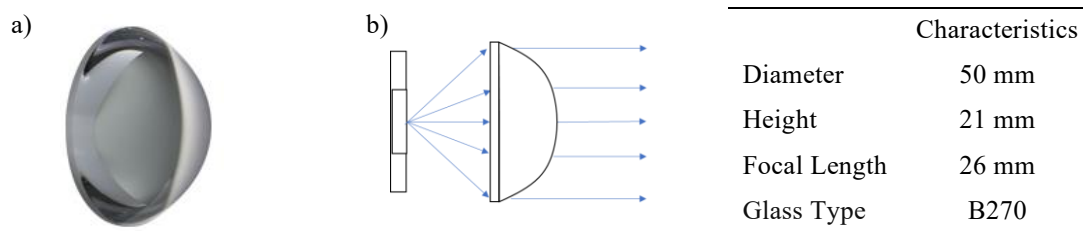


Figure 49:a) ACL5040U Aspheric Condenser Lens; b) How it works; Characteristics.

With this configuration at the end of the parabolic mirror at least a diameter of 100 mm of collected light could be generated, then a Fresnel Lens could be used to focus the light at the needed length. The light coming out from this lens need circa 350 mm to complete the mirrors way and hit the swing arm, so a Fresnel lens with diameter Ø110 mm and focus length: 350 mm was found [55].

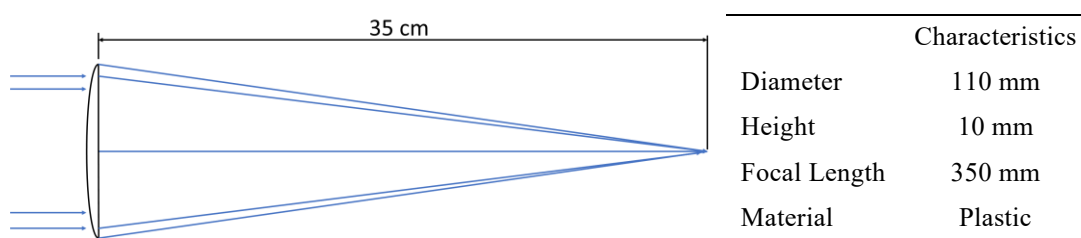


Figure 50: Chosen Fresnel lens characteristics.

To support the aspheric condenser lens inside the parabolic mirror a component was design, this support could be printed in 3D and its information are shown in Figure 51 a), while Figure 51 b) shows the complete system and how it works.

To simulate the system the program Optgeo was used, the first results showed that the system wasn't working well and only a few quantities of light was really focused to the strike point, as shown in Figure 52. Where the red lines are the light rays emitted and the green element represents the extreme of the arm at 350 mm from the Fresnel lens (light distance, not the realistic one between the two elements). The size of the strike a was chosen with the same dimensions of the chip LED.

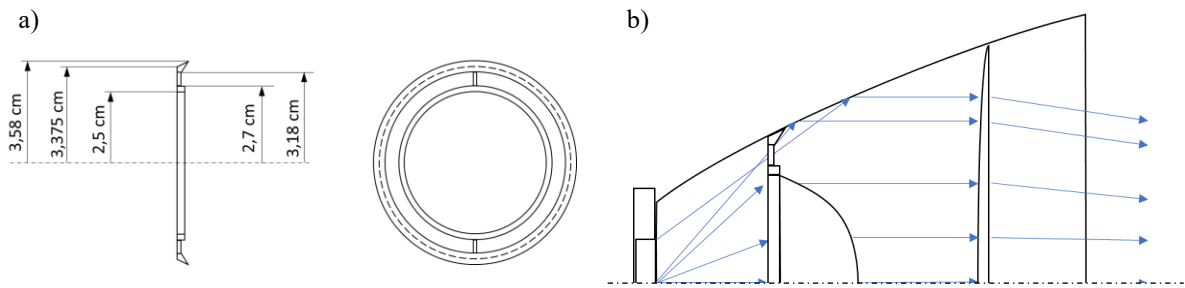


Figure 51: a) Component design to support the aspheric lens; b) Complete system.

Considering that the real LED is not a point source but a composition of more punctual sources, it was simulated as a composition of 3 punctual sources having all the same viewing angle, one positioned in the centre and two positioned at the extreme of the LED length.

The reasons why this system didn't work was the difficulty of the Fresnel lens to focus the light coming from a no punctual source. Also, the use of more elements to direct the light complicated the system making it more sensible to errors. The system was subject to Spherical Aberration.

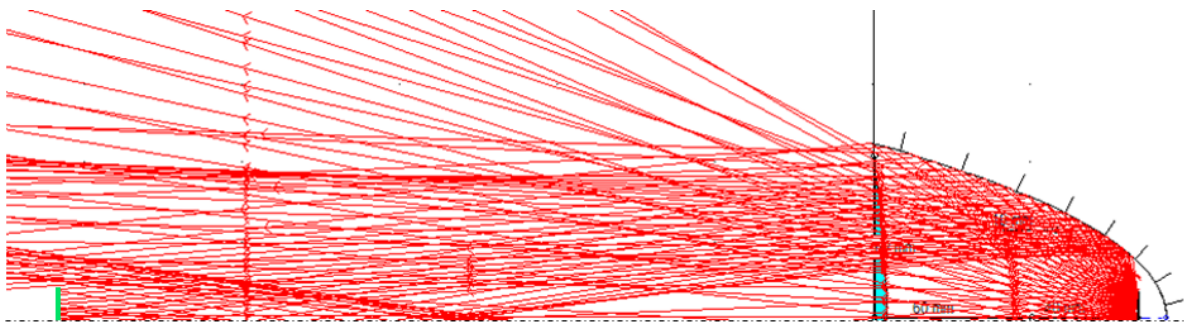
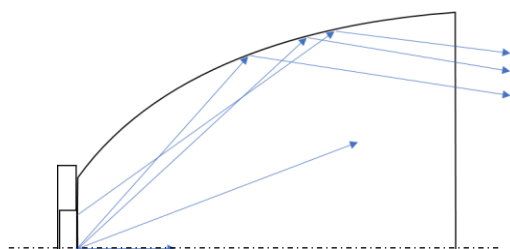


Figure 52: Optgeo simulation of the second solution, the element in green is the strike point.

### 5.1.3 Third solution

After previous simulations it was decided to no use more the Fresnel lens, to change the parabolic mirror in an elliptic reflector, so to focus the light immediately without having more elements directing the light, as explained in Chapter 1.2.2. Also, the possibility to collimate the light not focused by the mirror using an aspheric lens has been abandoned because didn't work properly.

To design the elliptic mirror first was decided to use the same dimension of the parabolic ones so:



	Characteristics
Diameter	125 mm
Height	100 mm
Focal Length	350 mm
Transmittance	98%

Figure 53: Chosen Elliptic reflector characteristics.

First results showed that the light was more focused than before but as previously mentioned the size of the LED was decreasing the possibility to be focused well. Also, a lot of light radiation of the rays not focused by the reflector was lost. With the program Optgeo was difficult to define the quantity of power lost so a MATLAB programme was built to calculate it.

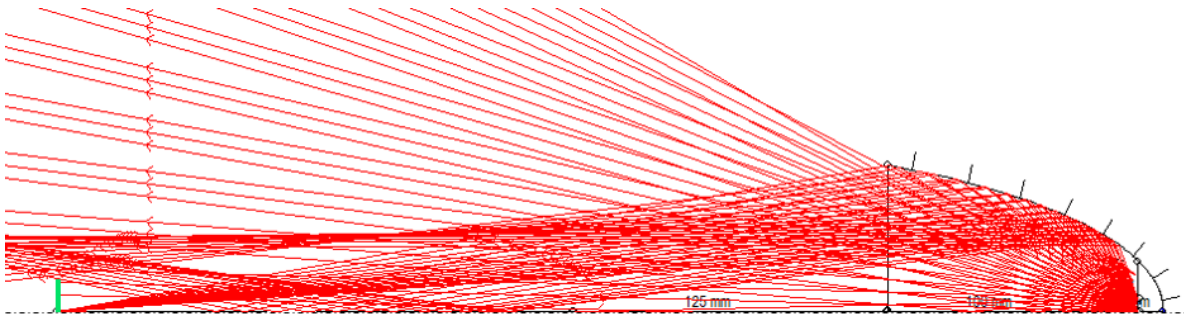


Figure 54: Optgeo simulation of the third solution, the element in green is the hitting point.

### 5.1.4 Radiant Power Model of LEDs

After simulation with cheap W-LEDs it was decided to build a program to calculate the amount of power emitted by LEDs knowing the luminous power and the spectrum characteristics. To do that it was necessary to define the Luminous Efficiency Function. This function describes the average spectral sensitivity of human visual perception of brightness, ISO 11664-1:2007, and it can be approximated by the function [56]:

$$V(\lambda) = 1.019 e^{(-285.4 (\lambda/1000 - 0.559)^2)} \quad (Eq. 46)$$

In Figure 55 is reported the graph of the function  $V(\lambda)$  depending on the wavelength.

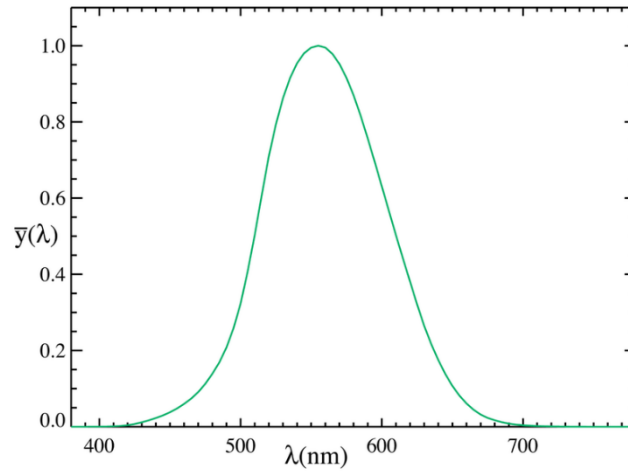


Figure 55: Luminous Efficiency Function,  $V(\lambda)$ .

Knowing the spectrum radiant power of a source  $\phi_{e,\lambda}(\lambda)$ , it is possible to calculate the luminous flux  $\phi_V$  with the following function:

$$\phi_v = 683.002 \text{ lm/W} \int_0^{\infty} V(\lambda) \phi_{e,\lambda}(\lambda) d\lambda \quad (Eq. 47)$$

In order to calculate radiant power could be use the Luminous Efficacy of Radiation (LER) to have data about how well the source produces visible light, unit lm/W:

$$LER = 683.002 \text{ lm/W} \frac{\int_0^{\infty} V(\lambda) \phi_{e,\lambda}(\lambda) d\lambda}{\int_0^{\infty} \phi_{e,\lambda}(\lambda) d\lambda} \quad (Eq. 48)$$

And then finally the total radiant power  $\phi_e$  knowing the luminous power  $\phi_v$ :

$$\phi_e = \frac{\phi_v}{LER} \quad (Eq. 49)$$

The MATLAB script works with the data input of the spectrum radiant power and the luminous power of the LED.

As mentioned before the size of the LED were creating problems in the light focusing so a research was made to find diode of 100 W with characteristics like the ones presented before but with smaller dimensions. Online W-LED with circular chip were found, better for light distribution, and with small diode size having a diameter of 1 cm.

In Figure 56 are reported the data of the YJ-BC-160H-G01 High CRI LED chosen as a candidate for subsequent tests [57].

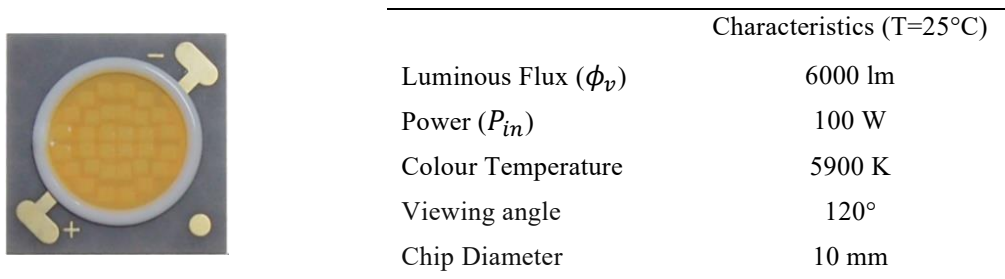


Figure 56: W-LED YJ-BC-160H-G01 characteristics [57].

In the datasheet the data of the typical spectral distribution graphs were presented, so it was possible to calculate the radiant power using the MATLAB program. In Figure 57 are shown: a) the Spectral power distribution of the diode; b) the Photonic spectral luminous efficacy curve, other name for the Luminous Efficiency Function; c) the product of the previous curve.

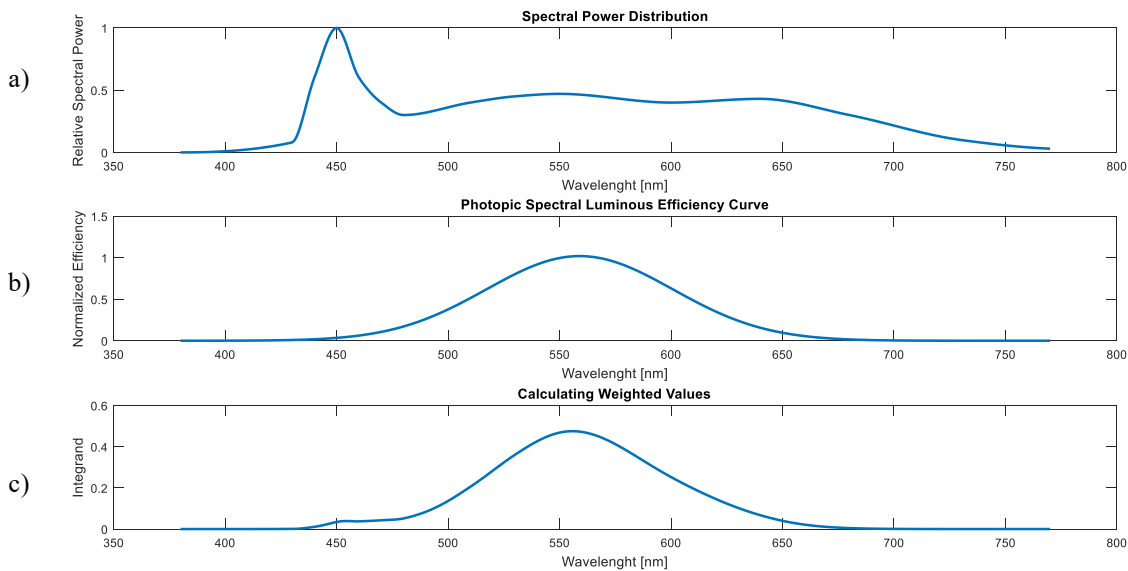


Figure 57: a) Spectral power distribution YJ-BC-160H-G01; b) Luminous efficiency function; c) product between graph a) and b).

The total radiant power  $\phi_e$  of the diode is estimated to be 23.49 W and LEF 255.47 lm/W, the efficiency calculated is of 23.5% so less than expected before but explained by the smaller quantity of luminous flux than before (YJ-BC-160H-G01  $\phi_v=6\ 000$  lm and previous 100 W W-LED  $\phi_v=10\ 000$  lm) .

### 5.1.5 Efficiency Model of Conical Reflectors

Then it was built a MATLAB program to calculate the efficiency of the reflector so to have an evaluation of the final radiation power, at first there were designed 3 types of reflector: the first with the same shape of the one presented before, the last were designed trying to focus as much possible light but in two different ways.

The first one presented in Figure 58 was designed to focus the light coming from the focus to 450 mm of length, the red point in the figure b) is the focus. It has a max diameter of 115 mm and it was estimated a transmittance of 98%. With this configuration not all the light emitted could be reflected by the conical mirror but only the light with an inclination angle from 30° to 60°.

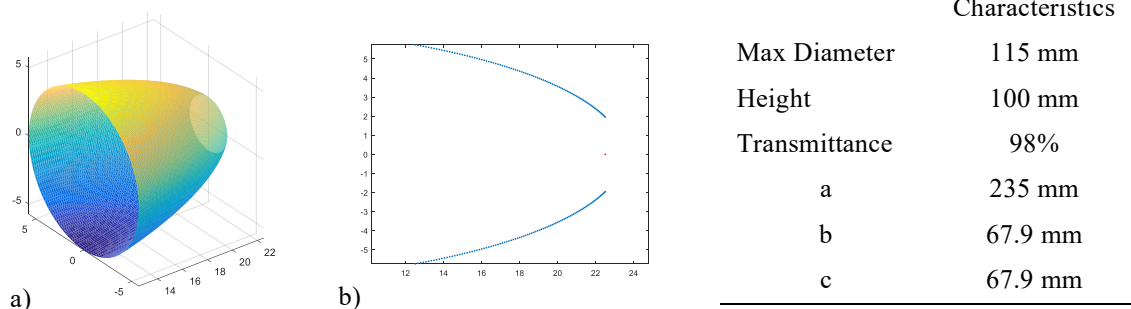


Figure 58: First reflector: a) 3D; b) 2D; Characteristics.

The second reflector presented in Figure 59 was designed trying to focus more quantity of light than before increasing the height up to the next focus, that increases the inclination angle from 14° to 60°, for this configuration they should be use 2 LEDs and 2 reflectors instead of the pivot mirror and the mirrors to direct the light.

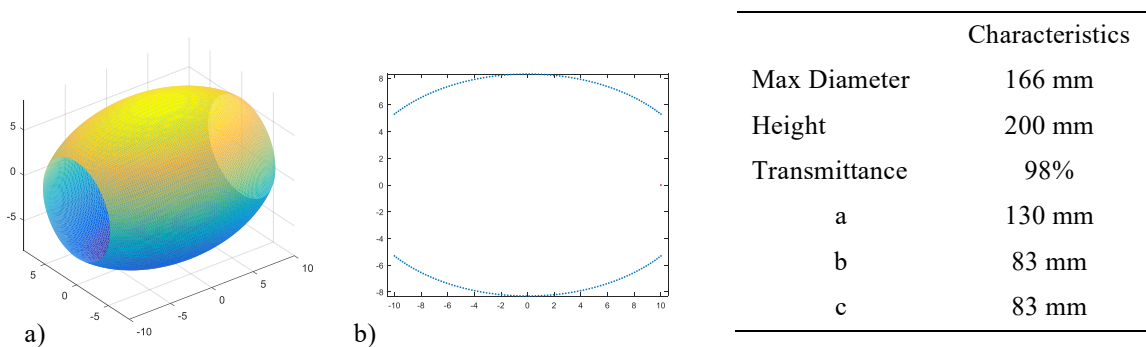
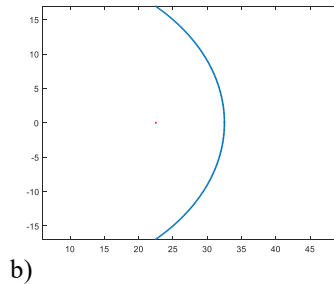
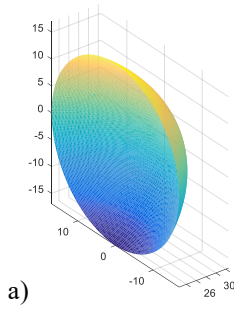


Figure 59: Second reflector: a) 3D; b) 2D; Characteristics.

The third one presented in Figure 60 was designed as before to increase the quantity of light but this time increasing the maximum diameter, the LED is facing in the opposite direction than before, in this way the only light that is not focused is the one coming back to the diode after reflection. As the second configuration 2 LEDs and 2 reflectors should be needed because the area section of the radiation would be elevated, and it could be not possible to size a mirrors light way.



Characteristics	
Max Diameter	338 mm
Height	100 mm
Transmittance	98%
a	320 mm
b	234.5 mm
c	234.5 mm

Figure 60: Third reflector: a) 3D; b) 2D; Characteristics

Then the program evaluates the typical LED spatial distribution of Intensity, that can be found on the datasheet of the diode and it was supposed that the volume of this distribution is the total power emitted by the diode.

$$\phi_{e,\theta_1,\theta_2} = \phi_e \frac{2\pi \int_{\theta_1}^{\theta_2} I(\theta)\theta d\theta}{2\pi \int_{\theta_{min}}^{\theta_{MAX}} I(\theta)\theta d\theta} \quad (Eq. 50)$$

Where  $I(\theta)$  is the Intensity depending on the angle of view  $\theta$ , and all the theta limits are calculated by the program depending on the chosen reflector size, the volume is calculated considering the rotation of the function  $I(\theta)$  around the axis y.

This value compared with the total radiant power emitted by the LED also give an information about the efficiency of the reflector:

$$E_{Ref} = \frac{\phi_{e,\theta_1,\theta_2}}{\phi_e} \quad (Eq. 51)$$

Then was made a consideration on the hitting point at the extreme of pendulum's arm, this need to be a mirror, which ideal size should be the same of the LED, so that the final reflected radiation can generate a pressure perpendicular to the mirror plane. This is the same working principle of the solar sails [58], the value of the generated pressure depends on the inclination of the hitting light rays following the law reported in Eq. 52 as shown in Figure 61.

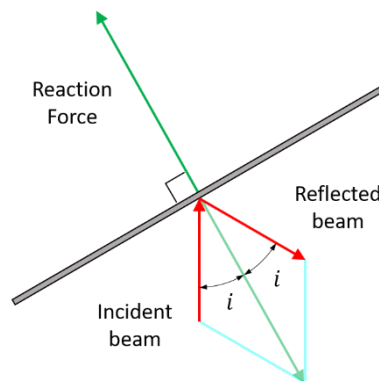


Figure 61: The reflection of the radiation flux generates a force perpendicular to the mirror.

$$F = F_0 \cos^2(i) \quad (Eq. 52)$$

$F_0$  is the force generated by LED radiation after the reflector and  $i$  is the inclination of the radiation respect the normal of the mirror surface, if it is considered the mirror as a perfect reflection plane the law can be rewrote as:

$$F = 2 F_0 \cos^2 (i) \quad (Eq. 53)$$

So, it should be important to know  $i$  in order to define a good value of final efficiency of the system. In the program it was created a relation between the inclination and the view angle of the LED and for the dependency of the intensity on the inclination:

$$E_{Ref\_incl} = \frac{2\pi \int_{\theta_2}^{\theta_1} I(\theta)\theta \cos^2 (i)d\theta}{2\pi \int_{\theta_{min}}^{\theta_{MAX}} I(\theta)\theta d\theta} \quad (Eq. 54)$$

Then as explained before if the arm-mirror is perfectly reflecting, the ending efficiency of the reflector could be rewritten as:

$$E_{Ref\_fin} = 2 E_{Ref\_incl} \quad (Eq. 55)$$

After the MATLAB script was completed, the 3 reflectors designed before were tested and in Table 11 them efficiency are reported:

Reflector N°	1	2	3
Efficiency of the reflector ( $E_{Ref}$ )	68.18 %	91.53 %	99.94 %
Efficiency of the reflector with inclination effects ( $E_{Ref\_incl}$ )	67.76 %	63.93 %	99.66 %
Efficiency of the reflector with perfect reflecting mirror ( $E_{Ref\_fin}$ )	135.56 %	127.86 %	199.32 %
Final W-LED YJ-BC-160H-G01 radiation power ( $\phi_{e\_fin}$ )	31.84 W	30.03 W	46.82 W

Table 11: Data of the MATLAB simulation for different types of reflectors.

In Figure 62 there is reported the typical spatial distribution of Intensity depending on the angle of view of the W-LED YJ-BC-160H-G01 [57], a) in 3D and b) in 2D. Then in Figure 63 in next page it is reported how this distribution vary with the reflectors, in the first 2 column the first effect of reflector on the distribution of intensity is shown, as before in 3D and 2D. In the third column there are reported in blue the effects of inclination on the Intensity and in red the same one with the limitation of the reflector.

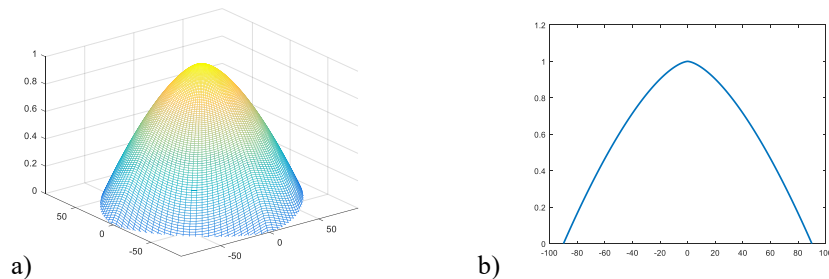


Figure 62: LED Intensity distribution: a) 3D; b) 2D

From the Table 11 and the Figure 63 in the next page, it can be seen that the best reflector would be the third one but considering its big dimension, the needed space to be build and a needed identical

system on the other side of the arm, the first one remains the best option. Also, if the effects of the inclination had not been taken in consideration the second reflector would have been the best solution.

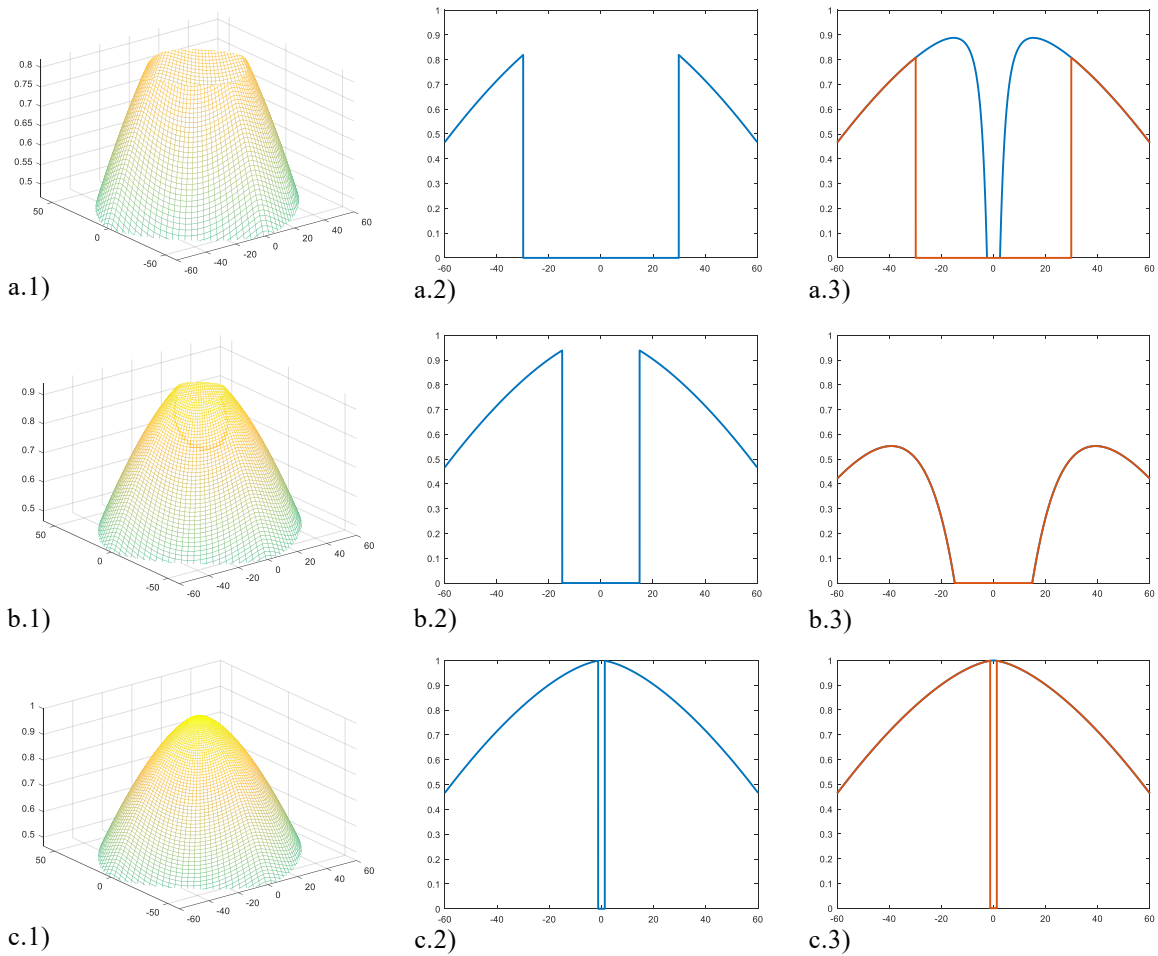


Figure 63: Intensity distribution after reflector: a) 1<sup>th</sup>; b) 2<sup>th</sup>; c) 3<sup>th</sup> : 1) 3D; 2) 2D; 3) with inclination effect.

After the results of the simulations it was considered to continue using reflector as the type of the first one presented before, for the small size and the good efficiency, then in case this solution would not be work well the third solution could be taken in consideration.

### 5.1.5 Fourth solution

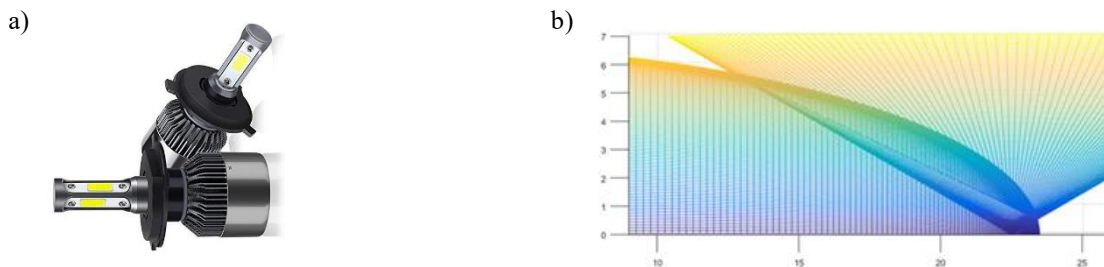


Figure 64: a) Typical car headlights LEDs; b) Light distribution inside reflector.

To improve the system, it was decided to find LEDs with better radiant power and with small chip size in order to have a better light focalization. The initial idea was to use the car headlights LEDs and from that build a better system. In Figure 64 a) a typical LED configuration used in a car is shown

[59], from that was chosen to change the orientation of the LED inside the reflector Figure 64 b). In this way the quantity of light focused would be bigger, the spherical aberration effect would be smaller, also smaller reflector and mirrors would be needed.

First it was designed a system with the W-LED presented before but instead of using just one, 3 of this type were disposed in the way reported in Figure 65, each diode has an angular view of  $120^\circ$  and a chip diameter of 10 mm:

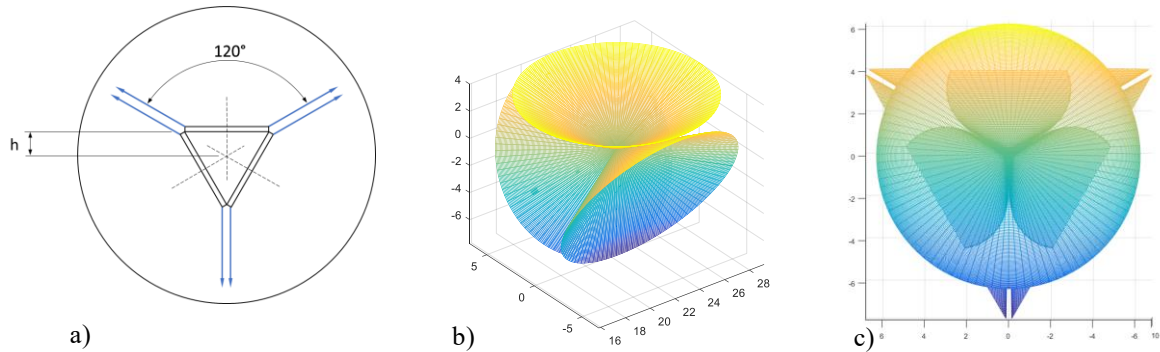


Figure 65: First concept 3 LEDs of 10 mm diameter: a) Frontal view; b) 3D View; c) LEDs inside reflector.

Due to the big angle of view the value  $h=2.88$  mm reported in the image would be too small to permit the design of an efficient heat exchanger of the cooling system. One solution could be to remove one of them, so increasing the space available and the efficiency of the exchange.

After this also LEDs with smaller view of angle and small power were evaluated, for example it was analysed the W-LED, TX-1818W20FC65-CUVCNG-A01 [60], same size of the previously one. Less luminous power emitted, based on singular chip emitting, so the light can be focused better considering the diode as a point source.

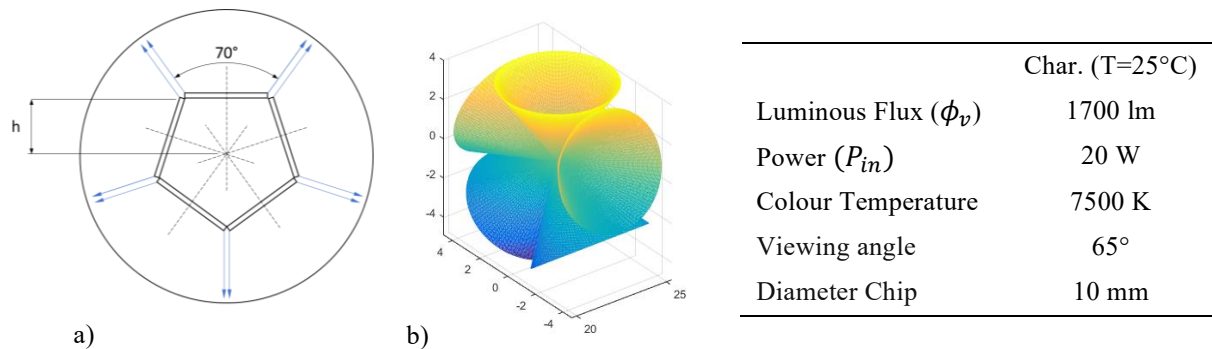


Figure 66: Second concept 5 LEDs of 10 mm diameter: a) Frontal view; b) 3D View; LED Characteristics.

This configuration with 5 diodes was tested as the ones before but the calculation changed cause to the different orientation of the LEDs. First it was analysed the power produced by just one of them and it was considered the same efficiency of the W-LED YJ-BC-160H-G01, so LED efficiency 23.5 %.

Than was evaluated the effect of the reflector (same reflector of before), all the light emitted by the LED is focused by the reflector because there are not angular limitations, so the Intensity graph results the same of Figure 62, and the first effect of the reflector has a value of 100%.

Than as before it was build a relation between the view angle and the reflected angle in order to calculate the inclination effect, the view angle is expressed in this form: all the light reflected in the

left zone of the reflector is considered with a negative view angle while the other side positive, as shown in Figure 67.

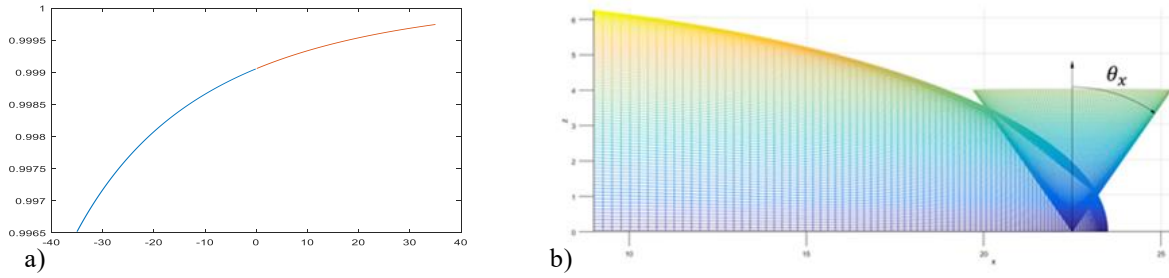


Figure 67: a) Inclination effect depending on view angle; b) Configuration.

The efficiency of the reflector with the inclination effect was calculated as a ratio between the volume of the Intensity with inclination effect and the ones without, the volumes were calculated with a triple integral as reported below:

$$E_{Ref\_incl} = \frac{\int_{\theta_x min}^{\theta_x max} \left( \int_{\theta_y min(\theta_x)}^{\theta_y max(\theta_x)} \left( \int_{I min(\theta_x, \theta_y)}^{I max(\theta_x, \theta_y)} \cos^2 i(\theta_x) dI \right) d\theta_y \right) d\theta_x}{\int_{\theta_x min}^{\theta_x max} \left( \int_{\theta_y min(\theta_x)}^{\theta_y max(\theta_x)} \left( \int_{I min(\theta_x, \theta_y)}^{I max(\theta_x, \theta_y)} dI \right) d\theta_y \right) d\theta_x} \quad (Eq. 56)$$

As before in presence of perfect reflection  $E_{Ref\_tot}$  became the double of  $E_{Ref\_incl}$ , for an individual chip. If in the system are used 5 LEDs disposed as in the Figure 45 a), the total power radiated by the system is 5 times the power of one.

Efficiency of the reflector ( $E_{Ref}$ )	100 %
Efficiency of the reflector with inclination effects ( $E_{Ref\_incl}$ )	99.89 %
Efficiency of the reflector with perfect reflecting mirror ( $E_{Ref\_fin}$ )	199.78 %
Final W-LED TX-1818W20FC65 radiation power ( $\phi_{e\_fin}$ )	9.19 W
System 5 W-LED TX-1818W20FC65 ( $\phi_{e\_fin}$ )	45.95 W

Table 12: Data of the Fourth solution MATLAB simulation.

This system should be better than the one simulated before because the light can be all focus by the reflector, the inclination effect is least, and it is easier to control the radiated output.

The final total radiated power is 45.95 W, 1.44 times bigger than before with the same power consumption, in Figure 68 is reported also a simulation in Optgeo.

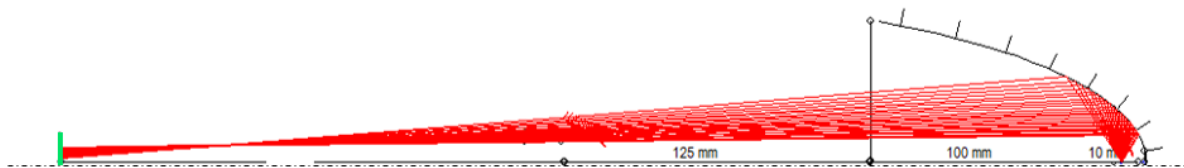


Figure 68: Optgeo simulation of the Fourth solution, the element in green is the hitting point at 350 mm from the end of the reflector, or rather 450 mm from the focus.

Then it was also made an analysis on the radiant area hitting the reflector, from Figure 69 it is possible to see that most of the radiated power is located on the right side of the reflector. So, the final power hitting the mirror at the extreme of the swing arm should have the same shape and distribution as the one in Figure 69 b).

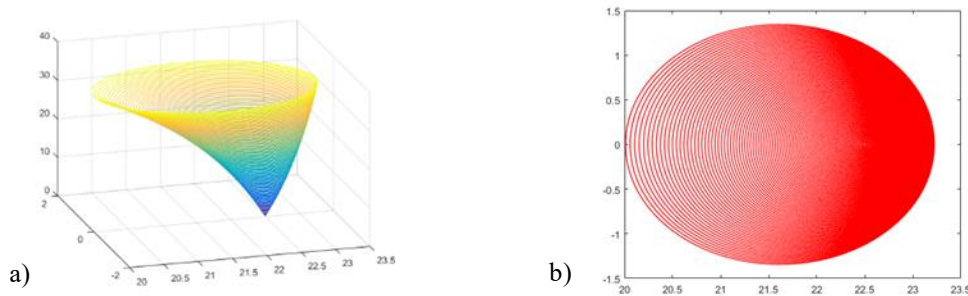


Figure 69: a) Hitting area depending on view angle; b) Distribution of radiated power emitted.

The system presented before called fourth solution was chosen to be used in this project, anyway the MATLAB script could be used to test other different configurations and LEDs.

## 5.2 Mirrors System

Once defined the LEDs and the focusing system, it was time to size the mirrors needed to direct the light from the reflector to the arm-mirror on the swing arm. To do that it was created in Optgeo the reflector with all the 5 LEDs, and then the mirrors have been designed. It was decided to use this program to easily see the light reflections.

The mirrors were disposed in order to minimize the size of the system and depending on the size of the reflector. A smaller reflector could be used, but the one chosen could be used for different configuration in case the one presented before should not work properly.

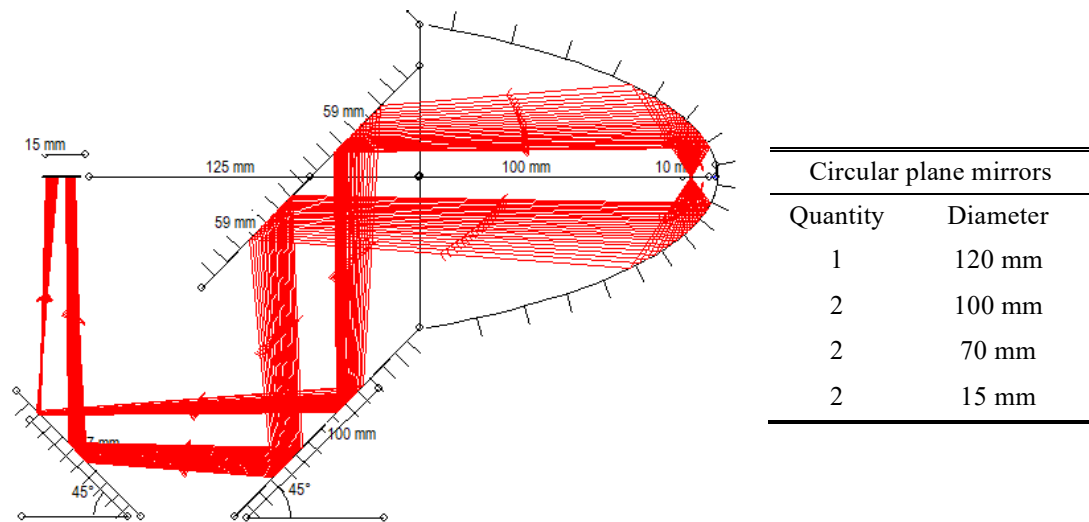


Figure 70: Complete system with mirrors; Table with quantity and sizes of mirrors.

In Figure 70 is reported the complete system, plane circular mirrors are needed in these quantities and sizes: 1 pivot with diameter of 120 mm; 2 fixed of 100 mm; 2 fixed of 70 mm; 2 fixed on the extreme of pendulum's arm in opposite directions at least of 15 mm. The complete system has a size of 260 x 270 x 120 mm.

The rotation of pivot mirror could be controlled by an Arduino using a servomotor. So, a servomotor was chosen based on the elevated stall torque, on the possible angular rotation between  $0^\circ$  and  $180^\circ$  and the operating speed. The mirror rotation axis will be the same of the servo so to minimize the power needed to rotate it.

For the project the mirror should rotate  $90^\circ$ , as showing in Figure 71 b), considering an operating speed of  $0.15 \text{ sec}/60^\circ$  with no load, the mirror should complete  $90^\circ$  in  $\approx 0.4 \text{ sec}$  ( for a load effect of  $+70\%$ ).

The servomotor will start from a zero position with the mirror's face parallel to the reflector open face, in this position no light is directed to the arm. After the first half period of the pendulum, when all the swing arm data is calculated by the program of Chapter 3, then it rotates the mirror every half period of the pendulum, the first rotation is of  $45^\circ$  and the others of  $90^\circ$ .

A first Arduino script was written to test the possibility to drive the servo and below there are reported the data of the chosen one SUNFUONDEN 55g [61].

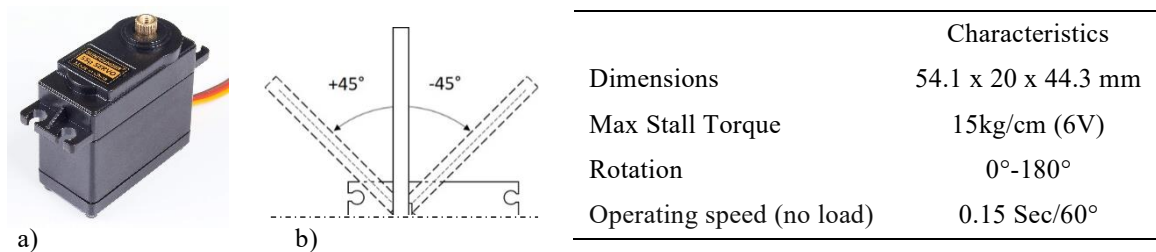


Figure 71: a) Chosen servomotor; b) Maximum limit angles; Characteristics.

### 5.3 Optical Aberrations

In the systems presented in Chapter 5.1 the presence of spherical surfaces implies the birth of a side effects as Spherical aberration and Chromatic aberration, described in Chapter 1.2.2, whose effects could be amplified in the system of Chapter 5.2.

The effect of Spherical aberration causes a wrong reflection of the light rays that strike a spherical surface off-centre by changing the inclination effect. This does not create problems for the Fourth solution because the configuration was studied to minimize the inclination effect, Figure 67.

While the First and Second solutions were affected by Chromatic aberration, failure of lenses to focus all wavelength (colors) to the same point, the Fourth not using lenses is no affected.

### 5.4 Cooling System

In order to have a perfectly working LEDs, so of all the damping system, it was necessary to design a cooling system to keep the temperature close to  $25^\circ\text{C}$ , as explained in Chapter 1.1.2, the one proposed was a water-cooling system, Chapter 4.4.

Not all the total dissipation power of all the LEDs (100 W) is going to be transformed in heat, but it was suggested to design a system able to cool this quantity, this value is close to the one emitted by the ordinary pc CPU [62], so it was decided to start from this type of system.

Usually these systems are composed by a water pump, a heat exchanger radiator, a water tank, a water block and a tubing system to connect all these components.

The ones required for this project should work as showing in Figure 72, the water block, in charge of transfer heat from the diodes to the water, should be the only component working inside the vacuum chamber.

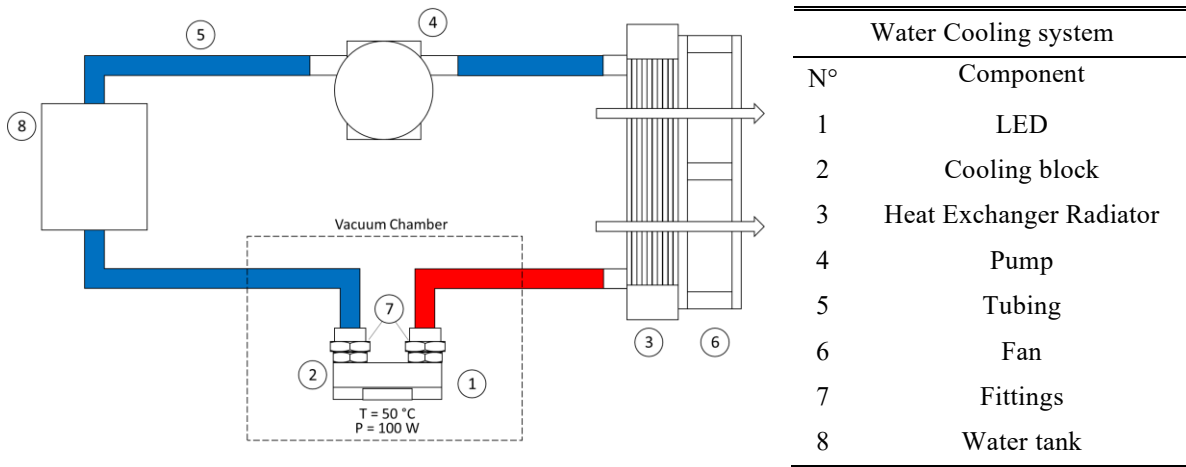


Figure 72: Water cooling system scheme and Components.

The components chosen are usually used in CPU water cooling systems of 100 W dissipation:

- a water pump with: Hydraulic head: 3 m, Volumetric flow rate: 280 l/h, Power: 5 W;
- a heat exchanger radiator: Size: 157 mm x 120 mm x 32 mm, Material: Aluminium;
- a Fan: Size: 120 mm, Airflow: 89.5CFM;
- a water tank of 1 litre, this component could be also bigger if the radiator could not cool enough the water.

In Figure 73 the photos of the chosen components are reported.

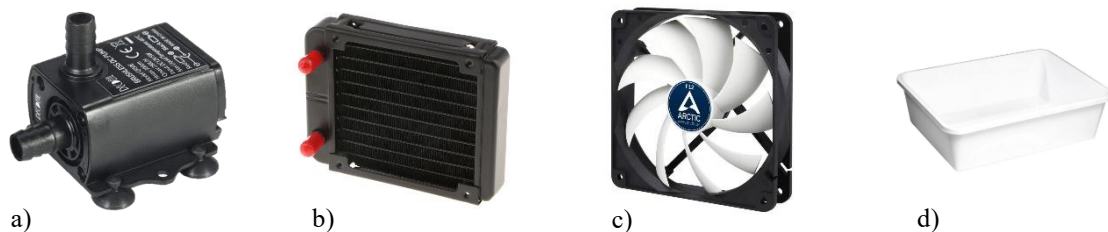


Figure 73: a) Water pump; b) Heat exchanger radiator; c) Fan; d) Tank.

One water block that could be used for the W-LED YJ-BC-160H-G01 is the Asiproper CPU Copper Water Block [63], Figure 74 a), while for the W-LEDs TX-3636W90FC120-NUVENG-A01 a new one is needed to be designed, cause to the orientations of the diodes Figure 66 a).

The idea was to replace the copper base of the Asiproper water block with a pentagonal cylinder, Figure 74 b), and each LED would be attached with thermal paste to one of the five external face of the prism. Inside the cylinder each internal face could have designed fins to allow the heat exchange with all the LEDs. In Figure 74 c) there are also 2 examples of water block fins that could be used, the material of the block should be copper, and the sizes are shown in Figure 74 d) e) and f).

For this designed water block there are 2 configurations that need to be tested, shown in Figure 75 a) and b) next page:

- extreme of the pentagonal cylinder close, water come in and out from the bottom of the block;
- extreme of the pentagonal cylinder open, used as the way out for water coming from the bottom of the block;

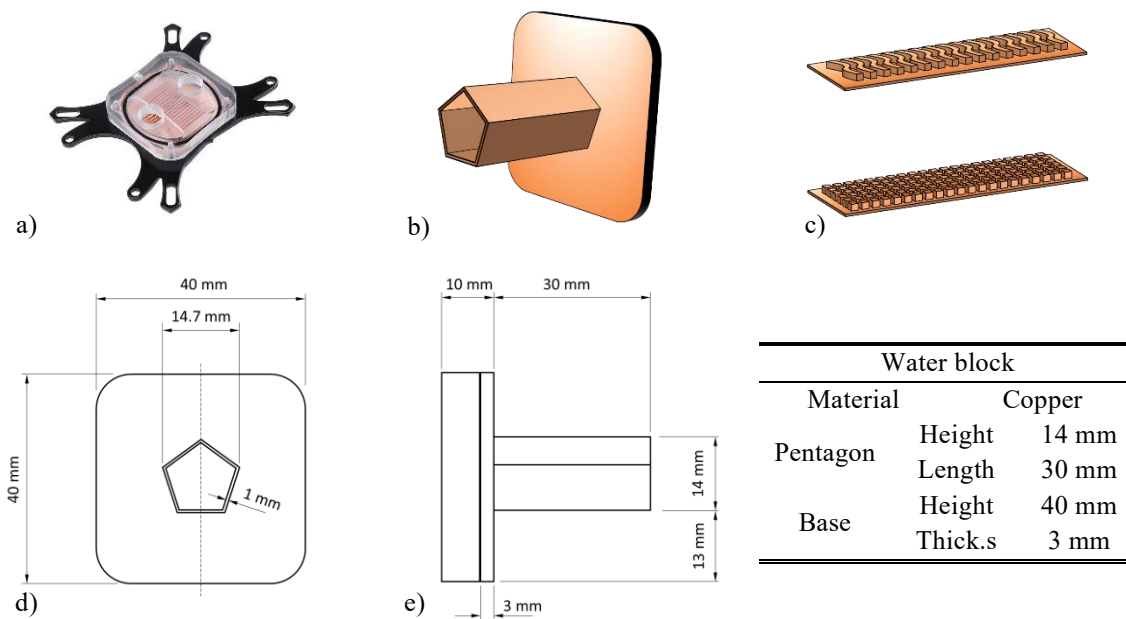


Figure 74: a) Typical Water block [63]; b) Designed Water block; c) Radiator fins; d) Front view; e) Lateral view; Characteristics.

In case this configuration should not work properly cause more cooling power is needed, this component could be replaced with one of same size but full of copper, so no water inside. Also, a Peltier Cell could be placed between this and the water block to increase the heat transfer, Figure 75 c), in that case a more powerful water-cooling system would be needed, to cool the heat radiated by the hot face of the cell.

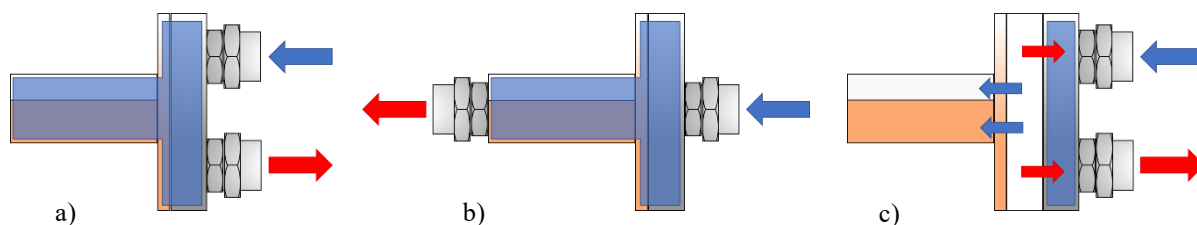


Figure 75: Configurations: a) 1; b) 2; c) 3.

To connect all the previous components a PVC tubing system could be used, with diameter of 10/8mm, and cause to the boundary conditions to prevent water coming out inside the vacuum chamber it is suggested to use fittings connections 1/4 Inch or 11/8 mm.

Then another component necessary for the system already mentioned is the Thermal paste, a thermally conductive compound used as an interface between the water block and the LEDs, so to eliminate the space between the interfaces in order to maximize heat transfer.

As first approximation it could be considered a limited LEDs working temperature of 50°C, the water enters inside the water block at 25°C and goes out at the limit temperature, perfect heat transmission. Then the hot water is transferred inside the tubing to the heat exchange radiator outside the vacuum chamber, here it is cooled by the work of the fan that pull colder air again the fins. After the water enters the 1 litre water tank at ambient temperature and it is forced by the water pump immersed inside to reach the water box in the vacuum chamber closing the loop.

As a critical factor the time to heat all the water inside the circuit without the radiator effect was calculated, so to have information on the ideal working time of the damping system for a  $P_{in}=100$  W source.

$$t = \frac{Q}{P_{in}} = \frac{m c_p \Delta T}{P_{in}} = 17,41 \text{ min} \quad (\text{Eq. 57})$$

This value with the presence of the radiator and the fan should increase, data about cheap radiator are difficult to find, so it was assumed a radiator with 18 FPI, using the datasheet of the radiator Koolance HX-422 Radiator [64].

The heat dissipation of this component plus a fan at 2 LPM is close to 300W for  $\Delta T = 25^\circ\text{C}$ , so the time should be enough for this project also imagining a cheaper radiator with just 50% efficiency of the one that was hypothesized.

The thesis did not treat the specific design of the cooling system, but it was oversized because the system will be adjusted once built, to cool the real power dissipation of the LEDs.

## 6 Swing Arm

In this chapter the pendulum's arm of the thrust stand is designed. The first subchapter is about the cooling system of the thrusters that will be tested on the swing arm and the second on the design of the auxiliary damping system. Then the third on the choice of the pendulum fiber based on the total mass of the components on the arm, and the last one on the calibration method of the thrust stand.

### 6.1 Cooling System

In Chapter 3 the data of the swing arm were described and there were defined the limits of the system, maximum thrust of 500 nN and a minimum of 50 nN. Ideally the LEDs that will be tested will have a high efficiency, more than the 40%, so the maximum radiated power by a LED for lowest efficiency is 378.8W. The remaining 60% of the electrical power should be converted to heat making necessary the use of a cooling system for  $P_{in}=227.3$  W.

On the pendulum's arm a water-cooling system as the ones presented in Chapter 5.4 couldn't be used, due to the vibrations produced by the water movements, so the best idea was to transfer all the heat produced by the LED to the arm, that could work as a heating block. The arm should be designed to resist for a time close to 1 hour, to execute tests on thrusters, and up to a temperature of 50°C. In Figure 76 are reported the swing arm data.

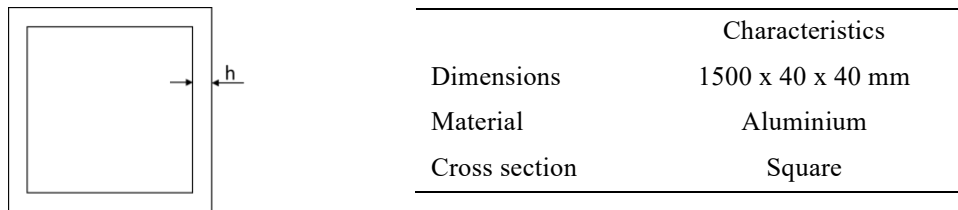


Figure 76: Cross section of the arm; Characteristics.

At the beginning of the project the thickness of the hollow aluminium profile was  $h=5$  mm, so the mass of the arm was  $m_1 = 2.835$  kg, for density of  $2.7$  g/cm<sup>3</sup>. So, it was possible to define the working time to increase the temperature of the profile from 25°C to the limit of 50°C,  $\Delta T_1 = 25^\circ\text{C}$ :

$$t_1 = \frac{Q_1}{P_{in}} = \frac{m_1 C_{p(Al)} \Delta T_1}{P_{in} M_{Al}} = 4,66 \text{ min} \quad (\text{Eq. 58})$$

This time was too low and needed to be improved, so it was decided to work on the factor that could be modified. The thickness of the profile was the first value changed from 10 to 20 mm, this increased the mass of the arm of 171.14%, up to  $m_2 = 4.860$  kg. This value should not be too high because it is limited by the tensile strength of fiber that hold it up. Then the initial temperature of the arm could be taken to 0°C and the limit temperature extended to 65°C, so  $\Delta T_2 = 65^\circ\text{C}$ .

The combination of all these changes increased the time of 445%:

$$t_2 = \frac{Q_2}{P_{in}} = \frac{m_2 C_{p(Al)} \Delta T_2}{P_{in} M_{Al}} = 20.76 \text{ min} \quad (\text{Eq. 59})$$

This is the heating time of an arm subject to the constant heat produced by the maximum thruster testable by the stand. In a real case, the test time of a thruster would be less than 10 minutes, therefore the calculated value is acceptable. Anyway, the mass value and the limited temperatures of the LEDs couldn't be higher.

One idea expects that just for elevated thrust test, a secondary aluminium arm, with the same length but outer width of 3 cm and inner of 2 cm, could be put inside the one with inner of 3 cm. This was thought because the changing mass modify the Inertia of the system and makes the pendulum less sensible.

For example, for a thrust of 200 nN, initial arm temperature of 0°C,  $\Delta T_2$ , and  $m_1$ , mass of the initial designed arm, the final LED working time would be:

$$t_3 = \frac{Q_3}{P_{in}} = \frac{m_1 C_{p(Al)} \Delta T_2}{P_{in} M_{Al}} = 30.30 \text{ min} \quad (\text{Eq. 60})$$

Or the maximum thrust force could be limited to 300 nN for the first tests.

These are just initial considerations because more effective ones could be done with real data on the future LED thrust that will be tested, it could be possible that these LED will have efficiency higher than 40%, more elevated upper limit working temperature or lower.

## 6.2 Auxiliary damping system

The system presented in Chapter 5 was designed as an external damping system necessary to slow down the oscillation effects made by the thrust on the arm. Due to the necessary experimentation of this system never found in literature, it was decided to use also an auxiliary damping system that could calibrate and verify the correct functioning of the first. As the first one the system should be external, so no oil damping was evaluated.

From the analysis on existing thrust stand of Chapter 1.5 the most recent and simple system was the one used by *Soni and Roy* [10], Chapter 1.5.9. The typology chosen for their thruster stand was an electromagnetic damping system using eddy-currents, a non-contact method inherently frictionless generated inside a conductor by a changing magnetic field in it.

The damping effects works when a magnet moves over a conductor, this movement inducts eddy currents inside the conductor, as explained by the Faraday's law of induction, and those generating their own magnetic field opposing the magnet movement make it slow down. The idea was to put a permanent magnet at the extreme of the short swing arm, side facing down on a copper block. Varying the distance between the magnet and the copper block the damping coefficient can be modified.

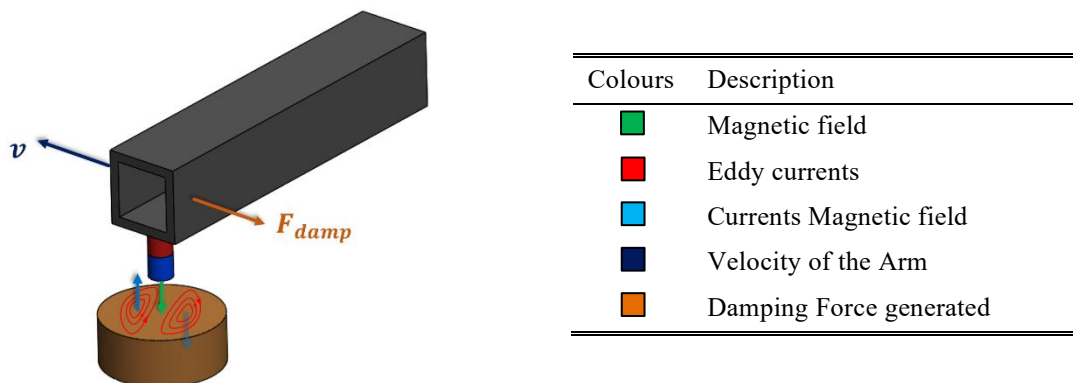


Figure 77: Eddy-current damp system; Legend.

This may always be active during the assembly and operating procedures of the vacuum chamber to prevent side vibrations, and then if the primary damping system is active, the copper block will be moved away from the magnet during the thruster tests.

A research was made to find information about the sizing of this technology, but no specifications were found. So, the idea was to choose the same components of the ones used in real thrust stand. In the *Soni and Roy* system a cylindrical copper block of high conductivity was mounted on the balance arm, diameter  $2\frac{1}{2}$ " and height of 1" , and 2 neodyum permanent magnets placed under it, each one of  $\frac{1}{2}$ " and height of  $\frac{1}{2}$ " and a magnetic flux  $B_{surface} = 6619\text{ Gauss}$  [65]. The amount of damping was controlled by varying the gap between the copper block and the permanent magnet from 0.5 up to 3 mm.

The same components used by *Soni and Roy* were chosen for this project, the real efficacy of the system will be tested in future once built, the gap between the magnets and the copper block will permit to set the damping ratio value. For redundancy, if the primary damping system is ineffective, the auxiliary system will become the main system, without affecting the possibility of performing tests.

### 6.3 Fiber Selection

Once defined the weight of the swing arm that could be used as a heating block, it was necessary verify if the fiber chosen could hold up it. In a previously thesis on this project it was suggested to use a steel fiber of diameter  $550\ \mu\text{m}$  for the elevated safe carrying capacity. In Table 13 are reported the fiber data:

Fiber Length (m)	0.75
Fiber Diameter ( $\mu\text{m}$ )	550
Fiber Material	Steel
Tensile Strength (MPa)	1200
Spring constant ( $\text{Nm}/^\circ$ )	$1.714 \times 10^{-5}$

Table 13: Data of the thrust stand fiber.

Below the definition of the components weight is presented:

- 1) **Arm:** As analysed in Chapter 6.1 for thrust lower than 300 nN, the pendulum's arm weigh is  $m_1 = 2.835\text{ kg}$ , while for the second configuration with a little arm inside the standard one, thrusts from 300nN to 500nN,  $m_2 = 4.860\text{ kg}$ .
- 2) **Battery:** To power a LED of 227.3 W for 30.30 min a battery of 114.79 Wh is needed, or rather 120 Wh. The capacity to mass ratio of lithium ion batteries is 40 Wh/kg, thence  $m_{B1} = 3\text{ kg}$  of battery. For the second configuration the max LED power is 378.8 W, the needed battery for 21 minutes is of 132.58 Wh, or rather 135 Wh and weight  $m_{B2} = 3375\text{ kg}$ .
- 3) **Additional:**  $m_+ = 2\text{ kg}$ , in this value the weight of cables, LEDs, power control and of the magnets are considered.
- 4) **Total:**  $m_{tot1} = 8\text{ kg}$  and  $m_{tot2} = 10.5\text{ kg}$ .

The steel fiber of  $550\ \mu\text{m}$  with averages tensile strenght value of 1200 MPa can support up to 29.06kg and with a security factor of 1.5 up to  $m_{limit} = 19.37\text{ kg}$ . So, there should be no problems for the use of the first or second configuration.

Due to the proximity of batteries weights of the two configurations, the heaviest will be used, so  $m_{tot1} = 8.4\text{ kg}$

The length of the fiber could be the same of the one suggested in Chapter 3.1, so also the effective spring constant of the system is the same.

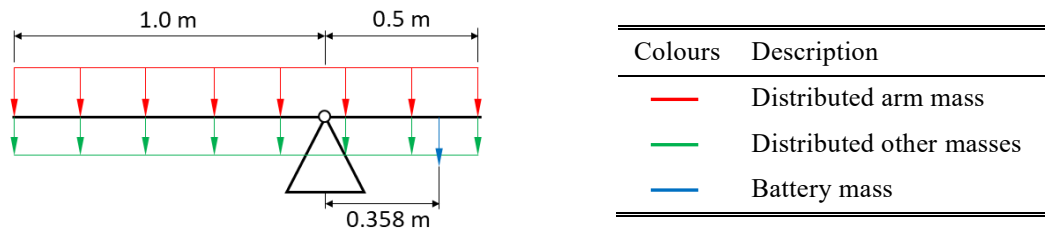


Figure 78: Force diagram acting on pendulum; Legend.

The battery is placed on the short arm and works as counter balanced weight, so its position was calculated considering the additional weight  $m_+$  distributed on the total length of the arm. For the first configuration it should be placed at 0.358 m from the fiber, Figure 78, while in the second at 0.508 m. So, there should be an adding mass of 1 kg on the short arm side of the pendulum without changing the battery position, the increasing total weight up to  $m_{tot2} = 11.5 \text{ kg}$  doesn't create problem thanks to the elevated  $m_{limit}$ . Also, if the adding mass is aluminium the time  $t_2$  calculate in chapter 6.2 became:

$$t_2 = \frac{Q_2}{P_{in}} = \frac{m_2 + C_p(Al) \Delta T_2}{P_{in} M_{Al}} = 25.03 \text{ min} \quad (Eq. 61)$$

making the use of a second configuration more convenient.

In Figure 79 is reported the swing arm with all the components described before and on the left the thruster tested and the mirror of the damping system. As anticipated in the Chapter 5.2 the mirror has diameter of 15 mm, but for the final concept could be increase to 20 mm.

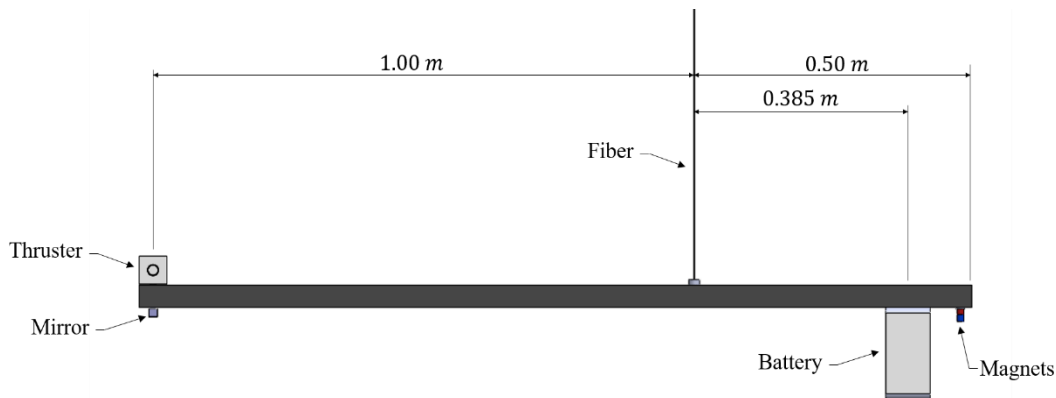


Figure 79: Complete arm configuration.

## 6.4 Calibration Method

As analysed in Chapter 1.4, existing thrust stand based on fiber or spring torsion pendulums have a calibration method to determine the system's effective spring constant. Common calibration methods include applying a known force or applying a known impulse, but recently analytical calibration methods are also used to find the unknown spring constant [35].

The calibration procedure of a thrust stand should generally be kept similar to the desired measurement procedure in terms of force range and force type, steady-state or impulse.

The stand presented in this thesis favours steady-state operations, so impulse calibration methods were not evaluated.

*Soni and Roy* [10] chose as calibration method for their stand one based on the logarithmic decrement method, they obtained a calculation error for  $k_0$  of 20.6%, most of it caused by the accuracy of the observed natural frequency. This accuracy is comparable to that obtained by other methods, so it was chosen as calibration method for the thrust stand presented here. The balance could be calmed previous to calibration and measurements allowing successive calibration and measurement by reducing the resting time of the system.

The logarithmic decrement calibration method is an analytical method used to calculate the effective spring constant via the observed damped frequency and the damping ratio of the system. The damping ratio is determined with the logarithmic decrement of two successive oscillation peaks [66]. The logarithmic decrement  $\Lambda$  of  $n$  oscillation cycles is defined as:

$$\Lambda = \frac{1}{n} \ln \left( \frac{x_0}{x_n} \right) \quad (\text{Eq. 62})$$

with  $x_0$  and  $x_n$  as the amplitudes of the first and the  $n^{\text{th}}$  peak of oscillation.

The damping ratio  $\zeta$  can then be calculated by Eq. 63:

$$\zeta = \frac{1}{\sqrt{1 + \left( \frac{2\pi}{\Lambda} \right)^2}} \quad (\text{Eq. 63})$$

from which it is possible to determine the natural frequency  $\omega_n$  via the relation between the system's natural frequency and the observed damped frequency of the system  $\omega_d$ , Eq. 20.

The effective spring constant  $k_0$  of the system is then calculated by reformulating equation Eq. 17, where  $I$  is the system's moment of inertia which must be determined prior to calibration with very high precision. The moment of inertia could be calculated using the parallel axis theorem and the superposition of the moments of inertia of the thrust stand's component shapes, as made by *Soni and Roy*.

They also determined that the error of the logarithmic decrement method is generated by uncertainty values of the determined system's moment of inertia and the observed natural frequency. So, they formulated an uncertainty equation for the logarithmic decrement method for  $k_0$  [10]:

$$\frac{\delta k_0}{k_0} = \sqrt{\left( \frac{2d\omega_n}{\omega_n} \right)^2 + \left( \frac{dI}{I} \right)^2} \quad (\text{Eq. 64})$$

One major downside of the logarithmic decrement method is its increasing inaccuracy for damping ratios greater than 0.5, which limits the maximum thrust stand damping, therefore increasing the expected response and relaxation time.

However, the method clearly brings a lot of advantages like the absence of the need for special calibration equipment, other than the devices already built-in in the system, as well as the methods' simplicity. It also allows for calibrations at different displacements and damping coefficients, thus ensuring the linearity of  $k_0$  over the desired measurement range and minimizing errors related to single-time events like steps or other harsh vibrations.

## 7 Measurement System

As mentioned at the end of Chapter 4 a new measurement system based on laser deflection was needed. At first, starting from basic laser deflection it was designed a visible measurement system on a chart, improved using lenses. After it was decided to create an electrical measurement system upgrading the one designed previously. A visibly measurement system based on laser deflection was already used by *Phipps and Luke* in the first version of the 2002 [6], then to increase the accuracy of measurement they decided to use a March-Zehnder interferometer in the second version of the 2006 [7]. The possibility to use an interferometer for this project was declined for a cheaper and simpler solution, as the one used by them in 2002.

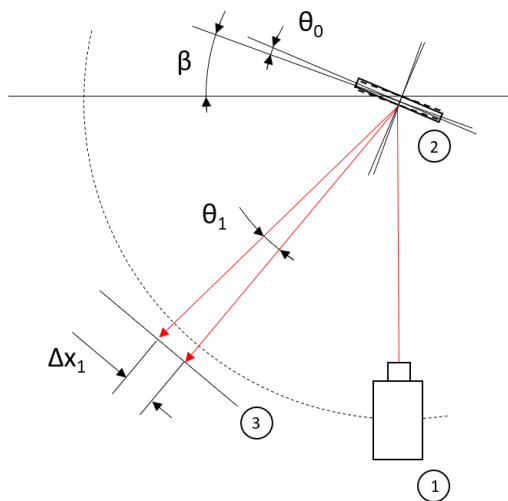
The sensibility of the system should be of 10 nN as reported in the requirements of Chapter 2.1.

### 7.1 Laser Deflection System

In this subchapter two concept of measurement system based on laser deflection are described, the first is a basic laser deflection, while the second is an upgrading of the first improving the sensitivity of the measurement using lenses.

#### 7.1.1 Simulation n°1

The design of the measurement system started with the definition of how the system should work. A laser inside or outside the vacuum chamber strikes a on a mirror, size 20 x 20 mm, that is fixed on the steel fiber of the pendulum. The rotation of the arm  $\theta_0$  makes the mirror rotate deflecting the laser beam for an angular displacement  $\theta_1$ . The beam hits a plane screen outside the vacuum chamber where the displacement  $\Delta x_2$  could be visibly or electronically measured, as shown in Figure 80.



Measurement system	
N°	Component
1	Laser source
2	Mirror
3	Screen

Figure 80: Basic laser deflection Simulation n°1; Components;

To simulate the system a MATLAB script was made. Simulation n°1 is a system with a laser source distant 0.25 m from the pendulum fiber.

As first approximation, the beam is perpendicular to the mirror plane, so no initial inclination  $\beta = 0^\circ$ . To have information about the final diameter of the laser beam there were supposed a divergency  $\theta = 1.2 \times 10^{-3} rad$  and an initial beam diameter of  $D_0 = 1 mm$ , these values were chosen after a research on existing laser sources,.

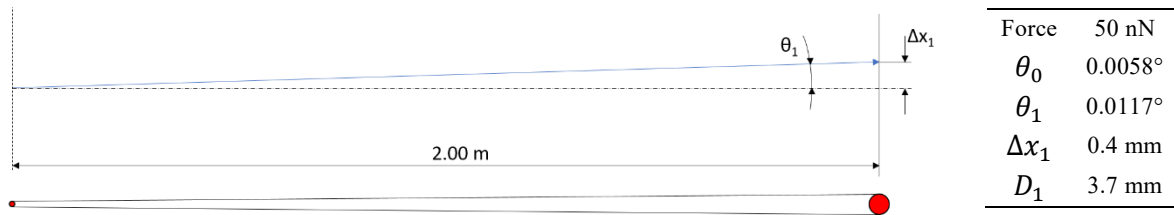


Figure 81: Simulation n°1: Scheme after mirror deflection and results; Results.

The Figure 81 shows what happen at the beam after the mirror deflection. The system was simulated with the minimum force,  $F_{min} = 50nN$ ,  $\theta_0 = 0.0058^\circ$  is the angular displacement of the arm,  $\theta_1 = 0.0117^\circ$  is the deflected beam angle and is the double of  $\theta_0$ . On a fixed screen at  $L = 2\text{ m}$  from the mirror  $\Delta x_1 = 0.4\text{ mm}$  is the distance between the laser initial point, for  $F = 0nN$ , and the calculated one.  $D_1 = 3.7\text{ mm}$  is the diameter of the beam on the screen.

It is possible to see that  $\Delta x_1$  is too small to be visibly measured, factors that influence this value are the distance  $L$  and  $\theta_1$ . Changing the initial inclination of the mirror  $\beta$  generate a differents  $\theta_0$  and  $\theta_1$ , but not  $\Delta x_1$ . The solution came from the autocollimator measuring principle, shown in Chapter 4.1.1, where lenses are used to collimate or focus the laser or LED beam.

### 7.1.2 Simulation n°2

For the Simulation n°2 it was decided to use two lenses, one Plano-Concave and one Plano-Convex. The converging lens is posed inside or outside of the chamber on the laser way after the mirror deflection, so to collimate the beam respect its initial direction, then a diverging lens amplify the angular displacement in order to obtain a higher  $\Delta x_2$  on the screen. The Figure 82 shows the schematic configuration of the simulation.

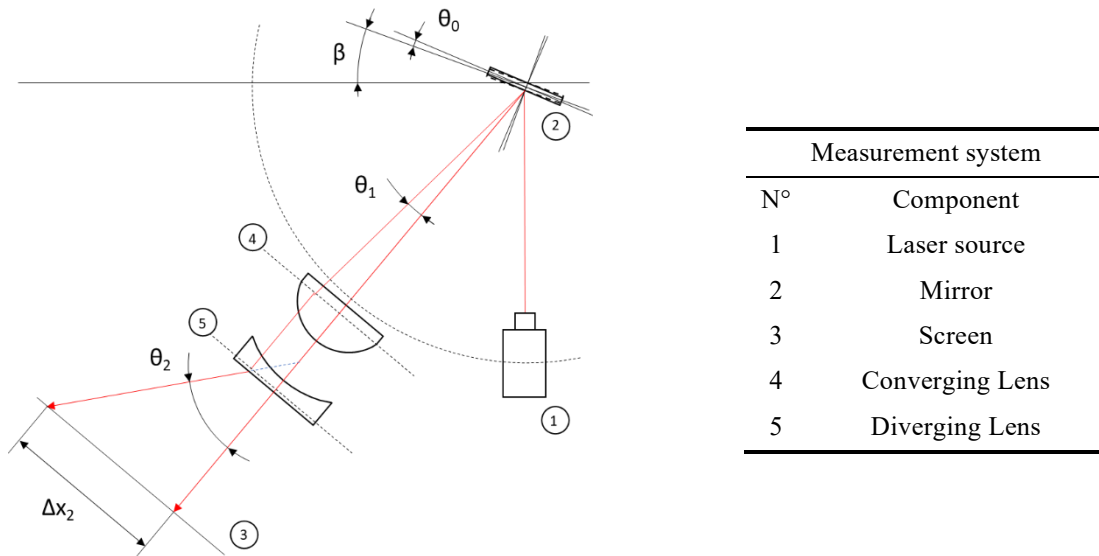


Figure 82: Schematic configuration of Simulation n°2; Components.

In this case the final length displacement is  $\Delta x_2$  and the angular  $\theta_2$ . Like in Simulation n°1 as first evaluation there is no initial inclination  $\beta = 0^\circ$ , but this value will be changed one time that the thrust stand is built to adapt the system to the vacuum chamber window. Anyway, for  $\beta \neq 0^\circ$ ,  $\theta_0$  and  $\theta_1$  would change but not the final  $\Delta x_2$ .

Two different lenses configuration were designed in order to test the system:

- 1) the first one with a Plano-Convex Lens (Uncoated) LA1252 ( $\varnothing 25.0$  mm N-BK7) [67] and a Plano-Concave Lens LC1054 ( $\varnothing 1/2$ " N-BK7) [68];
- 2) the second one with a Plano-Convex Lens (Uncoated) LA1464 ( $\varnothing 1$ " N-BK7) [69] and same Plano-Concave lens as before [68].

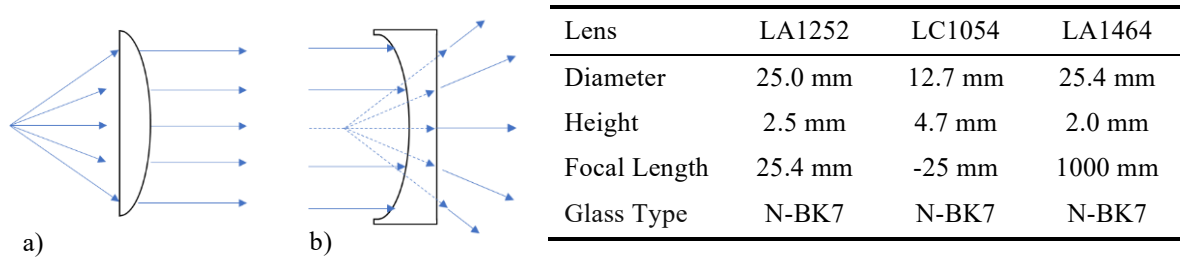


Figure 83: a) Plano-Convex lens; b) Plano-Concave lens; Characteristics.

In Figure 83 the lenses data are reported. The lenses positions were chosen depending on the focal lengths of each one,  $L_1$  is the distance between the mirror (fiber) and the first lens on the beam way,  $L_2$  from the second to the screen. The distance between the lenses was chosen to reduce the laser beam diameter. In Figure 84 are shown the results this simulation.

The first configuration showed an increment of 90.4% for displacement  $\Delta x_2 = 3.6149$  mm, while 208.7% for the second configuration,  $\Delta x_2 = 8.3499$  mm, making this last one a better option.

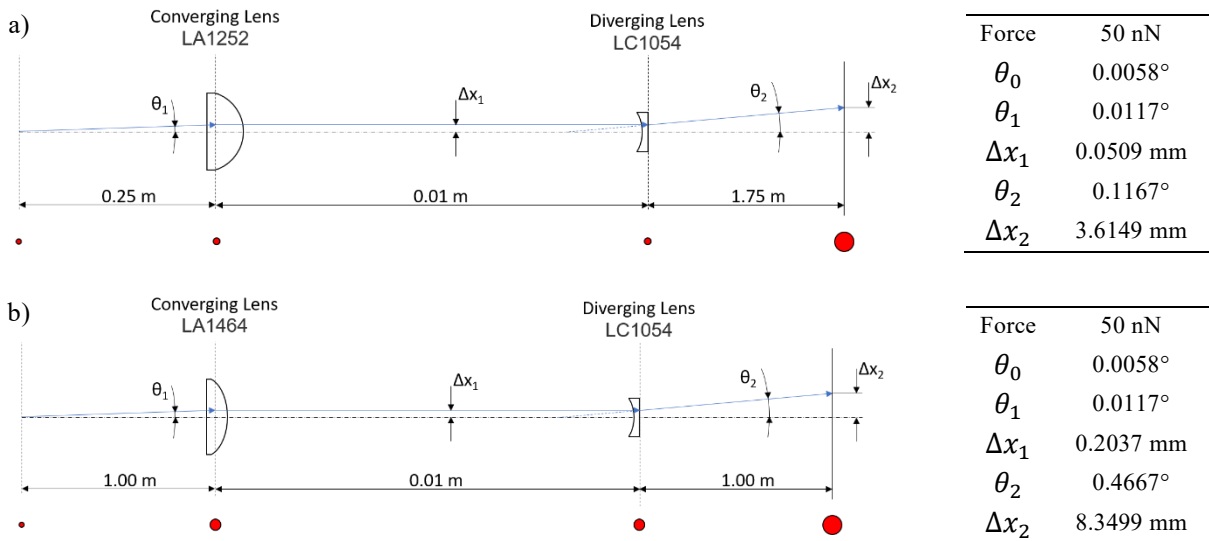


Figure 84: Simulation n°2: Scheme after mirror deflection a) Conf. 1; b) Conf. 2; Results.

The simulation also analysed the final diameter of the beam  $D_2$  compared with the displacement  $\Delta x_2$ . It can be seen from Figure 85 that diameters values are similar for those, but in the first configuration the big size of  $D_2$  and the small displacement  $\Delta x_2$  make difficult to appreciate with accuracy the different between the tests for  $F = 0$  nN and  $F_{min} = 50$  nN.

It was also made a qualitative analysis on the light intensity of the final beam on the screen. Assuming that the laser has a Gaussian beam profile and that the Full Width at Half Maximum (FWHM) is half of the diameter before the Plano-Convex lens [70]. The final beam diameter for half intensity was calculated to have an idea of how the image on the screen will be and an idea of the difficulty measurement level.

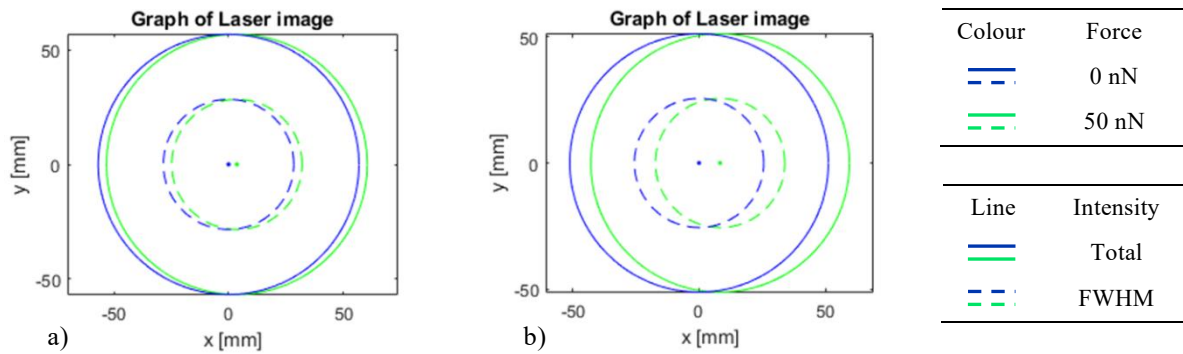


Figure 85: Simulation n°2 laser beam diameter: a) Conf. 1; b) Conf. 2; Legend.

The ideal measurement system should provide a sensibility of 10 nN but with a simple system, like the ones described in this chapter, it is difficult to reach this value, in Table 14 are reported the sensibility values of Simulation n°2.

	Option 1	Option 2
Sensibility $\Delta F$	25 nN	25 nN
Displacement $\Delta x$	1.8 mm	4.2 mm

Table 14: Sensibility Simulation n°2;

The configuration 2 was chosen as solution of the thrust stand, it is a visible measurement system with sensibility of 25 nN for a displacement of 4.2 mm that could be used for an initial efficacy evaluation of LEDs thrusters. Then as reported in Chapter 4.4 in case of good results of this technology will be take in evaluation the purchase of an autocollimator.

## 7.2 Electrical-Digital Measurements

The system presented before was based on visible measurements of the length displacement, from where it is possible to calculate the angular displacement of the arm and then information about the force of the thrusters as explained in Chapter 3. It would be easier to design a system that electronically measure the displacement.

The idea is not to have a measurement of the intensity of the laser light, but information about where it is lighting. To do that it could be used a line of photoconductive photocells. These components based on semiconductors, linearly vary the electrical resistance depending on the intensity of incident light. For this project they could be used as light sensors, in order to have information about the presence or not of Laser beam.



	Characteristics (T=25°C)
Size	4.3 x 5.1 x 2.4 mm
Dark resistance	1 M $\Omega$
Illuminated resistance	8 up to 20 k $\Omega$
$\lambda$ range	400 to 700 nm
$\lambda$ peak	540 nm

Figure 86: Photoresistor LDR GL5528 shape; Characteristics [71];

To reach a good sensibility of the instrument, each photocell should have sizes close to the system sensibility. So, they should be close to 4.2 mm or less and they should be in a number to archive the double of maximum displacement for  $F_{max} = 500nN$ , that generates  $\Delta x_2 = 83.5 mm$ , and  $\Delta x_{tot} = 167 mm$ . In Figure 86 are reported the data of the chosen photoresistor LDR GL5528 [71].

For a length of 167 mm, a line of 40 cells is required. They could be controlled by an Arduino but considering that a normal one has only 5 analogic pins, some multiplexers are needed. Each multiplexer usually has 3 or more digital outputs, so an Arduino Mega is needed.

The first idea is to use 5 8-channel analog multiplexer 74HC4051 [72], connected all of them to the Arduino Mega. Each photoresistor is an analog output, so 8 photoresistor are connected to each multiplexer. All the data would be transferred by the board to a computer and analysed, or from the Arduino itself, a graph would show which cells are illuminated by the laser beam. These data would be also sent to the MATLAB script of Chapter 3, to calculate the Force value of the testing thruster.

In order to improve the efficiency of the photocell they could be placed inside a black box with an open side facing the laser beam. Also, the laser could be chosen with the wavelength close to the  $\lambda$  peak of the photocell, colour green.

The servomotor and the damping system could be also controlled by the same Arduino.

In Figure 87 is shown the ideal configuration, the LDRs illuminated by the beam create a distribution of intensity registered by the MATLAB script and depending on the max of the curve the position of the laser is determined, so also the angular displacement of the arm.

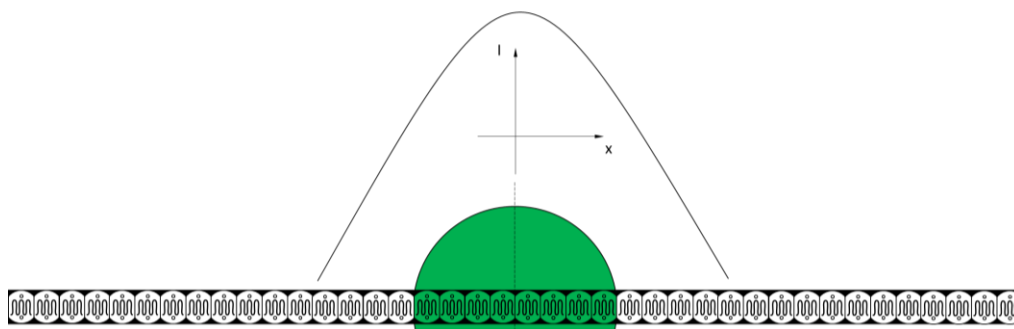


Figure 87: Simulation of electronic measurement using photocells.

## 8 Power and Control systems

This chapter is about the design of power and control system needed to power supply all the system of the thrust stand. The main power is provided by a power source at 12 V and for a correct sizing of the system all the components are considered working at maximum power.

The first subchapter is about the calculation of the power needed by the damping system, the second on the power of the measurement system and the third on the total power required by all the systems. Then there is another subchapter on the digital and analogic control made using an Arduino board.

The power of the battery on the short side of the swing arm was already calculated in Chapter 6.3, for the definition of the of the total weight of the arm. The design of the power control of this battery wasn't treated in this thesis due to the specific control needed by the future LED thrusters, that will be tested. But it could be imagined that a Buck or a Boost will be used to control the diode.

In the following figures to each component pictured is associated a number that correspond to components numeration of the list in Chapter 9.1.

### 8.1 Damping system Power Consumption

The components of the damping system that need to be electrically powered are the LEDs, the pump and fan of the cooling system and the servomotor that rotates pivot mirror.

First idea was to connect all the diodes in parallel, each one needs 4 V and 5 A, and to control the output voltage using only one buck converter. But another solution was chosen, due to the difficulty to find a converter with an elevated output of 25 A and the side effect of diodes parallel connection, the diode with the lowest forward voltage drop tries to carry a larger current risking overheating.

It was decided to use a buck converter for each LED. The ones chosen are 5 DC to DC Buck Converter (5 - 32V to 0.8 - 30V), with 5A constant output current capability and maximum power of 75W. In Figure 88 is reported the circuit diagram of the LEDs.

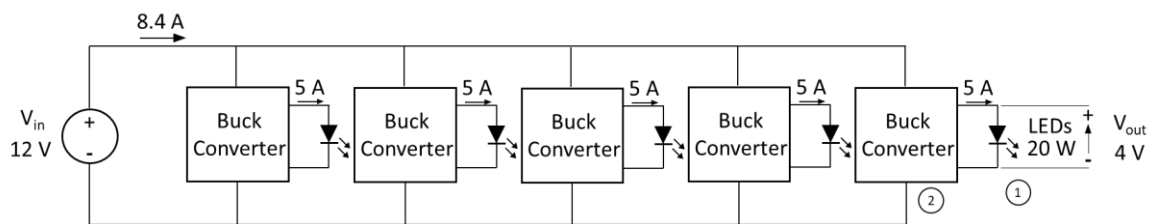


Figure 88: Circuit diagram of LEDs system.

Then the cooling system electrical power was designed. To control the fan airflow or the pump flow rate an optional buck converter could be used, as the DC to DC Buck Converter (3 - 40V to 1.5 - 35V), with a maximum output current of 3 A, and maximum power of 10W.

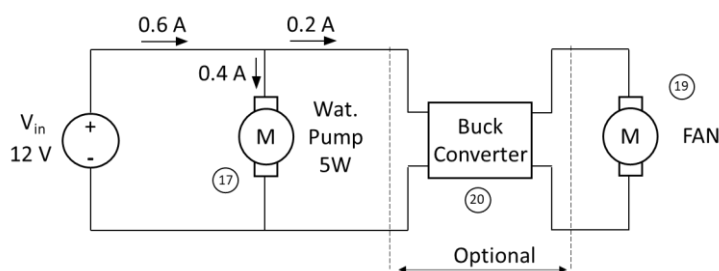


Figure 89: Circuit diagram of LEDs Cooling system.

The last electric component of the damping system is the servomotor that rotates the pivot mirror, its control is made by an Arduino board as explained in Chapter 8.4. For the servo the same Buck converter of the fan presented before was chosen, in Figure 90 is shown the circuit diagram.

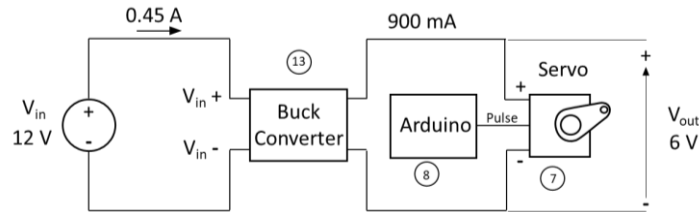


Figure 90: Circuit diagram of Servo rotating the pivot mirror.

## 8.2 Measurement system Power Consumption

The electrical components of the measurement system are the laser, the Arduino and the photocells. The chosen laser has a power output lower than 5 mW, this value does not generate an external force able to move the fiber where the reflecting mirror is disposed. The chosen colour is green to increase the efficiency of the photocells,  $\lambda_{\text{peak}}=520\text{nm}$  [73]. The divergency of the beam is lower than the one tested in Chapter 7.1, so the electronic measurement should be more accurate.

For the low value of current required by the laser it was decided to use a 50 mA Low Dropout Linear Regulator ADP3300, from 0.3 to 12V. One idea expects to increase the current needed by the Servo circuit up to 1 A and use the extra 100mA to power the laser, then a resistance of  $10\Omega$  could be used to drop the tension from 6 V to 5V required from the laser.

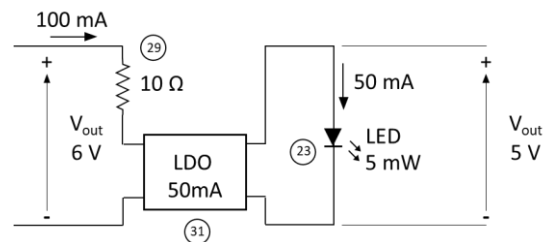


Figure 91: Circuit diagram of Laser, main voltage coming from Servo circuit.

Then the circuit of the 40 photocells controlled and powered by 5 multiplexers was designed. For each LDR a resistance between 1 and 10 k $\Omega$  could be used, as reported in the datasheet, the chosen ones are of 5.1 k $\Omega$ . Each multiplexer is powered from the 5V I/O port of the Arduino Mega. This board can work between 7 and 12 V but to avoid an excess of input voltage a buck converter at 7 V is used, same model as that used for the LED cooling system fan.

In Figure 92 the circuit diagram shows how 8 photocells are connected to each multiplexer, while in Figure 93 the circuit diagram of the Arduino which supplies 5 multiplexers is reported.

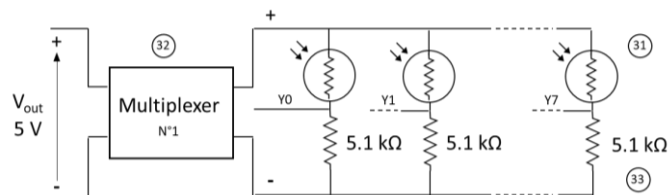


Figure 92: Circuit diagram of a Multiplexer with 8 Photocells.

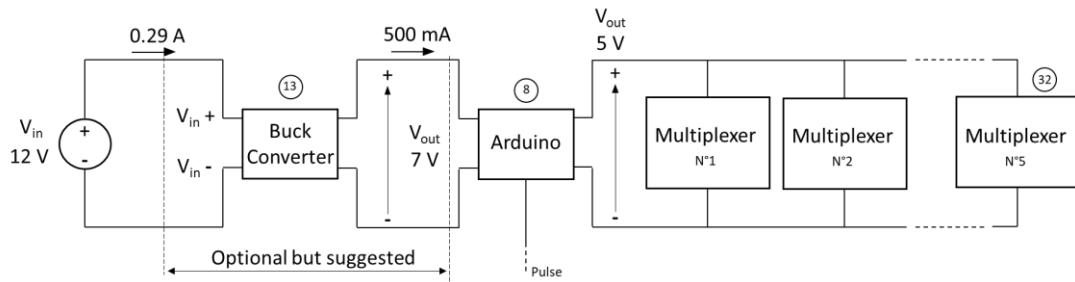


Figure 93: Circuit diagram of Arduino board supplying 5 Multiplexers.

### 8.3 Total Power Consumption

Then it was calculated the electrical power required for entire thrust stand. Considering a total efficiency of 90% the input current needed is 10.9 A, so a 150 W AC/DC converter with maximum current output of 12 A was chosen.

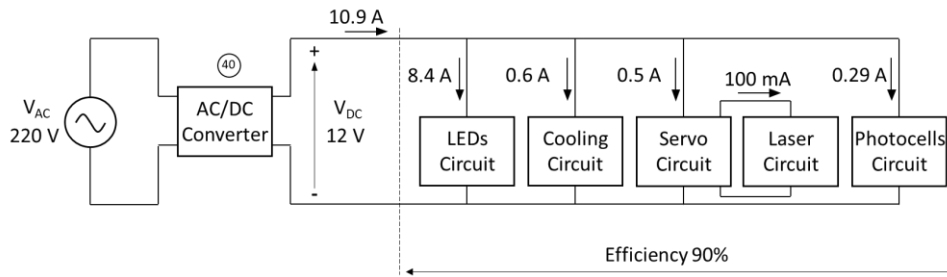


Figure 94: Circuit diagram of the thrust stand systems requiring electrical power supply.

### 8.4 LEDs Damping System Power Control

In this subchapter it is described how the damping system controls the power emitted by the LEDs. Each LED works at fix tension of 4V, the value of the radiation power emitted could be controlled varying the current of the diode from 0 up to 5A. As explained in Chapter 1.1.2 the relation between the radiation power and LED current could be approximated with a second order polynomial description, Eq. 4, here re-proposed with constant  $A_0 = 0$ :

$$\phi_e(I) = A_1 I_F + A_2 I_F^2 \quad (Eq. 65)$$

The chosen buck converter of Chapter 8.1 can be controlled in voltage and current by two trimmer potentiometers 3296W-103-ND [74] present on board. For simplicity, the one who changes the voltage will be call V-POT (Voltage control Potentiometer), while the other one C-POT (Current control Potentiometer).

The idea is to fix the output tension of each converter at 4V and vary the current rotating the yellow hat of the C-POT. This solution is effective but requires a manual control of the power supplied by the converter, the best idea should be to replace the trim pot with a digital one that could be controlled by an Arduino Nano. To do that it is necessary to have physically the converter board and test which digital pot may be suitable for the purpose, this is not a simple procedure and the pot couldn't be chosen before knowing how the board works. For that reason, two solutions were elaborated.

The first solution consists in a trim pots' rotation made by a servomotor. The first step is desolder the trim C-POTs from each converter board and then reconnected with extension cables, this to place the POTs where the servomotor system will work.

Then a gears system should be designed: a designed gear is fixed to each potentiometer's yellow hats and to the servomotor. The servomotor is posed at the centre of the system and rotating it makes rotate all the potentiometers' gears of the required same angle, called  $\gamma$ .

The design is shown in Figure 95 a), the servo is placed in the centre to provide the same rotating direction to all the gears connected to the potentiometers, in order that each converter supplies each LED with the same current.

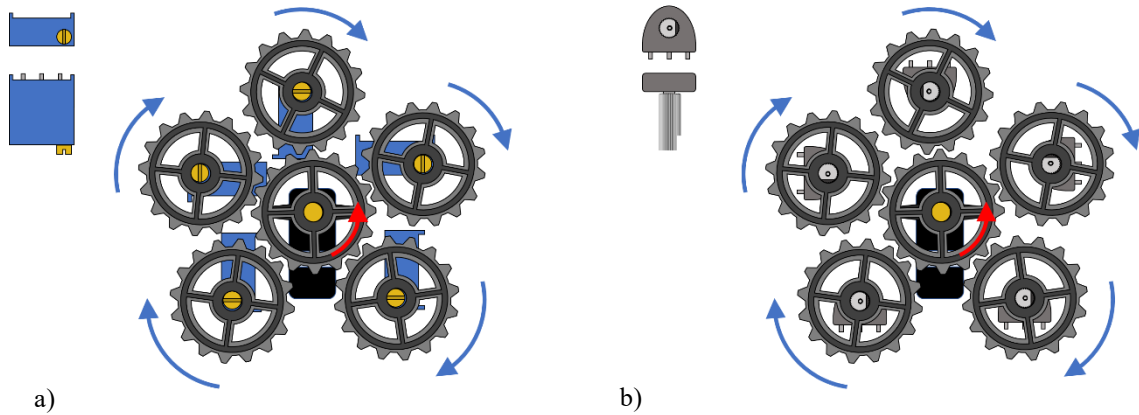


Figure 95: Gears system: Servomotor controls potentiometers rotations: a) Trim POT; b) Rotary POT.

The second solution is based on the same principle of the first one but changing the trim pot with a rotary potentiometer. The C-POT mounted on the board is a 10 k $\Omega$  trim potentiometer with an effective travel of 25 turns that could be replaced by a 10 k $\Omega$  rotary knob 3590S-2-103L with 10 turn [75]. The solution is shown in Figure 95 b) and it would be easier to control than the first one, thanks to the larger size of the rotating hat.

When the Damping system is built, each LED effective radiation power should be measured for each current caused by the rotation of the potentiometer  $I(\gamma)$ , so to define the values of the constants  $A_1$  and  $A_2$ .

$$\phi_e(\gamma) = A_1 I_F(\gamma) + A_2 I_F(\gamma)^2 \quad (Eq. 66)$$

Then the required rotation range of the potentiometers gears is defined, and the complete gears system could be sized.

The servo used for the gear system could be same model of the one chosen for the pivot mirror rotation, for the elevated stall torque and the angular displacement of 180°, or if necessary one with more than 360°. It could be controlled by the Arduino Mega of the measurement system or to prevent errors and improve efficiency by an Arduino Nano.

The task of the servomotor is to rotate for a specific angle each half period, to set the LED output power. This is similar to the mirror-servo's task, that is the rotation of the pivot mirror to direct focused light, so these two components could be controlled by the same Arduino board.

The mirror-servo's power supply is described in Subchapter 8.1 and the gear-servo could have the same circuit diagram, Figure 90.

They could be controlled by digital Arduino pins as shown in Figure 96, with the mirror-servo connected to pin 10 and gear-servo to pin 9. A simple Arduino script was created to try the servomotors work, and it's possible to set the initial positions and the rotation degrees.

The final idea is that the MATLAB program of Chapter 3 send back data to the Arduino about the mirror-servo and gear-servo new positions. The electrical power of the Arduino Nano could be made by connecting it via USB to the PC running MATLAB.

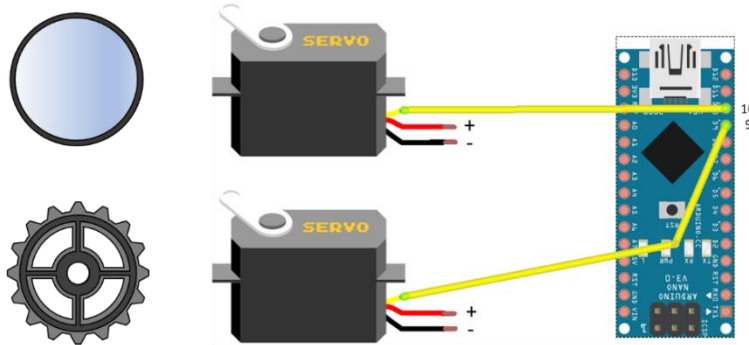


Figure 96: Damping system: Mirror-servo and Gear-servo control made by Arduino Nano:

## 8.5 Measurement System Digital Control

In this subchapter it is explained how the components of electrical measurement system, described in Chapter 7.2, interface with each other. The electrical power and the circuit diagram of each component was already treated in Chapter 8.2, therefore this part of the thesis works also as a guideline for assembly. The systems were designed with the program Fritzing in order to project and test functional scripts and design the configurations.

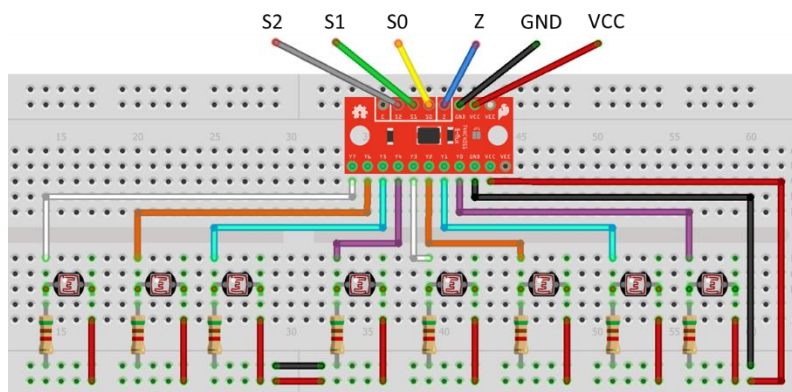


Figure 97: Multiplexer connections with photocells and resistances, and main pins.

In Figure 97 are shown all the physical connection between one multiplexer and the 8 photocells. Each multiplexer has 3 digital outputs S0, S1 and S2, and one analogic input Z, which are all connected respectively to the Arduino digital and analogic pins. Then the VCC and the GND are connected to the board power pins.

In Table 15 are reported all the pin connections between the Arduino Mega and each multiplexer, all the pins mentioned in the table are referred to the Figure 98 in the next page. The VCC and GND pins of each mux are connected in parallel with the power pins at 5V as presented in Figure 93.

	Multiplexer n°1		Multiplexer n°2		Multiplexer n°3		Multiplexer n°4		Multiplexer n°5	
	Digital	Analogic								
S0	22	-	25	-	28	S0	22	-	25	-
S1	23	-	26	-	29	S1	23	-	26	-
S2	24	-	27	-	30	S2	24	-	27	-
Z	-	A0	-	A1	-	A2	-	A3	-	A4
	Power		Power		Power		Power		Power	
VCC	M1+		M2+		M3+		M4+		M5+	
GND	M1-		M2-		M3-		M4-		M5-	

Table 15: All MUXes pins connections with Arduino Mega board.

An Arduino script was written to acquire data from all the photocells, when one cell is illuminated its value change from 0 up to a default value. These data could be sent to the MATLAB pendulum script to calculate the laser beam position, so to derive the angular displacement of the pendulum swing arm and then the Force of the tested thruster, as described in Chapter 7.2.

The Arduino Uno would have had a too low number of digital pins for this project, so the Arduino Mega became necessary, the free pins of this component could be used for futures upgrades.

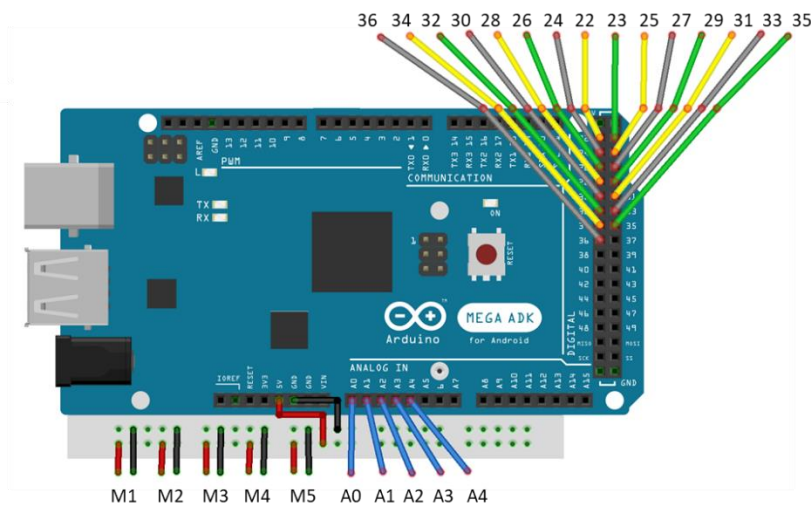


Figure 98: Arduino Mega pins connections with the 5 multiplexers.

## 9 Final concept

In this chapter the final concept of the thrust stand after the work made in the previous chapters is presented. At first a list with all the components of the stand is reported, then an explication on how the systems work, and at the end the cost analysis compared with the one made for the First concept, Chapter 4.3.

### 9.1 List of Components

In Table 16 are reported all the components of the thrust stand, for each one has been assigned a number, a basic information description is given and an estimate on the price of the product. Where the quantity is n.d. means that the number has not been defined yet.

While when there is an underlined price it means that the cost was estimated, because the actual one has not yet been provided by the seller or no information has been found.

N°	Component	Description	Qty	Price €
1	LED 20W	TX-1818W20FC65-CUVCNG-A01: Luminous flux: 1700 lm, Colour temperature: 7500 K, View angle: 65°, Diameter: 10 mm	5	<u>70.00</u>
2	DC-DC Step Down	Buck Converter: DC to DC 5-30V to 0,8-30V, Constant output current capability: 5A; Max power: 75W	5	11.95
3	LEDs Elliptic reflector	Length: 100mm tall, Diameter: 115mm, Characteristics: Characteristics: a) 235 mm; b) 67.9 mm; c) 67.9 mm	1	<u>50.00</u>
4	Rotary Pot	Model: Bluelover 5 3590S-2-103L, Capacity: 10K $\Omega$ , Turns: 10	5	15.89
5	Servomotor	Max stall Torque: 15 kg/cm (at 6 V), Dimensions: 54.1x20x44.3 mm	1	9.98
6	Arduino Nano clone	Elegoo Nano V3.0 CH340 ATmega328P	1	6.99
7	Servomotor	Max stall Torque: 15 kg/cm (at 6 V), Dimensions: 54.1x20x44.3 mm	1	9.98
8	Arduino Clone	Elegoo Mega 2560 R3 Board ATmega2560	1	14.99
9	Mirrors system Mirror 2 cm	Mirror Diameter: 20 mm	2	<u>1.00</u>
10	Mirror 7 cm	Mirror Diameter: 70 mm	2	<u>3.00</u>
11	Mirror 10 cm	Mirror Diameter: 100 mm	2	<u>3.00</u>
12	Mirror 12 cm	Mirror Diameter: 120 mm	1	<u>3.00</u>
13	DC-DC Step Down	Buck Converter: DC to DC 3 - 40V to 1.5 - 35V, Max output current: 3A; Max power: 10W	2	3.20
14	Water Cooling Block	Asiproper CPU Water Block water cooler Computer Cooler for Intel AMD + Screws/ To be modified	1	14.48
15	Thermal Paste	Arctic MX-2 Thermal Compound: Thermal Conductivity 5.6 W/(mK)	1	6.99
16	Heat Exchang. Radiator	KESOTO aluminium radiator water cooling for CPU 18 flat tubes 120mm, 150x115x30mm	1	10.22
17	Water Pump	Decdeal Max Height: 3 m, Power: DC 12 V and 5 W, Flow rate: 280L/H	1	5.75
18	Tubing	Masterkleer Schlauch Material: PVC, Diameter: 10/8mm (5/16"ID), Length: 3,3m (10ft)	1	10.19
19	Fan	Koolance FAN-12025MBK, Size: 120x25mm, Airflow: 90CFM	1	8.99
20	DC-DC Step Down	Buck Converter: DC to DC 3 - 40V to 1.5 - 35V, Max output current: 3A; Max power: 10W	2	3.20
21	Fittings	Connector: Size: Inner: $\varnothing$ 8 mm; Outer: $\varnothing$ 11 mm, Thread Size: 1/4 inch	4	18.76
22	Water Tank	Capacity: 1 litre	1	<u>4.00</u>

	23	Laser	Laser Diode: Colour: Green, Wavelength: 520nm, Output power: 5mW, Divergence Angle: < 0.7 mrad	1	66.00	
	24	Fixed Laser Stand	Adafruit Fixed Laser Mounting Stand [ADA1094]	1	8.53	
Laser system	25	Plano-Convex Lens	Model: LA1464, Size: Ø1" (Ø25.4 mm), Focal length: 1000mm, Material: N-BK7	1	17.36	
	26	Plano-Concave Lens	Model: LC1054, Size: Ø1/2" (12.7 mm), Focal length: -25mm, Material: N-BK7	1	15.95	
	27	Mirror	Size: 20x 20 mm	1	1.00	
	28	Screen	Millimetre sheet to visibly measure the angle displacement	1	1.00	
	29	Resistor 10	Resistor: 10 Ohm	1	0.25	
	30	LDO	Model: ADP3300, Low Dropout Linear Regulator: 50 mA	1	1.48	
LDRs	31	Photoresistor	Model: LDR GL5528, Size: 4.3 x 5.1 x 2.4 mm, Illuminated resistance: 8 up to 20 kΩ, λ peak: 540 nm	40	11.20	
	32	Multiplexer	SparkFun Multiplexer Breakout: 8 Channel (74HC4051), Wide voltage supply range: 2 – 10V	5	12.50	
	33	Resistor 5.1	Resistor: 5.1 KΩ	40	10.00	
Swing Arm	34	Fiber	Steel fiber: Diameter 550 μm, Spring constant: 1.714 x 10 <sup>-5</sup> Nm/°, Length: 0.75m	1	<u>70.00</u>	
	35	Aluminium bar n°1	Hollow Aluminium profile square cross section: Length: 1.5 m, Outer width: 40 mm, Inner width: 30 mm.	1	40.00	
	36	Aluminium bar n°2	Hollow Aluminium profile square cross section: Length: 1.5 m, Outer width: 30 mm, Inner width: 20 mm.	1	40.00	
	37	Battery	Lithium power supply: 40.80Ah, 3.7V, 150Wh, Output DC 12 V, Weight: 1.5 kg, Size: 80x165x175 mm	1	100.00	
	38	Copper block	Dimensions: 2 1/2" dia. x 1" thick, Material: Copper	1	40.00	
	39	Magnets	Surface Field: 6619 Gauss, Dimensions: 1/2" dia. x 1/2" thick, Material: NdFeB, Grade N52, Weight: 12.1 g	2	7.96	
Power system	40	AC/DC Converter	AC/DC converter: Input: 220 – 240 V AC/50 – 60 Hz, Output: 12 V DC, Max power 150W, Max current 12 A	1	29.90	
	41	Cable AC/DC	Cable to connect the AC/DC to the AC power	1	<u>2.00</u>	
	42	Cable	Cables to connect all the components to the power source	n.d.	<u>10.00</u>	
	43	Digital Multimeter	Necessary to test the system	1	<u>10.00</u>	
	44	Arduino Cable	To connect all the Arduino pins to the MUXes	n.d.	5.00	
				TOT	145	<u>786.00</u>

Table 16: List of the thrust stand components.

The Damping system was divided in LEDs, Mirrors system and Cooling system, while the Measurement system in Laser system and LDRs. The power system reported is not as the one presented in the chapter 8, because its electronic components were included in the rows of the subsystem that they power. So, only the AC/DC converter and all the electric cables were included.

As explained before same prices were supposed to have a reference value of the final stand's cost, all these prices are underlined in the table. The sum of all the supposed prices is 232€, while hypothetical the total cost of the thrust stand is 786€.

## 9.2 Design Description

This sub-chapter explains how the subsystems of the thrust stand are made and how they work, this information will be useful to build the system.

The power and control system are the only ones not treated here, because in Chapter 8 there is reported all the necessary information, also all its components inside the figures of that chapter have already been reported with the list number.

### 9.2.1 Damping System Operation

The damping system is composed by the groups that in Table 16 were called: LEDs, Mirrors system and Cooling system, all the data of the components of which they are composed are specified there.

As reported in Chapter 5 it was decided to use an elliptic reflector mirror with LEDs inside, each one distributed on the lateral faces of a copper pentagonal prism that is used also as designed water box. Each LED is an individual chip with a viewing angle of  $65^\circ$ , this configuration permit to focus all the light emitted by the diodes. In Figure 99 is shown how the components are disposed.

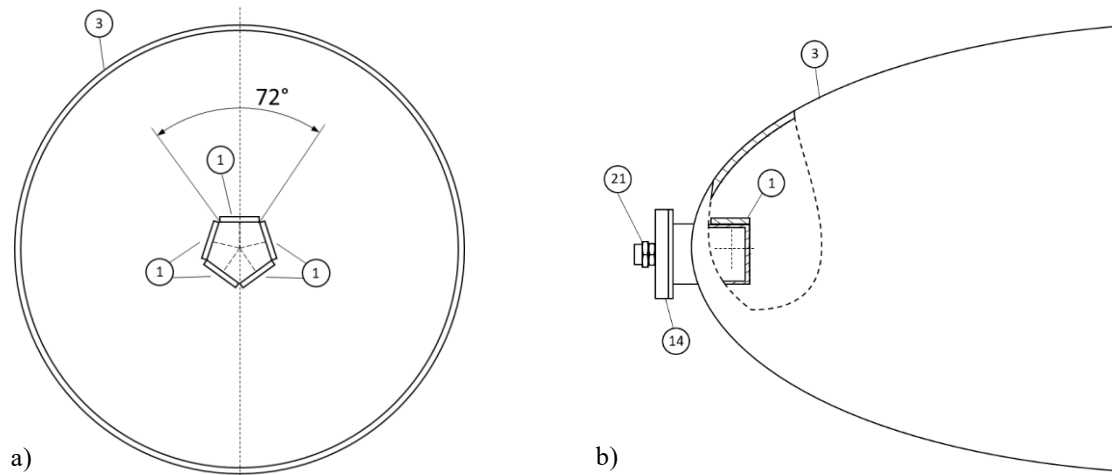


Figure 99: Reflector with LEDs, Water block and fittings: a) Front view; b) Side view.

Then it was designed a mirrors system to direct the light focused by the reflector to a small mirror at the end of the pendulum's arm. This is composed by a pivot mirror moved by a servomotor controlled by an Arduino Nano, the details of the operation are presented in the Chapter 5.2, and 4 circular mirrors arranged at  $45^\circ$ . The height of the whole system was set at 175 mm from the centre of the water block to the ground. In Figure 100 of the next page the side and top view of the system are shown, the Figure 100 b) has been cut due to its size, but the symmetry of the system allows it to understand its arrangement. The complete sizes of the system are: 280x260x175 mm.

After using the results of the last simulations presented in Chapter 5.2, the final size of the light beam that hits the mirror fixed on the swing arm was estimated. Each diode generates an individual beam with circular section but the reflection on the elliptical reflector changed the section to elliptical, the typical ellipse dimensions on the last mirror are 3.4x2.64 mm. Due to the different routes travelled by each LED beam the final dimensions of the ellipses on the mirror should be different. For that it was decided to electronically control each LED with a buck converter, in order to calibrate the output radiated power one time that the thrust stand is build, as explained in Chapter 8.4.

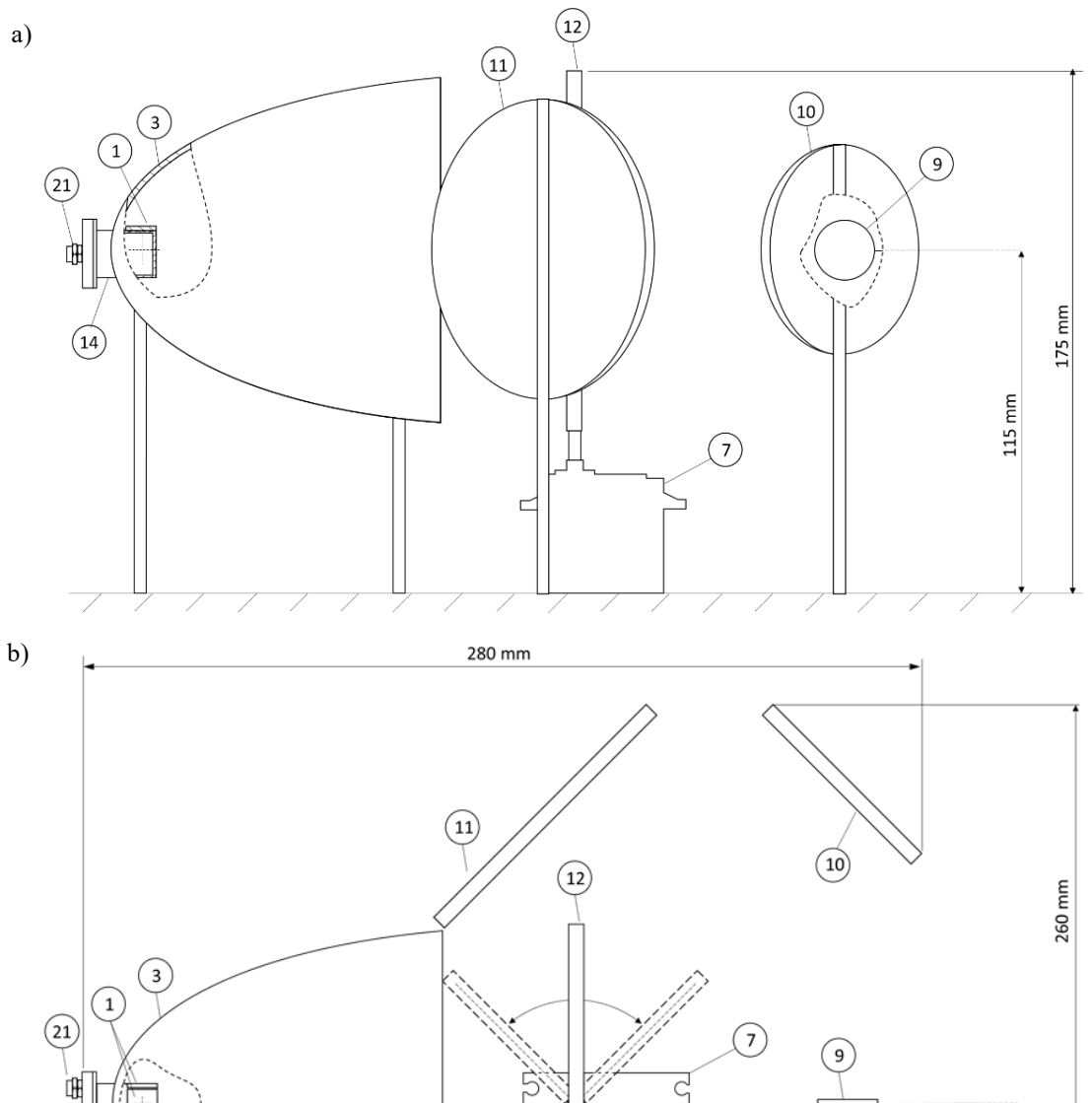


Figure 100: Damping system: a) Side view; b) Top view.

In Figure 101 the ellipses are shown in red, the colour indicates also the distribution of power intensity of the beam, it could be seen that the high intensity is close to the centre of the mirror. In Figure 101 b) are reported in red the force vectors of the LEDs beams, their reflections on the mirror generate the damping force perpendicular to the mirror plane, in green, as explained in Chapter 5.1.

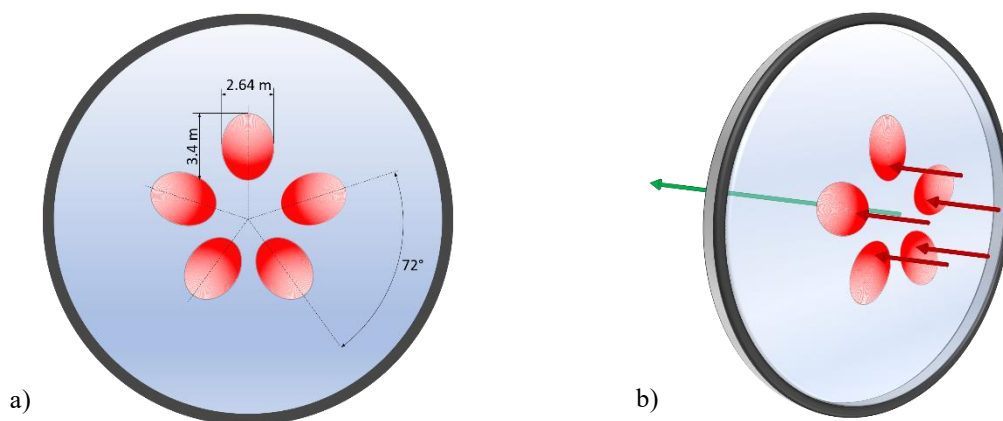


Figure 101: Light beams on the final mirror on the swing arm: a) Front view; b) 3D view.

Then it was designed the cooling system of the LEDs system, to avoid the exit of water inside the vacuum chamber, which would immediately evaporate due to pressure, it was decided to use fitting to connect the tubes with the water block, and outside to the exchange radiator. The pump should be mounted inside the water tank to a minimum depth of 30 mm from the water level. The length of the tubes will be evaluated one time that the system is built.

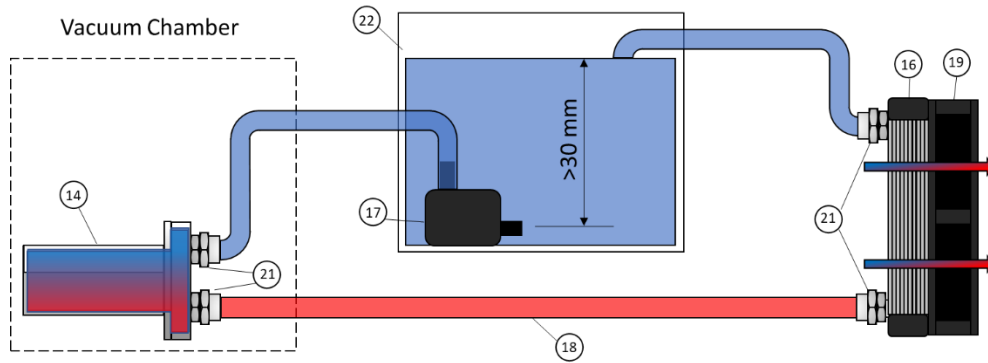


Figure 102: Water cooling system for the LEDs of the damping system.

### 9.2.2 Measurement System Operation

The measurement system is composed by the groups that in Table 16 were called: Laser system and LDRs, all the data of the components of which they are composed are specified there. The sensibility of the system is 25nN as explained in Chapter 7.

A laser source is fixed at 25 cm from the mirror fixed on the fiber of the swing arm, the positioning outside or inside depends on the actual size of the vacuum chamber, in any case it is fixed with a laser stand. The angle  $\beta$ , generated by the mirror face with the arm axis, depend on where there is a window to let the laser beam out. Then outside the vacuum chamber at 1 m from the mirror there are two lenses a plano-convex and a plano-concave that increase the angular displacement of the arm. At 1 m away from the last lens a screen detects the final deviation of the laser beam, as shown in Figure 103.

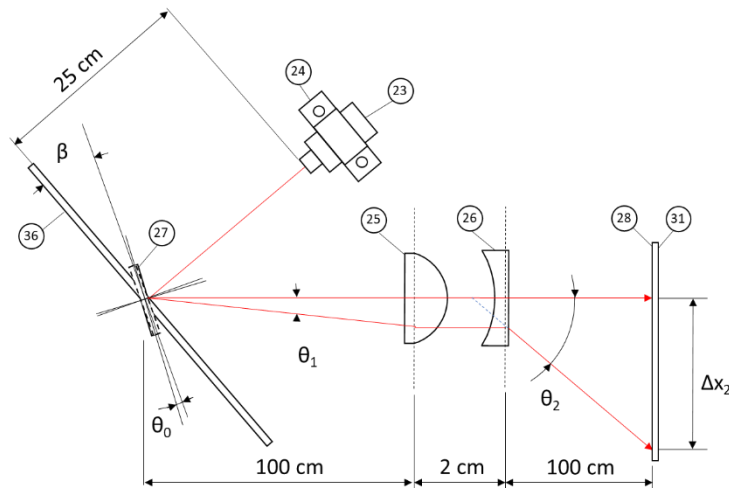


Figure 103: Measurement system based on laser deflection.

The final chosen laser source has better characteristics than the one tested in Chapter 7, so the final beam sizes on the screen were calculated again and they are shown in Figure 104 for the minimum and maximum force that can be test on the pendulum. The decrease size of the final laser beam allows to increase the effectiveness of the system [73].

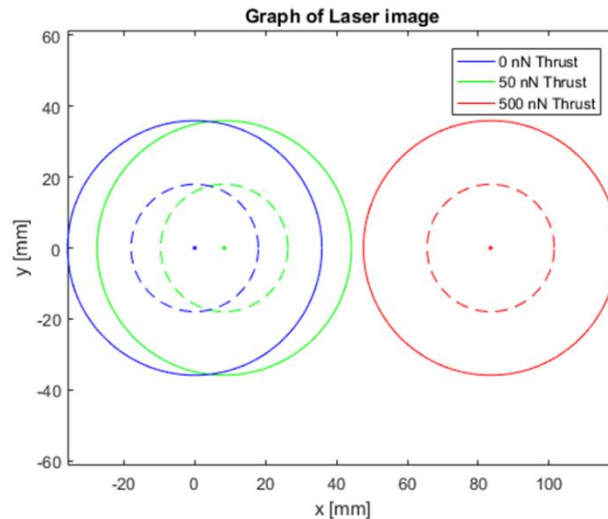


Figure 104: Final laser beam size, tested for  $F_{min}=50\text{nN}$  and  $F_{Max}=500\text{nN}$ .

The system was designed to detect manually or electronically the angular displacement, in the first case with a millimetre paper sheet used as a chart and in the second with a LDRs system that is composed by 40 photocells arranged in a straight line. Each LDR sends an analogic output to a Mux that transforms it into digital one and sends it to the Arduino Mega, which deals with the organization and sending of the data collected to the MATLAB program of Chapter 3. The operations of the system are described in Chapters 7.2 and 8.5. In Figure 105 is shown how should be the LDRs system.

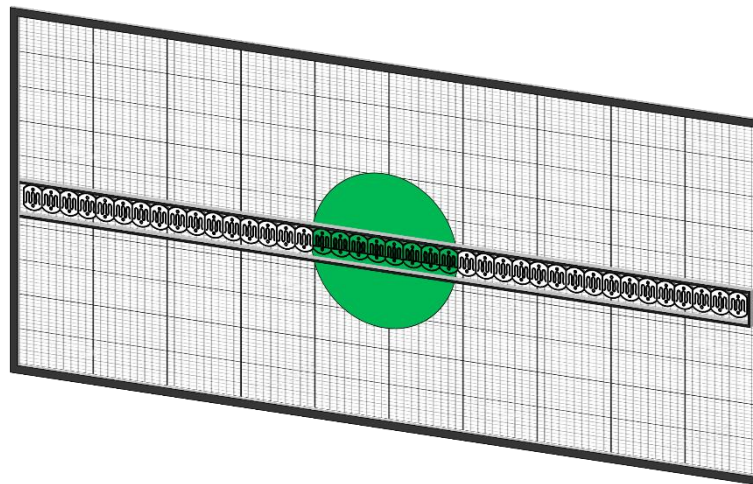


Figure 105: Screen to manually measure the angular displacement or electronically using the LDR system.

### 9.2.3 Swing Arm Operation

The swing arm is composed by the homonymous group presented in Table 16, all the data of the components of which it is composed are specified there.

The pendulum in Figure 106 was designed in Chapter 6. On one extreme of the arm are placed the mirror for the damping system and the future thruster that will be tested, on the other side the magnets, for the auxiliary eddy-current damp system, and the battery, to power the thrusters. The arm is used to detect the force generated by the thrusters tested, moving in 1 dimension, also it is used as a cooling block to accumulate the heat power produced by the thruster, to avoid a change in the junction temperature and make them work properly.

Before the test in the vacuum chamber the arm is cooled to the temperature of 0°C. If the main damping system is not active, the auxiliary one is used. The copper block of this system is posed on a support that can increase or decrease its height, varying the gap between it and the magnets, defining the damping ratio.

For forces bigger than 300nN a small section arm, with same length size, is put inside the main one to increase the capacity of the cooling block, this solution will be tested to verify the actual need of more cooling.

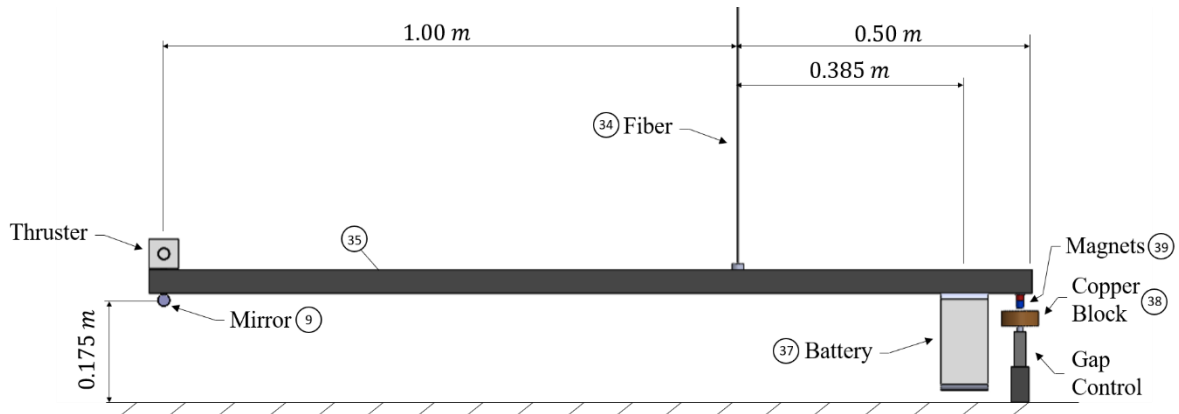


Figure 106: Thrust stand arm.

### 9.2.4 Nano Newton Thrust Stand by IRS

In the following figure is presented the final setup of the proposed thrust stand projected in this thesis. All systems are shown except for the cooling system of the damping system and the laser deflection of the measuring system, since they will be positioned outside the vacuum chamber and their assembly has already been described in Chapters 9.2.1 and 9.2.2:

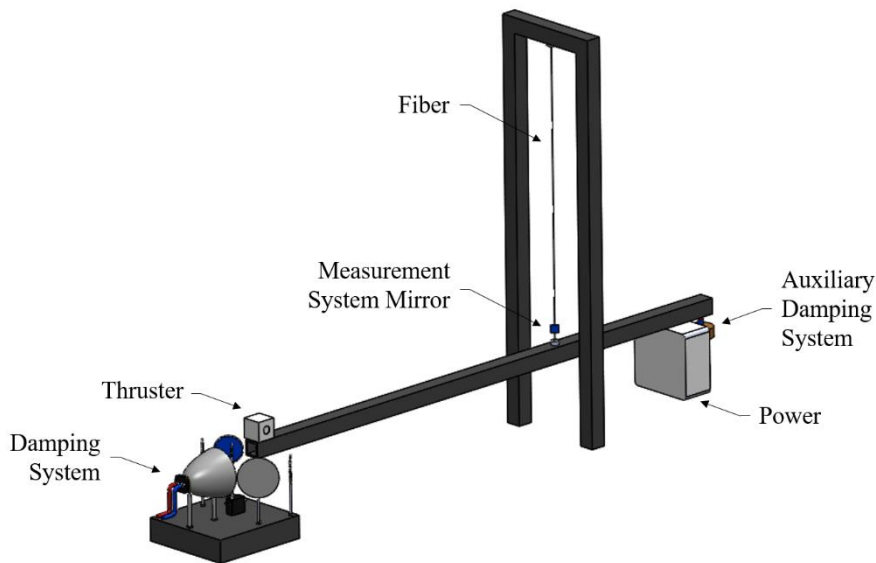


Figure 107: Schematic design of the IRS thrust stand configuration.

Also, in the Figure 108 the details of the damping system and of the auxiliary one are pictured.

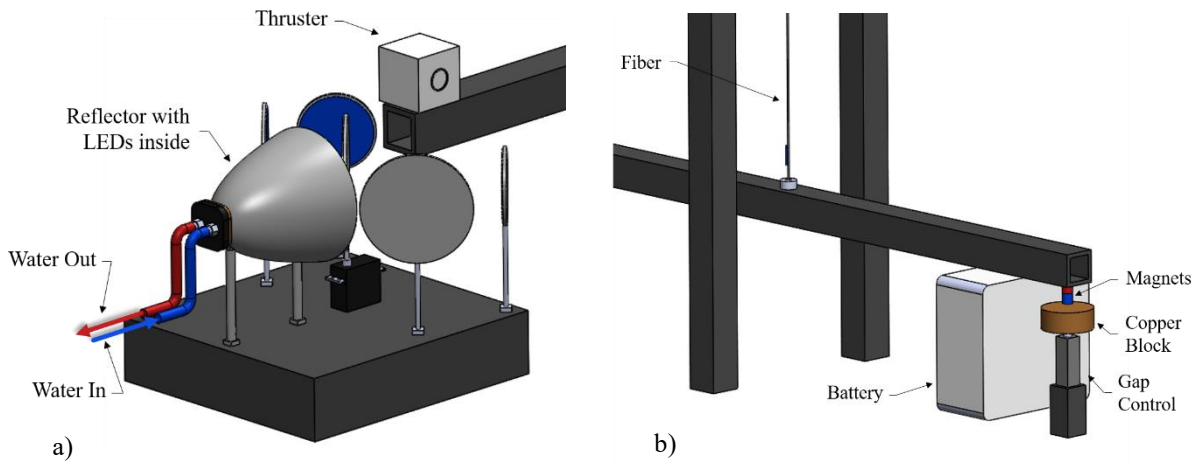


Figure 108: Details of the: a) Main LEDs electromagnetic damping system; b) Auxiliary Eddy-Current damping system.

### 9.3 Cost Analysis

The thesis work ends with a cost analysis of the thrust stand, as made for the first concept in the Chapter 4.3, compared to that concept the cost was reduced by 93% thanks to the non-use of an autocollimator.

In Figure 107 are reported the total price of each subsystem. The one having the highest price of 298€ is the swing arm due to the special steal fiber, that probably will be higher than the one estimated, and the high capacity battery to power the thrusters. The damping system that is composed by LEDs, Mirrors system and Cooling system has a total price of 286€, close to the one before, the components that make this value elevated are the LEDs and the reflector, for which it was supposed a cost of 50€ but probably could be higher considering that it should be built.

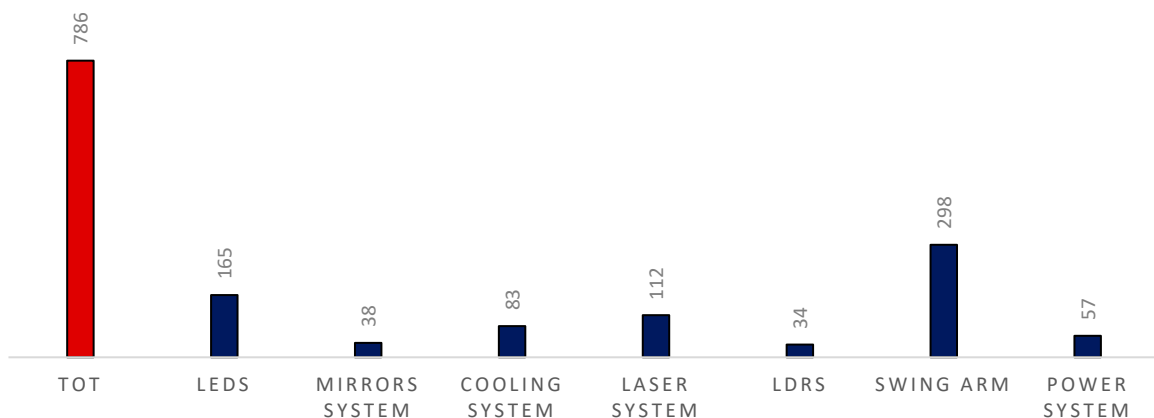


Figure 109: Cost analysis of the thrust stand.

The final cost calculated is less than 1000€ and the system could represent an excellent compromise for a first evaluation of the effects of electromagnetic radiation propulsors.

## 10 Conclusions

The system presented in this thesis is a first elaboration of a thrust stand with an innovative active damping system based on electromagnetic radiation, for thrusters in the micro and nano-Newton range. The scope of the work has been achieved, first an introduction and research on real thrust stand were made, to know how they work and starting from this analysis design an innovative one. Second the recognition of the requirements and boundary conditions was made, these were followed during the entire project. A MATLAB script was built to simulate a real thrust stand in order to accurately size the elements of the system. During the design the actual cost of the components has always been evaluated and the philosophy of a high efficiency and low-cost project has been followed.

An innovative damping system based on LEDs electromagnetic radiation power was designed, respecting the requirements, testing different configurations and providing MATLAB scripts to simulate the efficiency of the system. The high source generating the radiation power is based on the light focusing of 5 LEDs through an elliptic reflector and mirrors, its power and light direction control are made by an Arduino moving servos. The maximum force generated by system is of 151.63 nN and it permits to damp a thruster of 400nN.

A previous work on a first design of this thrust stand was very helpful to design the pendulum, then its arm was sized to detect the force of the thrusters and to absorb their heating power cooling them. An auxiliary eddy-current damp system was presented if the main one, being experimental, should not work properly.

The measurement system has a sensitivity of 25 nN and it was designed on laser deflection through lenses. The displacement data can be read on a graph, or electronically measured by a continuous line of LDRs, with an Arduino Mega that collects and digitizes them. The calibration is made using the logarithmic decrement method, the spring constant of the system is analytically estimated, from the system's damping ratio based on successive peaks of oscillation in conjunction with the measured damped frequency.

So finally, it was designed a steady-state thrust stand with thrust range 50 nN - 400 nN and a sensibility of 25 nN, that can be controlled and monitored by a PC using MATLAB, with a revolutionary damping system and an estimated cost less than 1000€.

This thrust stand could represent an excellent compromise for a first evaluation of the effects of electromagnetic radiation propulsors.

In future, in case of a positive results of electromagnetic radiation propulsors, more accurate elements could be used, such as:

- a) Autocollimators for the measurement system, in order to increase the sensibility from 25 nN to 10 nN, providing also a better communication between measurement and damping system and a much more reliable system, as shown in chapter 4.1.1;
- b) Optical fiber light collimation for the damping system, in order to make more use of the power emitted by the LEDs with more efficient collimating system, chapter 4.1.2;
- c) More powerful LEDs for the damping system, in order to increase the maximal thrust limit of 500 nN up to 1  $\mu$ N, as required by Lisa-Pathfinder.

## References

- [1] S. Fasoulas, G. Herdrich, T. Schateikis and J. Martin, “High Precision Attitude Control System Based on the Emission of Electromagnetic Radiation”, *35th International Electric Propulsion Conference, IEPC-2017-273*, Atlanta, USA, 2017.
- [2] D. Nicolini, “LISA Pathfinder Field emission thruster system development program,” *30th International Electrical Propulsion Conference, IEPC-2007-363*, Florence, Italy, 2007.
- [3] A. Jamison, “Accurate Measurement of Nano-Newton Thrust for Micropropulsion System Characterization”, *27th International Electric Propulsion Conference, IEPC-01-236*, Pasadena, CA, 2001.
- [4] J. Ziemer, “Performance measurements using a sub-micronewton resolution thrust stand”, *27th International Electric Propulsion Conference, IEPC-01-238*, Pasadena, CA, 2001.
- [5] J. P. Lake, G. Cavallaro, G. Spanjers, P. B. Adkison and M. J. Dulligan, “Resonant Operation of a Micro-Newton Thrust Stand”, *28th International Electric Propulsion Conference, IEPC-0303-0298*, Toulouse, France, 2003.
- [6] C. Phipps and J. Luke, “Diode Laser-Driven Microthrusters: A New Departure for Micropropulsion”, *AIAA Journal, Vol. 40, No. 2*, 2002.
- [7] C. R. Phipps, J. R. Luke, W. Helgeson and R. Johnson, “A Low-Noise Thrust Stand for Microthrusters with 25nN Resolution”, 2006.
- [8] M. Gamero-Castaño, “A torsional balance for the characterization of microNewton thrusters”, *Review of Scientific Instruments 74(10)*, 4509–4514, 2003.
- [9] Y.-X. Yang, L.-C. Tu, S.-Q. Yang and J. Luo, “A torsion balance for impulse and thrust measurements of micro-Newton”, *The Review of scientific instruments, Vol. 83, 015105*, 2012.
- [10] J. Soni and S. Roy, “Design and characterization of a nano-Newton resolution thrust stand”, *Review of Scientific Instruments, Vol. 84*, 2013.
- [11] C. Ronda, “Luminescence”, *WILEY-VCH Verlag GmbH & Co. KGaA*, 2008.
- [12] P. Ball, “Leds get on the right wavelength”, *Nature News. 10.1038/news030505-2*, 2003.
- [13] M. Cullen and J. Mearns, “Coulometric determination of arsenic gallium arsenide”, *Analytica Chimica Acta, vol. 277, no. 1, pp. 113-117*, 1993.
- [14] P. Hart, “Green and yellow emitting devices vapor-grown gallium phosphide”, *Proceedings of the IEEE, vol. 61, no. 7, pp. 880-884*, 1973.
- [15] S. Chang, Y. C. T. Lin, B. Huang, S. Chang, C. Chang, Y. Lin and C. Wong, “Znse based white light emitting diode on homoepitaxial znse substrate”, *Optoelectronics, IET, vol. 1, no. 1, pp. 39-41*, 2007.
- [16] S. Nakamura, T. Mukai and M. Senoh, “High-brightness ingan/algan doubleheterostructure blue-green-light-emitting diodes”, *Journal of Applied Physics, Vol. 76, no. 12, pp. 8189-8191*, 1994.
- [17] “How to Choose the Right LED Lighting Product Color Temperature”, UR-EKA Lighting & Controls, 2010. [Online]. Available: <https://ur-eka.com/how-to-choose-the-right-led-lighting-product-color-temperature/>.
- [18] “Spectral response different kinds of light sources”, Housecraft.ca, 2012. [Online]. Available: <http://housecraft.ca/eco-friendly-lighting-colour-rendering-index-and-colour-temperature/>.
- [19] L. Donaldson, “Improved white leds”, *Materials Today, Vol. 16, no. 3, pp. 51-52*, 2013.
- [20] E. Schubert, “Light-Emitting Diodes”, *Cambridge University Press*, 2006.
- [21] M.-H. Kim, M. F. Schubert, Q. Dai, J. K. Kim, E. F. Schubert, J. Piprek and Y. Park, *Applied Physics Letters, 91(18):183507*, 2007.

- [22] A. Thorseth, “Characterization, Modeling, and Optimization of Light-Emitting Diode Systems”, Faculty of Science, University of Copenhagen, 2011.
- [23] Lumileds, “Luxeon rebel direct color portfolio”, Philips Lumileds Lighting Company, 2016. [Online]. Available: <https://www.lumileds.com/uploads/28/DS68-pdf>.
- [24] Cree, “Cree XLamp XR-E LED”, Data Sheet, 2009. [Online]. Available: <https://www.prosoft.ru/cms/f/352041/XLamp7090XR-Epdf.pdf>.
- [25] X. QU, “Development and Design of Light-emitting-diode (LED) Lighting Power Supplies”, Department of Electronic and Information Engineering, The Hong Kong Polytechnic University, 2009.
- [26] McGraw-Hill, Encyclopedia of Science & Technology, 10th Edition, McGraw-Hill, 2012.
- [27] L. S. Pedrotti, “Fundamentals of Photonics”, *Module on Basic Geometrical Optics*, 2008.
- [28] Thorlabs.com, “Lens Tutorial”, Spherical Singlets, 2015. [Online]. Available: [https://www.thorlabs.com/newgrouppage9.cfm?objectgroup\\_id=8790](https://www.thorlabs.com/newgrouppage9.cfm?objectgroup_id=8790).
- [29] W. J. Smith, Modern Optical Engineering, 4th Edition, McGraw-Hill Education, 2007.
- [30] Thorlabs.com, “Aspheric Condenser Lenses”, Thorlabs, 2015. [Online]. Available: [https://www.thorlabs.com/newgrouppage9.cfm?objectgroup\\_id=3835](https://www.thorlabs.com/newgrouppage9.cfm?objectgroup_id=3835).
- [31] Thorlabs.com, “Fresnel Lenses”, Thorlabs, 2013. [Online]. Available: [https://www.thorlabs.com/newgrouppage9.cfm?objectgroup\\_id=1222](https://www.thorlabs.com/newgrouppage9.cfm?objectgroup_id=1222).
- [32] G. Sereni, “The study of Newton's rings for alignment of”, Dipartimento di Fisica ed Astronomia, Univerisità degli Studi di Parma, 2015.
- [33] Japan Aerospace Exploration Agency, “Small Solar Power Sail Demonstrator 'IKAROS' Successful Attitude Control by Liquid Crystal Device”, *JAXA Press Release 9th August 2015*, 2015.
- [34] Eoport.al.or, “LightSail-2”, Earth Observation Portal, 2019. [Online]. Available: <https://directory.eoport.al.org/web/eoport.al/satellite-missions/l/lightsail-2#footback5%29>.
- [35] J. E. Polk, A. Pancotti, T. Haag, S. King and M. Walker, “Recommended Practices Thrust Measurements”, *33th International Electric Propulsion Conference, IEPC-2013-440*, Washington, DC, 2013.
- [36] J. C. Anderson, The Seismic Design Handbook, Dynamic Response of Structures, pp 183-246, Dynamic Response of Structures: Farzad Naeim, 2001.
- [37] Dial.de, “Efficiency of LEDs: The highest luminous efficacy of a white LED.”, DIAL, 2016. [Online]. Available: <https://www.dial.de/en/blog/article/efficiency-of-ledsthe-highest-luminous-eficacy-of-a-white-led/>.
- [38] Haag-streit.com, “ELCOMAT Product Line, ELCOMAT Vario”, MÖLLER-WEDEL OPTICAL, [Online]. Available: <https://www.haag-streit.com/moeller-wedel-optical/products/electronic-autocollimators/elcomat-product-line/elcomat-vario/>.
- [39] Haag-streit.com, “ELCOMAT direct”, MÖLLER-WEDEL OPTICAL, [Online]. Available: [https://www.haag-streit.com/fileadmin/Moeller\\_wedel\\_optical/Brochures/Electronic\\_Autocollimators/ELCOMAT\\_direct\\_English.pdf](https://www.haag-streit.com/fileadmin/Moeller_wedel_optical/Brochures/Electronic_Autocollimators/ELCOMAT_direct_English.pdf).
- [40] Trioptics.com, “TriAngle product finder”, TRIOPTICS, 2014. [Online]. Available: <https://www.trioptics.com/products/electronic-autocollimators/>.
- [41] Goldstonescientific.com, “Prizmatix UHP-T2-LED-White: 2 Inch, High CRI Microscope LED Light Source”, GoldstoneScientific, [Online]. Available: <https://www.goldstonescientific.com/prizmatix-uhp-t2-led-white-2-inch-high-cri-microscope-led-light-source/>.

- [42] Goldstonescientific.com, “Prizmatix UHP-T-D Violet LED System at 405nm”, GoldstoneScientific, [Online]. Available: <https://www.goldstonescientific.com/prizmatix-uhp-t-d-violet-led-system-at-405nm/>.
- [43] J. H. Lau, Chip On Board: Technology for Multichip Modules, Springer Science & Business Media, 1994.
- [44] Reuk.co.uk, “LED Dimmer Circuit”, REUK.co.uk, 2007. [Online]. Available: <http://www.reuk.co.uk/wordpress/lighting/led-dimmer-circuit/>.
- [45] Ac-rc.net, “AC85-265V 100W Waterproof PWM Dimmable Driver [UV363-100-PWM]”, AC-RC Hobby, 2014. [Online]. Available: [http://ac-rc.net/catalog/product\\_info.php?products\\_id=241](http://ac-rc.net/catalog/product_info.php?products_id=241).
- [46] Ebay.it, “Royal Blue 440-450nm High Power LED SMD Chip Lamp”, CH\_Town Electronic, 2019. [Online]. Available: <https://www.ebay.it/itm/1w-3w-5w-10w-20w-30w-50w-100w-Royal-Blue-440-450nm-High-Power-LED-SMD-Chip-Lamp/122022099000?hash=item1c69157838:m:msnvFtOR9BGRxLqK0OE8REg>.
- [47] Eu.mouser.com, “ASMT-JL31-NRS01”, Broadcom / Avago, [Online]. Available: <https://eu.mouser.com/ProductDetail/Broadcom-Avago/ASMT-JL31-NRS01?qs=9j6qqDjiC69xEsOkICvcNg==>.
- [48] A. Technologies, “ASMT-Jx3x 3W Mini Power LED Light Source, Datasheet”, AVAGO Technologies, 2014. [Online]. Available: <https://docs.broadcom.com/docs/AV02-1941EN>.
- [49] LED\_ENGIN, “LuxiGen™ Violet LED Emitter Series LZ1 395nm Power, LZ1-00UAP5, Datasheet”, 2018. [Online]. Available: <http://www.ledengin.com/files/products/LZ1/LZ1-00UAP5.pdf>.
- [50] Eu.mouser.com, “LZ1-00UAP5-00U5”, LED Engin, 2018. [Online]. Available: <https://eu.mouser.com/ProductDetail/LED-Engin/LZ1-00UAP5-00U5?qs=%2Fha2pyFadugnkoJHT2QoxvjvsO3d5xhyZmU6r6XwclOnSasFV6529w%3D%3D>.
- [51] Amazon.de, “Tesfish 100W LED Chip White Bulb High Power Energy Saving Lamp Chip (100W white)”, Tesfish, 2016. [Online]. Available: [https://www.amazon.de/Tesfish-White-Power-Energy-Saving/dp/B01DFDKH2E/ref=sr\\_1\\_27?\\_\\_mk\\_de\\_DE=%C3%85M%C3%85%C5%BD%C3%95%C3%91&keywords=led+100w&qid=1565953921&s=gateway&sr=8-27](https://www.amazon.de/Tesfish-White-Power-Energy-Saving/dp/B01DFDKH2E/ref=sr_1_27?__mk_de_DE=%C3%85M%C3%85%C5%BD%C3%95%C3%91&keywords=led+100w&qid=1565953921&s=gateway&sr=8-27).
- [52] Amazon.de, “Tesfish 44mm Linse 60 grad+ 50mm Reflektor Tasse + feste Halterung für 20W 50W 100W Led Licht chip”, Tesfish, 2016. [Online]. Available: [https://www.amazon.de/Tesfish-Linse-Reflektor-Tasse-Halterung/dp/B01CU101F0/ref=pd\\_sbs\\_201\\_7?encoding=UTF8&pd\\_rd\\_i=B01CU101F0&pd\\_rd\\_r=1c22a792-836b-43af-8a29-d2e5109c4b8b&pd\\_rd\\_w=rQlzg&pd\\_rd\\_wg=LjVRR&pf\\_rd\\_p=74d946ea-18de-4443-bed6-d8837f922070&pf\\_rd\\_r=7](https://www.amazon.de/Tesfish-Linse-Reflektor-Tasse-Halterung/dp/B01CU101F0/ref=pd_sbs_201_7?encoding=UTF8&pd_rd_i=B01CU101F0&pd_rd_r=1c22a792-836b-43af-8a29-d2e5109c4b8b&pd_rd_w=rQlzg&pd_rd_wg=LjVRR&pf_rd_p=74d946ea-18de-4443-bed6-d8837f922070&pf_rd_r=7).
- [53] Amazon.com, “Parabolic Reflector Lens for 100W LED Chip”, STRATUS LEADS, 2017. [Online]. Available: <https://www.amazon.com/Parabolic-Reflector-Lens-100W-Chip/dp/B073TY6BFR?SubscriptionId=AKIAIOCEBIGP6NUBL47A&tag=&linkCode=xm2&camp=2025&creative=165953&creativeASIN=B073TY6BFR>.
- [54] Thorlabs.com, “ACL5040U - Aspheric Condenser Lens, Ø50 mm, f=40 mm, NA=0.60, Uncoated”, THORLABS, 2015. [Online]. Available: <https://www.thorlabs.com/thorproduct.cfm?partnumber=ACL5040U>.
- [55] Alibaba.com, “Round Optical PMMA Plastic Car Parking Wide Angle Fresnel Lens Large Diameter 110 mm Focal Length -350mm Minifier Lens”, DOUMOO, [Online]. Available: [https://www.alibaba.com/product-detail/Round-Optical-PMMA-Plastic-Car-Parking\\_60692071624.html?spm=a2700.7724857.normalList.69.342076d9ypQanW](https://www.alibaba.com/product-detail/Round-Optical-PMMA-Plastic-Car-Parking_60692071624.html?spm=a2700.7724857.normalList.69.342076d9ypQanW).
- [56] INTERNATIONAL STANDARDS, “ISO 11664-1 (CIE S 014-1/E): COLORIMETRY -- PART 1: CIE STANDARD COLORIMETRIC OBSERVERS”, 2007. [Online]. Available: <https://www.sis.se/api/document/preview/910475/>.

- [57] YUJI\_LED, “YJ-BC-160H-G01 High CRI LED, Datasheet”, 2016. [Online]. Available: <https://cdn.shopify.com/s/files/1/0344/6401/files/YJ-BC-160H-G01.pdf>.
- [58] J. L. Wright, *Space Sailing*, Routledge, 1992.
- [59] Hella.com, “LED HEADLIGHTS”, HELLA TECH WORLD, 2014. [Online]. Available: <https://www.hella.com/techworld/au/Technical/Automotive-lighting/LED-headlights-833/>.
- [60] Cobledarray.com, “6500K - 8500K LED Light Emitter 65° Viewing Angle 20 W White LEDs”, TYANSHINE, 2014. [Online]. Available: <http://www.cobledarray.com/sale-4009402-6500k-8500k-led-light-emitter-65-viewing-angle-20-w-white-leds.html>.
- [61] Sunfounder.cc, “Specification of SunFounder 55g Servo, Datasheet”, 2017. [Online]. Available: [http://wiki.sunfounder.cc/images/7/78/SunFounder\\_55g\\_Servo\\_datasheet.pdf](http://wiki.sunfounder.cc/images/7/78/SunFounder_55g_Servo_datasheet.pdf).
- [62] Ekwb.com, “Custom CPU Loop, Components of the liquid cooling loop”, 2016. [Online]. Available: <https://www.ekwb.com/solutions/custom-loop/#needed-components>.
- [63] Amazon.co.uk, “Asiproper CPU Water Block Water Cooler Computer Cooling Radiator for Intel AMD+Screws”, Asiproper, 2018. [Online]. Available: <https://www.amazon.co.uk/Asiproper-Cooler-Computer-Cooling-Radiator-Black-Transparent/dp/B07CXV5JHJ>.
- [64] Koolance.com, “Radiator, 1x120mm 18-FPI Aluminum”, KOOLANCE, 2013. [Online]. Available: <https://koolance.com/radiator-1-fan-120mm-18-fpi-aluminum>.
- [65] Kjmagnetics.com, “D88-N52”, K&J Magnetics, Inc., [Online]. Available: <https://www.kjmagnetics.com/proddetail.asp?prod=D88-N52>.
- [66] J. Soni, J. C. Zito and S. Roy, “Design of a microNewton Thrust Stand for Low Pressure Characterization of DBD Actuators”, *51st Aerospace Sciences Meeting*, Grapevine, TX, 2013.
- [67] Thorlabs.com, “LA1252 - N-BK7 Plano-Convex Lens, Ø25.0 mm, f = 25.4 mm, Uncoated”, THORLABS, 2009. [Online]. Available: <https://www.thorlabs.com/thorproduct.cfm?partnumber=LA1252>.
- [68] Thorlabs.com, “LC1054-A-ML - Ø1/2" N-BK7 Plano-Concave Lens, SM05-Threaded Mount, f = - 25.0 mm, ARC: 350-700 nm”, THORLABS, 2015. [Online]. Available: <https://www.thorlabs.com/thorproduct.cfm?partnumber=LC1054-A-ML>.
- [69] Thorlabs.com, “LA1464-ML - Ø1" N-BK7 Plano-Convex Lens, SM1-Threaded Mount, f = 1000.0 mm, Uncoated”, THORLABS, 2015. [Online]. Available: <https://www.thorlabs.com/thorproduct.cfm?partnumber=LA1464-ML>.
- [70] D. Hill, “How to convert FWHM measurements to  $1/e^2$  halfwidths”, Zemax CUSTOMER PORTAL, 2007. [Online]. Available: <https://customers.zemax.com/os/resources/learn/knowledgebase/how-to-convert-fwhm-measurements-to-1-e-squared-ha>.
- [71] Pi.gate.ac.uk, “CdS PHOTOCONDUCTIVE CELLS GL5528, Datasheet”, 2014. [Online]. Available: <https://pi.gate.ac.uk/pages/airpi-files/PD0001.pdf>.
- [72] Cdn.sparkfun.com, “74HC4051; 74HCT4051: 8-channel analog multiplexer/demultiplexer”, 2016. [Online]. Available: [https://cdn.sparkfun.com/assets/learn\\_tutorials/5/5/3/74HC\\_HCT4051.pdf](https://cdn.sparkfun.com/assets/learn_tutorials/5/5/3/74HC_HCT4051.pdf).
- [73] Egismos.com, “520nm, Green Diode Laser Model, Datasheet”, 2019. [Online]. Available: <http://www.egismos.com/laser-modules/green-laser-module-D45205D.pdf>.
- [74] Bourns.com, “3296 - 3/8 ” Square Trimpot® Trimming Potentiometer, Datasheet”, 2016. [Online]. Available: <https://www.bourns.com/docs/Product-Datasheets/3296.pdf>.
- [75] Bourns.com, “3590 - Precision Potentiometer, Datasheet”, 2017. [Online]. Available: <https://www.bourns.com/pdfs/3590.pdf>.